ELECTRIC SENSING ZONE SIGNAL BEHAVIOUR IN LIQUID ALUMINIUM

by

François Dallaire

Department of Mining and Metallurgical Engineering
McGill University
Montréal, Canada
February, 1990

A Thesis Submitted to the
Faculty of Graduate Studies and Research
in Partial Fulfillment of the Requirements for the Degree of
Master of Engineering

ABSTRACT

Metal cleanliness is a major concern of today's aluminium industry. The metal cleanliness is related to the number and size of nonmetallic inclusions suspended in the liquid metal. A sensor, submerged in a liquid metal bath, produces a characteristic electrical signal during the passage of a particle through its Electric Sensing Zone (ESZ). On-line analysis of these signals enable melt particle size distribution to be derived. The present study focuses on signals obtained during application of such a sensor to aluminium melts.

Both the sensor and the preprocessing stages of the signal are described. A mathematical model of the high pass filtering transfer function is developed in the time domain to predict its role in modifying the raw signal's transient waveforms

Classes of signal transients are identified and described in anticipation of further development based on pattern recognition techniques. Signal behaviour description in specific situations are performed through the relative occurrence rates of each class of transient. Attention is directed towards extraction of information relative to, both the production of particle size distribution as well as for sensor control purposes.

RESUME

De nos jours, l'industrie de l'aluminium porte beaucoup d'interêt a la purete du métal. Cette purete est reliee au nombre et a la dimension des particules non metalliques en suspension dans le metal liquide. Un senseur, submerge dans un bain de metal, produit un signal électrique caracteristique lors du passage d'une particule a travers sa Zone Electrique Sensible. L'analyse de ces signaux permet de deriver, in situ, la distribution de tailles des particules en suspension dans le bain de metal. La presente etude porte sur l'analyse de signaux produits lors de l'utilisation de ce senseur dans des bains d'aluminium.

La generation et le traitement des signaux sont decrits. La fonction de transfert du filtre passe haut est predite par des modeles mathematiques afin de caracteriser son role quant a la modification des signaux originaux

Des classes de transients sont identifiees et decrites pour preparer a l'introduction de techniques de reconnaissance de forme. La frequence relative d'observation des transients de chacune des classes est utilisee pour caractériser le comportement du signal dans divers contextes spécifiques. L'extraction de l'information contenue dans le signal est faite en relation avec la production et la validation de la distribution de tailles des particules ainsi qu'avec les aspects de contrôle du senseur.

ACKNOWLEDGMENTS

I would like to thank Professor Rod Guthrie for sponsoring this project, as well as for the faith he showed, from the start, in this new avenue of research within his group.

My special thanks are due to Jean-Pierre Martin, a research fellow at Alcan's Laboratories in Arvida for making possible laboratory and in-plant recordings of LiMCA signals and for his constant interest and useful discussions.

I would also like to thank our technician, Frank Sebo, for his constant imaginative technical support, Selçuk Kuyucak, a fellow student, for providing the orifice picture in Figure 1.2. and finally, Gregory Carayannis, for his valuable comments relative to the thesis document.

The research project was primarily funded by grants from NSERC and Alcan International Ltd

TABLE OF CONTENT

LIST OF FIGURES

LIST OF TABLES

Table Title Page #

CHAPTER 1 -- INTRODUCTION

The problem of metal cleanliness is a major concern in the aluminium industry. Many applications, and consequently volume of sales increase, are possible only with improved metal cleanliness. The cleanliness depends on the number, the size and distribution of nonmetallic inclusions suspended in a melt. In aluminium alloys, inclusions with diameter greater than 15μm can be considered potentially detrimental. Depending on the application, their presence can yield to different types of defects which increase breakage and/or rejection rates in the production lines. For example, the production of beverage can body is very sensible to the presence of inclusions in thin metal sheets since they cause the metal to tear or the can to collapse when its content is pressurized.

A number of techniques are available to improve the metal cleanliness. These include fluxing of the melt with active, passive or a mixture of gases, decantation of the melt, filtration through different types of beds and finally, combination of gas flux with mechanical agitation. A SNIF degasser unit is such kind of technique and was encountered in the frame of this work. Standing for "Spinning Nozzle In-line Flotation", it is a commercial product of Union Carbide. A SNIF degasser consist of a gas bubbling injection system equipped with a spinning paddle improving the rate of gas mixing with molten aluminium flowing through the unit. Injection of an inert gas with a small proportion of chlorine is performed on certain types of aluminium alloys to remove inclusions, hydrogen and alkalis. In general, the purpose of these melt cleaning techniques is to reduce its concentration of both hydrogen and suspended inclusions.

Before the introduction of the Electric Sensing Zone (ESZ) technique, no rapid quantitative analytical method was available for the monitoring of suspended inclusion in melts. Gross chemical analysis giving bulk concentration of an element, is not providing information about inclusion size. An other method, the Porous Disk Filtration Apparatus (PoDFA), developed and used by Alcan International LTD, is based on direct examination of polished surfaces. Since the concentration of inclusion in liquid aluminium is usually low for such examination, preconcentration of inclusion is required. Basically, the method consist of forcing five pounds of sampled melt to flow through a porous disk. The porous disk and its content (metal and trapped inclusions) are allowed to cool and are recuperated for optical metallographic analysis. While this method procures indication of inclusion size and composition, it is semi-quantitative since it may be affected by the judgment of the metallographer. On top of that, the performance of the method is sensible to the permeability of the porous disk and the metallographic analysis is time consuming.

An ultrasonic technique, similar to the one used for nondestructive testing of solid materials, has been shown to be applicable to molten metals [1]. Such a technique has been developed by Renolds Aluminium Company [2]. While the promises of the technique are to give the size, the shape and the concentration of suspended inclusions, the method is confronted to a lower detection limit for inclusion size. The method could measure the bulk concentration of inclusion greater than 47μm while only inclusions greater than 235μm could be detected individually [3]. Smaller particle can be detected only with an increased ultrasonic inspection frequency. In practice, the transmission of a higher frequency requires a wave guide and is subject to strong attenuation. More development is required before this technique becomes attractive.

1.0 Melt inclusion monitoring with an electric sensing zone technique

The Electric Sensing Zone technique, also known as the resistive pulse technique, was first developed by Coulter in the 1950's for blood cells counting and size analysis [4]. Since then, it has been widely applied to the detection of several other types of suspensions in aqueous solutions and has been enhanced to increase sensor's particle detection limits down to submicron levels [5].

The application of the technique to liquid metals began with the research of D. Doutre at McGill [3]. The primary motivation for this work was the lack of any rapid method for the monitoring of inclusion content of a melt, suitable for process control. The extension of the ESZ technique to the high temperature corrosive environment and low electrical resistivity of liquid metals was not an easy task. Selecting proper materials for the probe assembly was important, but the key step to make the technique reliable was the discovery that a very high electric current passed through the orifice could clean it and wet it, allowing restabilization of the signal. This is known as the "conditioning current". The apparatus implementing the technique has been named LiMCA, the acronym standing for "Liquid Metal Cleanliness Analyzer".

The LiMCA apparatus offers unique on-line features, providing both the number and size distribution of inclusions suspended in a volume of melt sampled directly from the launder. This make it a very attractive industrial casting quality control method, as well as a powerful process metallurgy R&D tool.

The LiMCA apparatus was fine tuned for the analysis of aluminium purity when Alcan became involved in its development. A number of prototypes have now been tested. Industrial models have been designed, debugged, installed and were in full time operation in eight Alcan casting plants around the world as of August 1988.

The application of the technique to other melts (copper, magnesium, cast iron and steels) is under continued investigation at McGill. While it has been shown that the technique can be applied in these melts, sensor head equipment is still at the prototype stage of development. For these reasons, in the present study, the analysis of the behaviour of the ESZ of the LiMCA system will be limited to the context of aluminium melts.

1.1 LiMCA principle of operation

The principle of operation of the LiMCA apparatus is illustrated by Figure 1.1. The detection and measurement of suspended particles in a conducting fluid is performed by the ESZ technique while the liquid to be analyzed is drawn at a constant rate through an orifice into an electrically insulated vessel, the probe. Simultaneous to the liquid's inhalation into the probe, a constant electric current I, flowing from one electrode to the other is also maintained across the orifice by a battery of potential V_B. The passage of a non metallic particle through the orifice temporarily increases the electrical resistance of the ESZ. This variation in resistance, in the presence of electric current I, registers as a voltage transient superimposed on the steady state potential V_E taken across the electrodes, as shown in Figure 1.1. To a first approximation, the amplitude of the superimposed voltage pulse is proportional to the volume of the particle, so that counting pulses and measuring their amplitude allows one to evaluate the concentration and size distribution of particles within the sampled fluid.

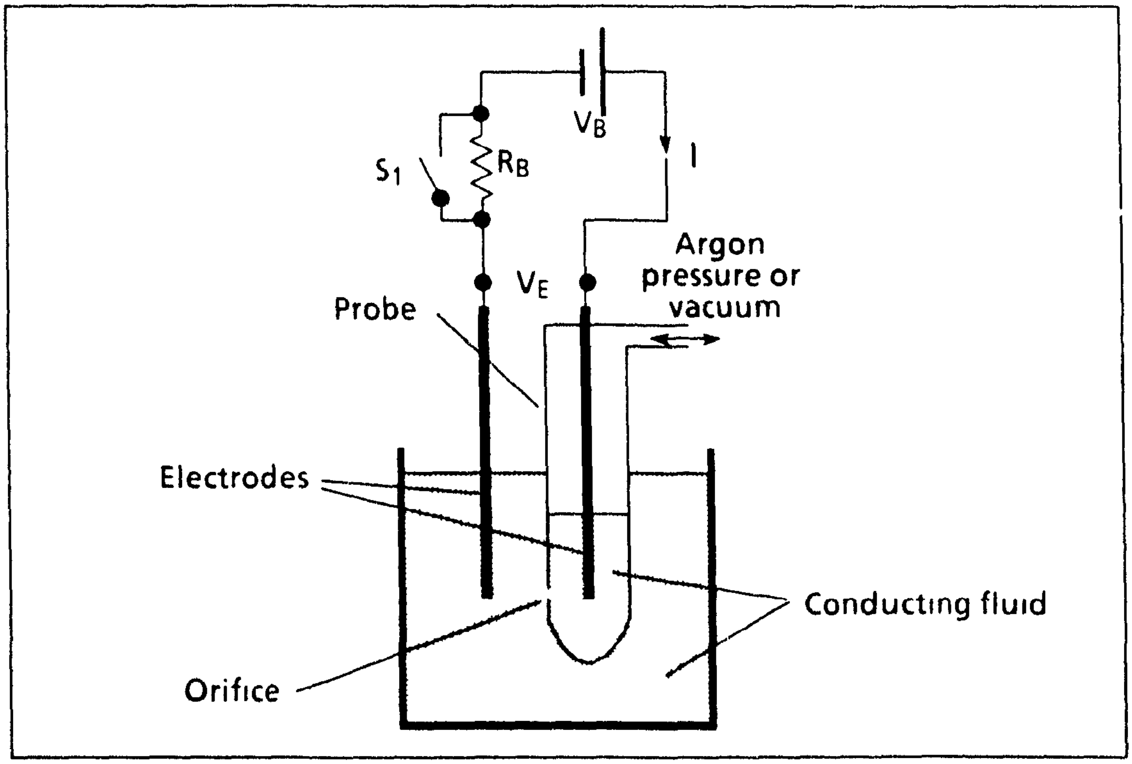

Figure 1.1 LiMCA principle of operation

The analysis procedure is initiated when the probe is first submerged in the melt, and metal is aspirated into the probe establishing the first contact between the two electrodes. The melt sampling cycle then begins with the aspiration of the melt into the probe until the level of melt inside the probe reaches the outside melt level. In order to avoid metal freeze up, an argon gauge pressure is applied above the melt so that the melt is flushed out of the probe. A cycle is typically performed over a time interval in the order of one minute. The filling and the emptying parts of the cycle are typically of equal duration.

The analysis of the signal typically takes place during the filling up part of the cycle. This is called the "up-mode analysis". Usually, while the tube is being emptied, no signal analysis is done and even the electric current, I, through the orifice, is turned off to extend the battery life. However, in particular cases discussed in Section 5.4.1, such analysis is performed and this will be referred to as "down-mode analysis".

The particle concentrations and size distributions are typically evaluated at each melt sampling cycle. The accumulated counts, divided by the volume of melt sampled, yields to the inclusion concentration. The volume sampled is estimated by measuring the time interval over which the pulse detection analysis takes place and assuming a fixed constant melt flow rate through the orifice [3].

The conditioning current is generated physically, by closing (for a few seconds) the switch S_1 (Figure 1.1). This action short cuts the resistor R_B. The current is then only limited by the resistance between the electrodes. As this is much smaller than R_B, a much higher current (200 to 300 A) is induced through the sensing zone. It is believed that the beneficial effect of the conditioning current is due to intense localized heat being generated, causing good wetting of the orifice wall and removing any accumulated debris (i.e. inclusions) [3]. The conditioning current is generally applied at the beginning of each cycle in order to improve signal stability following melt flow inversion.

1.2 The orifice

Obtaining an adequate and reliable signal depends greatly on the pattern of melt flow through the orifice. The flow must be laminar for the baseline to be stable. A smoothly shaped orifice together with good wetting of the orifice wall by the melt are key parameters determining desirable laminar flows. Fortunately, the glass blowing technique used to create the orifice in the side wall of the Kimax tubes produces a very smoothly shaped symmetrical orifice.

A cross section of such an orifice is shown in Figure 1.2. Proper wetting of the orifice wall by the melt is readily achieved in the case of aluminium by applying the conditioning current.

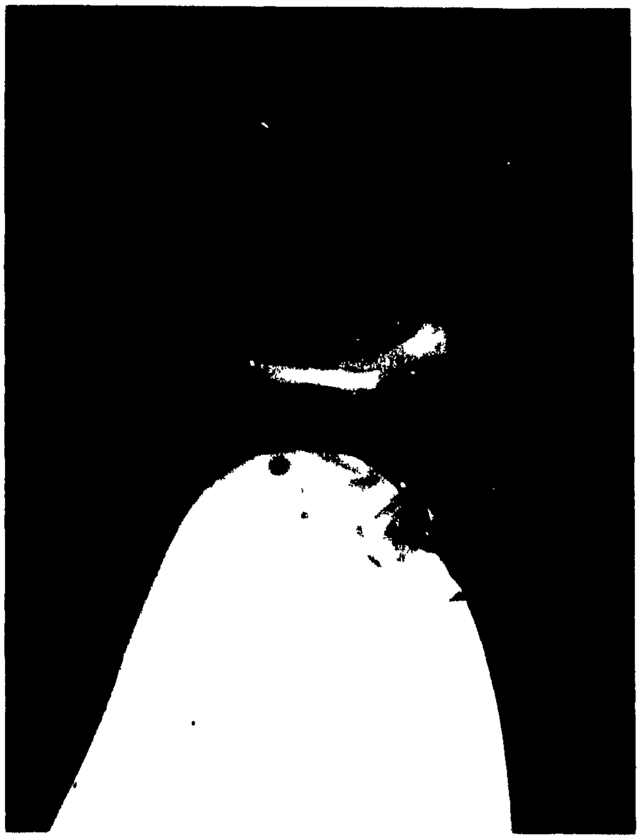

Figure 1.2 Picture of a Kimax transverse section orifice shape.

The rate of metal flow into the probe is also an important parameter. At low flow rates, orifice blockages are frequent while at high rates, turbulent flow may occur. Optimal operating conditions have been determined [3] where a positive or negative Argon pressure of 16.92kPa (2.5 psi) maintained inside the probe produces a 16 ml/min volumetric flow rate (3.77 m/s average fluid velocity) through a 300 μm diameter orifice. However, a flow rate of 0.5 ml/sec was used for all experiments studied in later chapters.

1.3 Prediction of resistive pulse magnitude

The resistive pulse magnitude is function of d, the diameter of the inclusion passing through the orifice, D, the orifice diameter and L,the orifice length. The orifice length is generally taken as the thickness of the probe wall. The problem of predicting the magnitude of the resistive pulse for all values of (d/D) has no simple analytical solution. It has been demonstrated [6] for $(d/D) < 0.4$, that for a cylindrical orifice of length L, much greater than its diameter D, the passage of an insulating particle of diameter d, suspended in a conducting fluid of electrical resistivity ρ, generates a resistive pulse of magnitude ΔR given by :

$$\Delta R = \frac{4\rho d^3}{\pi D^4} \qquad \text{Eq 1.1}$$

This relation indicates the dependence of ΔR, the resistance increase, on the particle volume Vp, and its independence with respect to the orifice length. It can also be rewritten as :

$$\Delta R = K\, Vp \qquad \text{Eq 1 2}$$

where K is a function of the fluid's resistivity and the orifice diameter :

$$K = \frac{24\rho}{\pi^2 D^4} \qquad \text{Eq 1.3}$$

The value of K can be computed theoretically, for a given ρ and D. In practice, since the effects of a smoothly shaped elliptical orifice of short length compared to its diameter on ΔR is neglected, a calibration procedure in aqueous solution using standard spheres is recommended.

For the range $0 < (d/D) < 0.8$, correction factors for ΔR have been published [7] which yield to an accuracy of 99%. The correction function may be expressed analytically as [6] :

$$f\left(d/D\right) = \frac{1}{1 - 0.8\left(\frac{d}{D}\right)^3} \qquad \text{Eq. 1.4}$$

For the case of (d/D) closer to unity a more sophisticated development is needed. This is however of little practical interest since very large particles would cause frequent orifice blockage.

The determination of the voltage transient corresponding to the resistance variation of Eq. 1.4 is performed by applying Ohm's law on the current feeding circuit of Figure 1.1. With the currents I_1 and I_0 respectively with, and without a particle in the orifice, then :

$$\Delta V = I_1\left(R_E + \Delta R\right) - I_0 R_E \qquad \text{Eq 1.5}$$

with

$$I_1 = \frac{V_B}{R_B + R_E + \Delta R} \qquad \text{Eq 1.6a)}$$

and

$$I_0 = \frac{V_B}{R_B + R_E} \qquad \text{Eq 1.6b)}$$

the voltage variation may be rewritten

$$\Delta V = I_0 \frac{R_B}{R_B + R_E + \Delta R} \Delta R \qquad \text{Eq 1.7}$$

where ΔR can be neglected in the denominator. The final expression for the variation in voltage as a function of a particle diameter is thus :

$$\Delta V = I_0 \frac{R_B}{R_B + R_E} \frac{1}{\left\{1 - 0.8\left(d/D\right)^3\right\}} \frac{4\rho d^3}{\pi D^4} \qquad \text{Eq 1.8}$$

Measured values of R_E and R_B are used to calculate the ratio $R_B/(R_E + R_B)$.

CHAPTER 2 -- THEORETICAL SIGNAL

2.1 Introduction

The theoretical signal is defined as an ideal signal to be expected from the perfect behaviour of an ESZ device in the absence of any "noise" or electrical interference picked up from the surrounding world. Even if such signals are not commonly found in real life, it is important to understand their characteristics. They also can illustrate the purposes and effects of the signal conditioning stages.

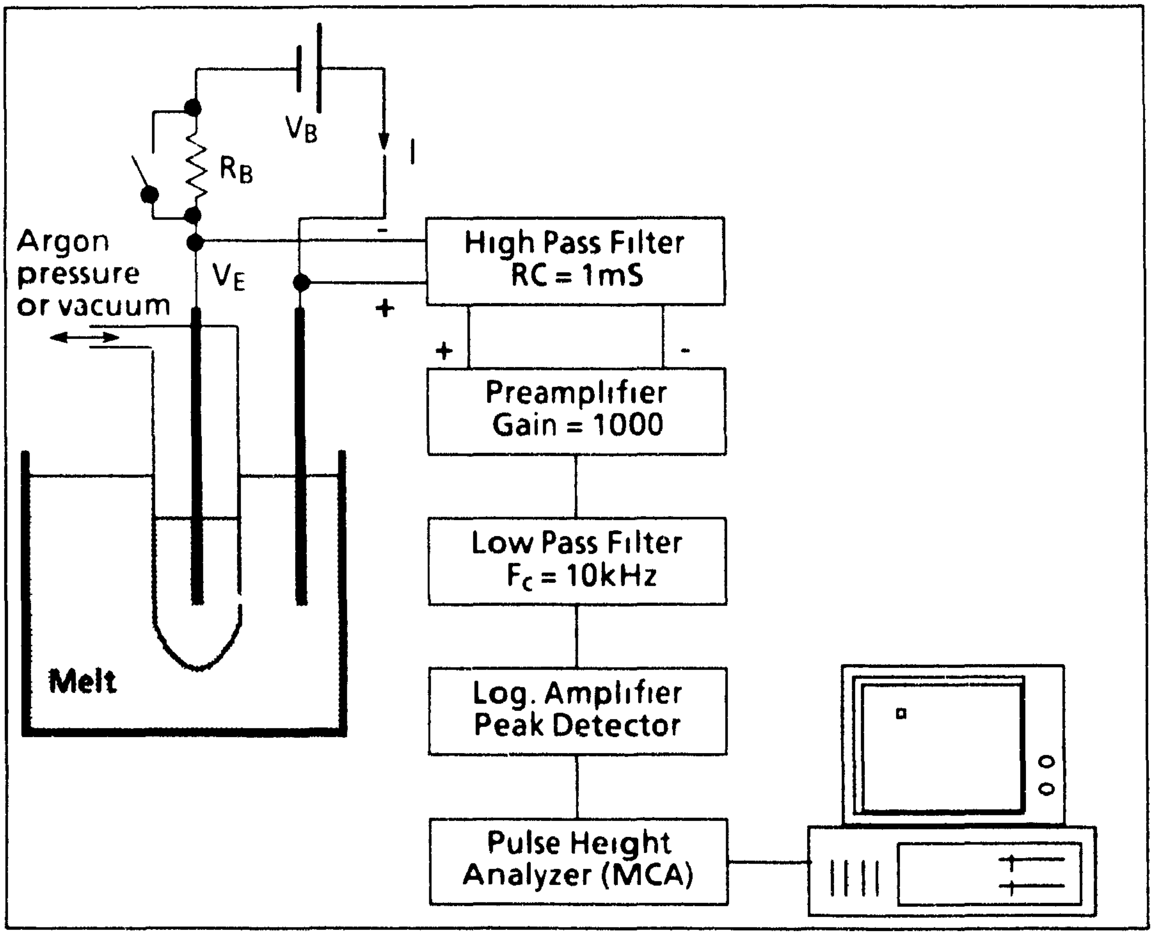

Figure 2.1 ESZ device schematic diagram

Figure 2.1 illustrates, in the schematic form, the ESZ probe, the current feeding circuit and the signal analysis system. The current feeding circuit consists of a battery providing a constant potential, V_B (6V), and a ballast resistance R_B (0.2ohm). Together, they constitute a DC current source (60 A) connected to both electrodes. The current loop is closed when the melt establishes contact between the electrodes after it has been sucked into the submerged probe. The probe for aluminium melts, is fabricated from an electrically insulating material (Kimax). The passage of electrical current through the probe's orifice constitutes the Electric Sensing Zone (ESZ).

The five rectangular boxes in Figure 2.1 schematize the preprocessing stages of the actual signal analysis system. The first stage, a passive high pass filter with 1ms time constant removes the DC component of the signal. This stage introduces a few side effects in the transients (e.g. amplitude loss and undershoot). The filtered signal is than fed to the differential preamplifier having a gain of 1000. The third stage is a low pass filter which limits the bandwidth of the signal to 10kHz. The next box incorporates two analog electronic devices. The first one is a logarithmic amplifier that proportionally applies a higher gain to lower amplitude signals. Its purpose is to improve the detection of small pulses. The second function is a peak detector which responds only to signals whose amplitude are above a certain threshold, sending a "strobe pulse" to the next stage each time such a signal is detected. This last stage is a Multi-Channel Analyzer (MCA) used in its Pulse Height Analyzer (PHA) mode. There, the 0 to 10V analog input range is linearly mapped to the 0 to 511 digital MCA channels. The MCA digitizes and measures the maximum amplitude value of the incoming signal and stores a count in its corresponding channel. The display of the MCA shows an amplitude size distribution of the detected pulses. Through a RS-232 link, MCA control and data transfer are performed by an IBM compatible PC. Then, the MCA voltage amplitude distribution data is processed and converted to a particle size distribution through the application of Equation 1.8.

2.1.1 DC component of the signal

The characteristics of the signal, taken at the electrodes, are illustrated in Figure 2.2. First, the signal has a standard measured DC component of typically 0.12V testifying to the electrical resistivity introduced by the melt path, by the melt/electrode contact, and most important of all, by the presence of the orifice between the electrodes. Assuming the orifice to be cylindrical, this DC level voltage may be obtained quite simply from integration of Ohm's law [6]. For $L >> D$, the resistance of a cylindrical volume filled with a conductive fluid is given by :

$$R = \frac{4\rho L}{\pi D^2} \qquad \text{Eq 2.1}$$

where R is the electrical resistance of the orifice, ρ is the electrical resistivity of the fluid, L and D are respectively the length and the diameter of the cylindrical orifice. In our case however, because L is comparable to D, it has been shown that $(L + 0.8D)$ should be substituted for L to make an approximate correction for the end effects [6] so that.

$$R = \frac{4\rho\left(L + 0.8D\right)}{\pi D^2} \qquad \text{Eq 2.2}$$

Taking from Table 2.1 the standard electrical conditions for ESZ operation in aluminium melts, the calculated value of the orifice resistance R is $4.4\text{x}10^{-3}$ ohm, corresponding to a DC component voltage level of 0.264V. While the order of magnitude is correct, this calculated value is larger than the standard measured value by a factor two. The error indicates that the geometrical approximation of the orifice to a cylindrical shape is not very good. Because of its smooth shape, the orifice's diameter is only close to D around the central portion of the ESZ, so that only a fraction of the length L, $L_{eff} = \sim 0.3L$ should be used in Eq. 2.2. Physically this makes more sense and the resulting DC voltage value, ~ 0.115V, is closer to the measured value. A value of R can also be obtained by integration of Ohm's law, as was done by Doutre [3] for the calculation of ΔR, when (d/D) approaches one.

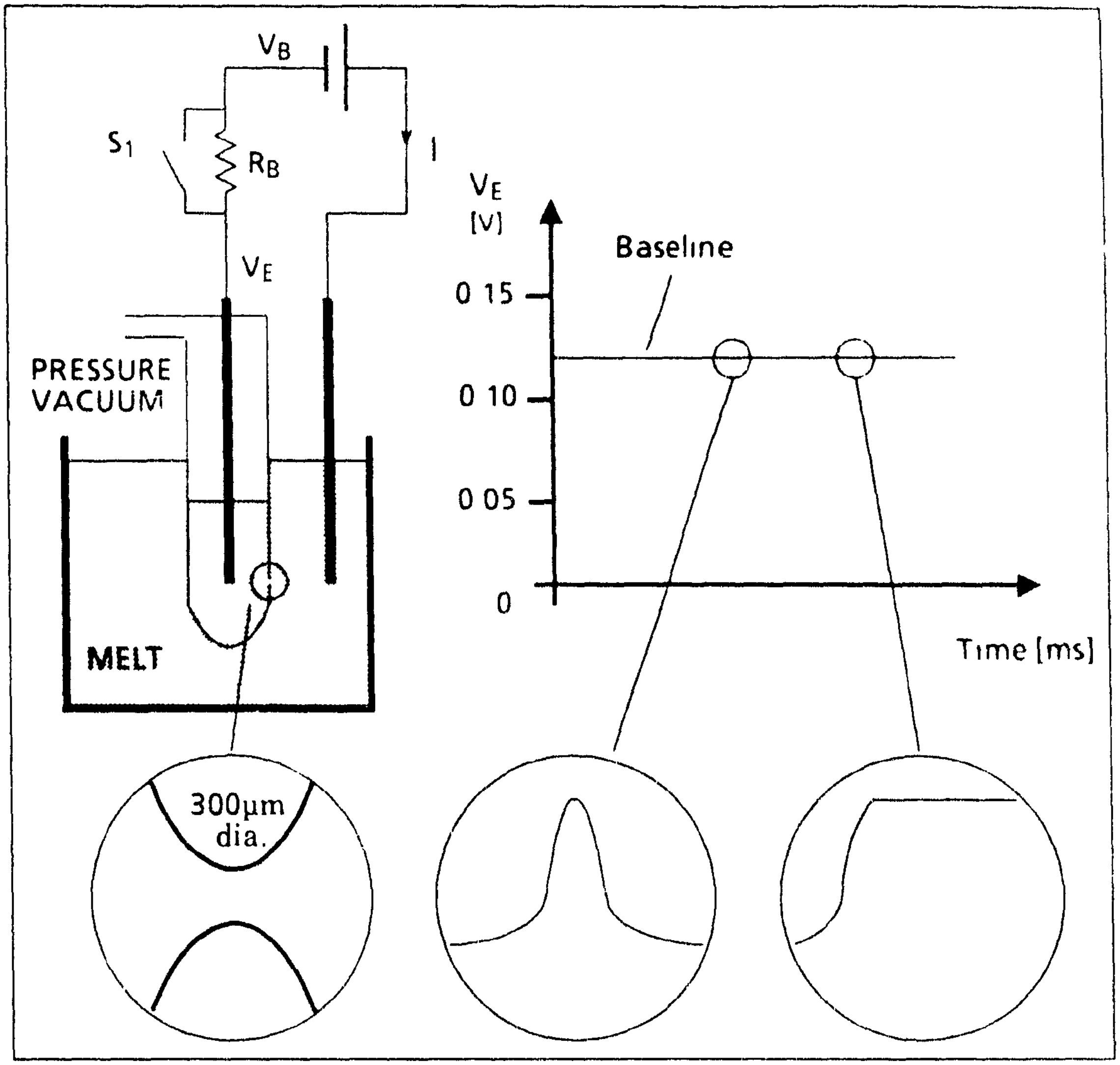

Figure 2 2 Principle of LiMCA operation

2.1.2 AC component

The flat characteristic of the signal's DC component corresponds to moments where no particle is passing through the orifice and is defined as the signal's baseline. Superimposed on the DC level, Figure 2.2 also shows imperceptible variations (transients) that can be attributed to variation in orifice resistivity. Two small fluctuations are enlarged as examples in the figure. The first is a temporary fluctuation of symmetrical shape which is generally related to the passage of a nonconductive particle through the ESZ. The second is a step change in the DC level which can be interpreted as a permanent reduction of the ESZ volume. These types of transients are described in detail in Chapter 4.

Table 2.1
Standard values of ESZ
electrical parameters

PARAMETER	VALUE
V_B	12V
R_b	0.2ohm
I	60A
ρ	0.25×10^{-6} ohm m
D	300μm
L	1mm

As discussed in Chapter 1, Eq.2.3 describes the relation between the pulse amplitude and the equivalent spherical particle size provided that *d*, the diameter of the particle, is much smaller than *D*, the diameter of the orifice.

$$\Delta V = \frac{4\rho I d^3}{\pi D^4} \qquad \text{Eq. 2.3}$$

Taking the values listed in Table 2.1, this last equation may be written :

$$\Delta V[\mu V] = 0.0024\left(d[\mu m]\right)^3 \qquad \text{Eq. 2.4}$$

or, the other way around:

$$d[\mu m] = 7.5\left(\Delta V[\mu V]\right)^{\frac{1}{3}} \qquad \text{Eq. 2.5}$$

Table 2.2 illustrates the order of magnitude of the voltage pulse amplitudes before preamplification for a typical particle size range of 10 to 100 μm, as calculated through Eq. 2.4.

From Table 2.2, it is clear that the amplitudes of the transient values corresponding to the passage of particles through the ESZ are much smaller than the DC level of the signal. As these transients are so small, the AC component of the signals must be amplified (typically by a gain of 1000) before

Table 2.2
Particle size/Pulse amplitude correspondence

Particle size [µm]	pulse amplitude [µV]
10	2 4
20	19.2
30	64 8
40	153.6
50	300.0
60	518 0
70	823.2
80	1228
90	1749
100	2400

any information can be extracted using standard analog electronic circuits. The DC level must be filtered out so that only the AC component is amplified. The removal of the signal's DC component is performed by using a High Pass Filter (HPF), the first signal conditioning stage of the system, as shown in Figure 2.1.

The remaining AC component of the signal is therefore amplified by the preamplifier (gain = 1000) and limited in bandwidth to 10kHz by the Low Pass Filter (LPF) stage. While these two last stages of signal preprocessing do not have a detrimental effect on the original signal, the high pass filter (HPF) does. The effects of the HPF are therefore studied in some detail in the next section.

2.2 High pass filter effects

The high pass filter circuit, also known as AC-coupling, is shown in Figure 2.3. It consists of simple passive first order resistor/capacitor (RC) circuits. Both

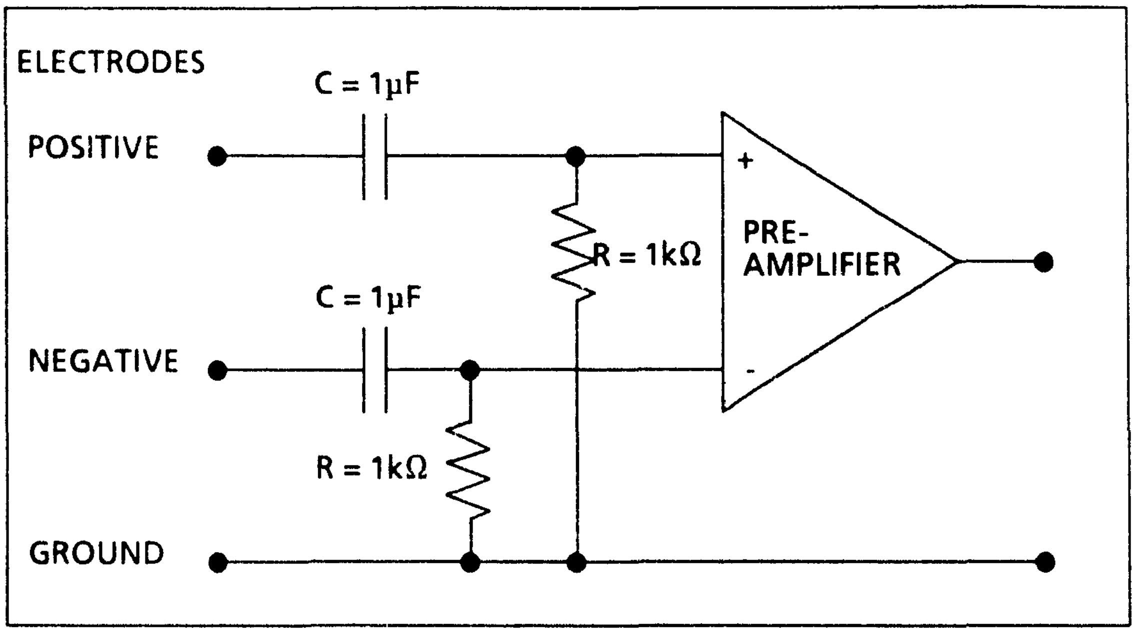

Figure 2.3 High pass filter schematics

the positive and the negative electrodes are connected to the preamplifier device through RC type filters. The capacitor, following the input electrode potential, charges itself at a rate limited by the value of R and C. As a consequence, its potential is not able to follow rapid changes in the signal. Since the potential at the preamplifier input is equal to the input signal minus the potential at the capacitor, only "fast" voltage variations are fed to the preamplifier input while the capacitor is still being charged up. The main design parameter in this circuit is the value of the filter's time constant, the RC product. In the studied case, RC = 1ms.

2.2.1 Effect on real signal

The desirable effect of the AC-coupling circuit is shown in Figure 2.4. The DC component of a typical baseline step transient (dashed line) is filtered out, the falling edge follows a baseline restoration exponential decay of 1ms time constant (solid line). A transient such as the one of Figure 2.4 (solid line) is referred as a *baseline jump*.

Figure 2.5 illustrates an undesirable effect introduced by the AC-coupling on a typical normal ESZ transient. While the input signal (dashed line) to the filter

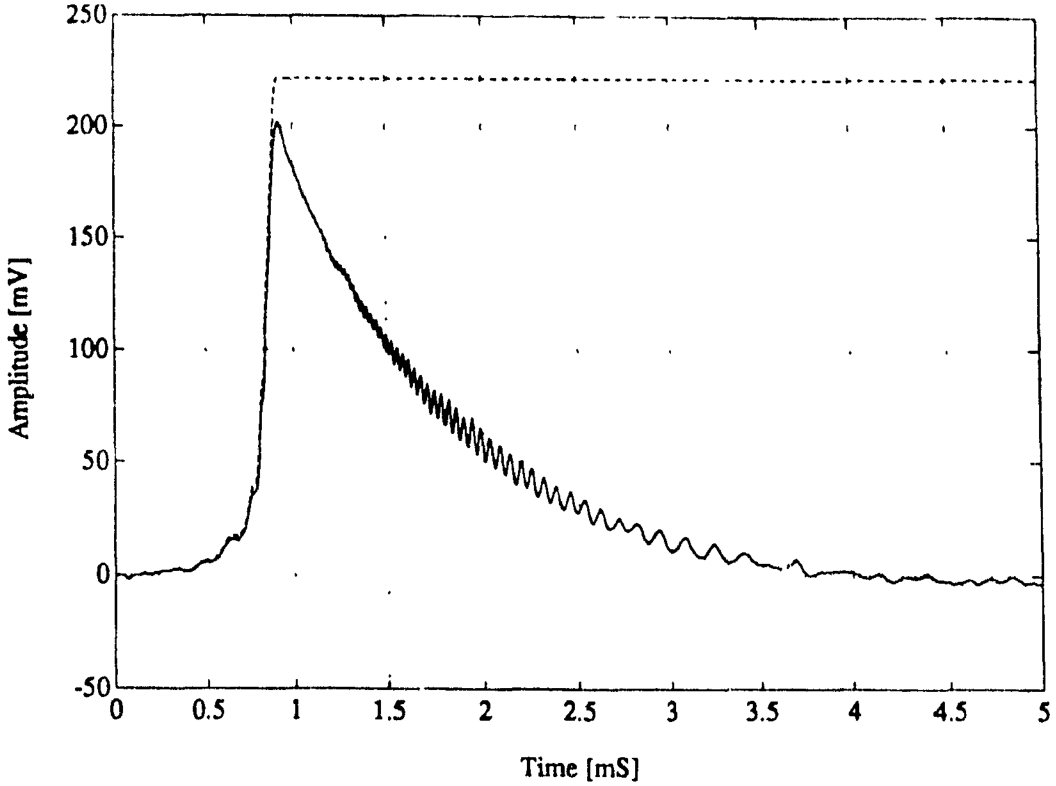

FIGURE 2.4 Typical baseline step transient and corresponding *baseline jump* transient

has a symmetrical bell shape to it, the output transient (solid line) is not symmetrical, exhibiting "under-shoot" at the foot of the falling edge. This is a consequence of the RC filtering circuit.

An even more undesirable effect is the reduction of the output transient's amplitude. This amplitude loss is a function of the RC filter time constant and of the transient frequency content. To get a better understanding of these effects, a mathematical model of the high pass filter transfer function has been derived.

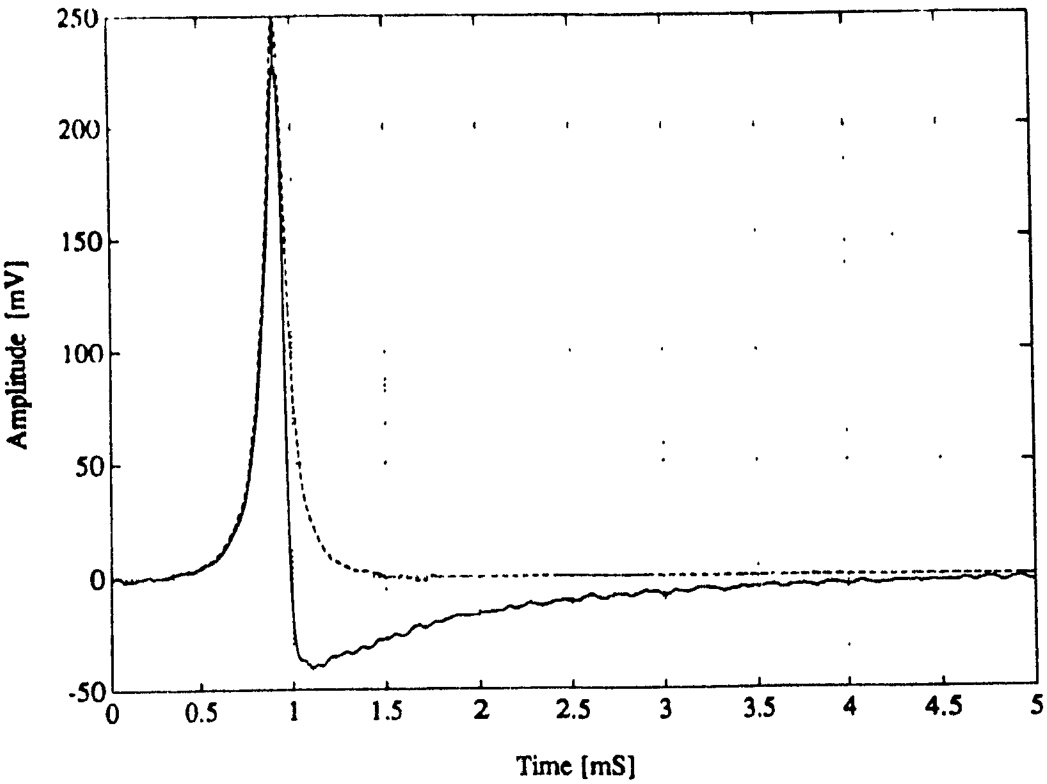

FIGURE 2.5 Typical *normal pulse* transient before and after the high pass filter

2.3 Mathematical model of high pass filter

The purpose of this mathematical model is to allow quantitative estimation of the distortion introduced in the signal by the high pass filter. First, a general analytical solution of the AC-coupling circuit governing differential equation is derived. Then, four different analytical functions are used to model the input transient signals. For each model, a particular analytical solution was found using the input functions and the general solution.

2.3.1 General solution

The differential equation describing the AC-coupling circuit shown in Figure 2.6 can easily be derived using Equations 2.6 a), b) and c).

$$i_c(t)=C\frac{dv_c(t)}{dt} \qquad \text{Eq. 2.6 a)}$$

$$v_2(t)=R\,i_c(t) \qquad \text{Eq. 2.6 b)}$$

$$v_c(t)=v_1(t)-v_2(t) \qquad \text{Eq. 2.6 c)}$$

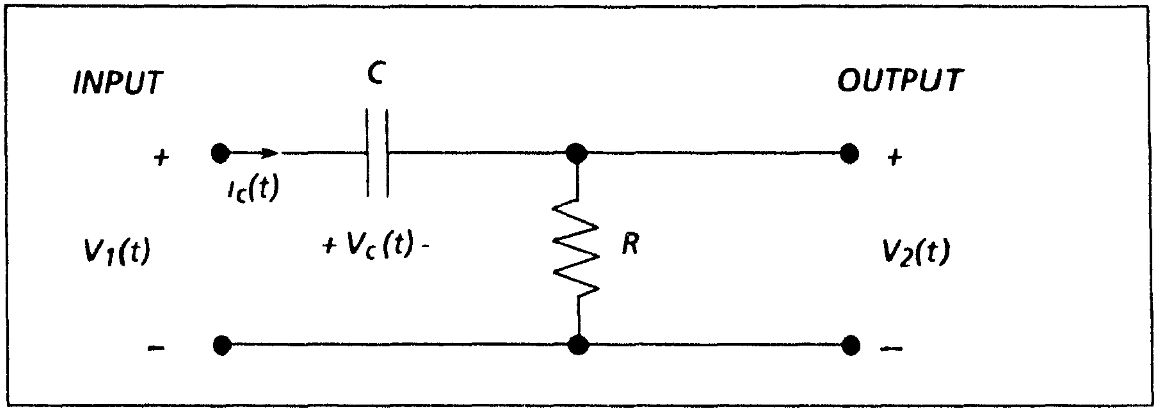

Figure 2.6 AC coupling circuit

Eq. 2.6 a) and b) respectively represent the potential at the capacitor C, and the potential at the output of the AC-coupling circuit. Equation 2.6 c) is obtained through Kirchhoff first law, which stipulates that the sum of potentials around a closed loop is equal to zero. Substituting Eq. 2.6 c) in Eq. 2.6 a) gives Eq. 2.7.

$$i_c(t)=C\frac{d}{dt}\left(v_c(t)+v_c(t)\right) \qquad \text{Eq. 2.7}$$

Substitution of Eq. 2.7 in Eq. 2.6 b) and derivation of the resulting equation gives the following differential equation :

$$\frac{dv_2(t)}{dt}+\omega v_2(t)=\frac{dv_1(t)}{dt} \qquad \text{Eq. 2.8}$$

where

$$\omega=\frac{1}{RC} \qquad \text{Eq. 2.9}$$

Integration of Eq.2.8 is readily achieved by first multiplying both sides by $e^{\omega t}$:

$$e^{\omega t}\frac{dv_2(t)}{dt} + \omega e^{\omega t}v_2(t) = e^{\omega t}\frac{dv_1(t)}{dt} \qquad \text{Eq. 2.10}$$

The left hand side of Eq. 2.10 is the derivative of $e^{\omega t} v_2(t)$, so that :

$$\frac{d}{dt}\left[e^{\omega t}v_2(t)\right] = e^{\omega t}\frac{dv_1(t)}{dt} \qquad \text{Eq. 2.11}$$

Taking the integration on both sides ,

$$\int_{t_0}^{t}\frac{d}{d\iota}\left[e^{\omega\iota}v_2(\iota)\right]d\iota = \int_{t_0}^{t} e^{\omega\iota}\frac{dv_1(\iota)}{d\iota}d\iota \qquad \text{Eq. 2.12}$$

yielding

$$e^{\omega t}v_2(t) - e^{\omega t_0}v_2(t_0) = \int_{t_0}^{t} e^{\omega\iota}\frac{dv_1(\iota)}{d\iota}d\iota \qquad \text{Eq. 2.13}$$

so that, the output voltage can be expressed as :

$$v_2(t) = e^{-\omega\left(t-t_0\right)}v_2(t_0) + \int_{t_0}^{t} e^{-\omega(t-\iota)}\frac{dv_1(\iota)}{d\iota}d\iota \qquad \text{Eq. 2.14}$$

this being the general solution to the problem.

2.3.2 Particular solutions

As mentioned previously, filtering effects are function of the transient's frequency content. In the process of modeling the particular input signals, the frequency content must be evaluated. A simple way to do this is to measure the pulse half height width (in time units) and approximate the transient shape by a simple geometrical function. The variable b will represent the pulse half height width.

2.3.2.1 Rectangular pulse model

This first model is certainly not realistic in describing the LiMCA bell pulse shape fed to the filter's input. However, for a square pulse signal at the filter input, the calculated output gives a good insight into the effect of the high pass filter. A typical pulse half height width b, equal to 0.2ms was chosen to illustrate its effect.

The rectangular pulse illustrated in Figure 2.7 can be characterized by the following equations.

$$v_1(t) = 0 \ , \ for\, t < t_i \qquad \text{Eq. 2.15 a)}$$

$$v_1(t) = a \ , \ for\, ti \le t < t_i + b \qquad \text{Eq. 2.15 b)}$$

$$v_1(t) = 0 \ , \ for\, t \ge t_i + b \qquad \text{Eq. 2.15 c)}$$

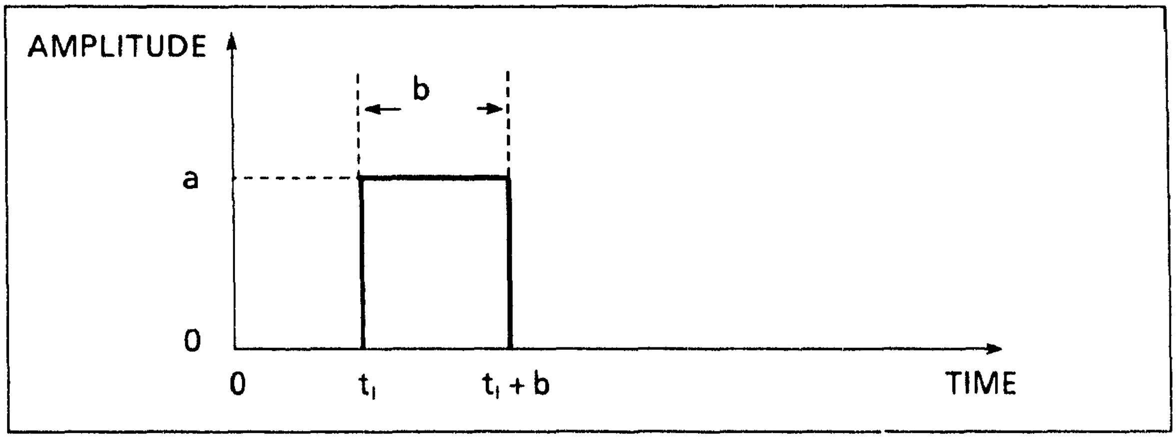

Figure 2.7 Rectangular pulse model

The particular solution for this case is calculated by substituting Eq. 2.15 in the general transfer function solution, Eq. 2.14. The model is a discontinuous function of three individual continuous time segments. Each segment is substituted in the general solution equation with the initial conditions given by the previous segment solution. Following this procedure, it was found that :

$$v_2(t) = 0 \ ; \ for\, t < t_i \qquad \text{Eq 2 16a)}$$

$$v_2(t) = a e^{-\omega\left(t - t_i\right)} \ ; \ for\, t_i \le t < t_i + b \qquad \text{Eq. 2.16b)}$$

$$v_2(t) = a\left|e^{-\omega\left(t-t_1\right)} - e^{-\omega\left(t-t_1-b\right)}\right| \quad , \ for\ t \geq t_1 + b \qquad \text{Eq. 2.16c)}$$

The input and the output functions are plotted in Figure 2.8 for the typical case where :

$$RC = 1.0\,\text{ms}$$
$$b = 0.2\,\text{ms}$$

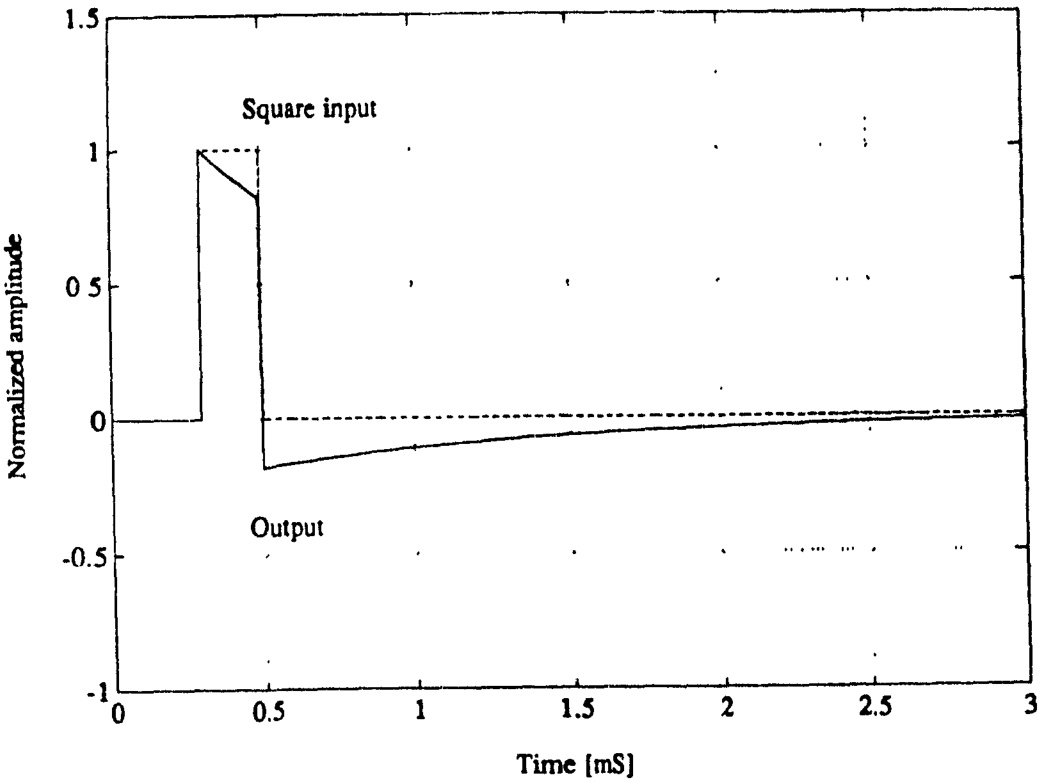

Figure 2.8 Calculated response for the rectangular pulse model

The figure clearly illustrates that DC removal affects both the peak section and the falling edge foot of the pulse. Sharp edges (high frequency content) are not affected at all. The peak DC section is filtered out following an exponential decay until the falling edge is met. The edge being not affected, the falling step value of the output signal must be equal to that of the input signal. Consequently the output signal must go negative at the foot of the falling edge and then recover to zero baseline level, following the exponential 1ms time constant pattern.

This model is a rough approximation of a real transient but has the benefit of clearly illustrating the under-shoot effect.

.3.2.2 Triangular pulse model

A triangle pulse model is much more realistic in describing a raw LiMCA bell pulse shape fed to the filter's input. Its output gives a good idea of the effect of the high pass filter on a typical LiMCA pulse of 0.2 ms width. The triangular pulse can be characterized by Eq.2.17 as shown in Figure 2.9.

$$v_1(t) = 0 \ , \ for\, t < t_i \qquad \text{Eq. 2.17a)}$$

$$v_1(t) = \frac{a}{b}\left|t - t_i\right| \ , \ for\, t_i \le t < t_i + b \qquad \text{Eq. 2.17b)}$$

$$v_1(t) = -\frac{a}{b}\left|t - \left(t_i + 2b\right)\right| \ , \ for\, t_i + b \le t < t_i + 2b \qquad \text{Eq 2.17c)}$$

$$v_1(t) = 0 \ , \ for\, t \ge t_i + 2b \qquad \text{Eq. 2.17d)}$$

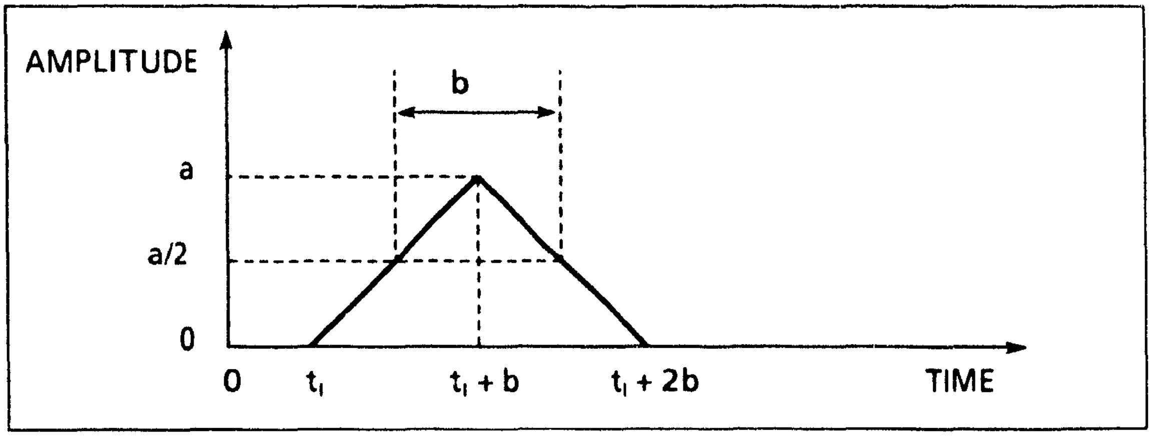

Figure 2.9 Triangular pulse model

Again, the particular solution for this case is calculated by using Eq. 2.17 with the general transfer function solution, Eq. 2.14. The general solution will be applied to each individual continuous segment using an initial condition given by the previous segment solution.

The solution is :

$$v_2(t) = 0 \quad ; \; for\, t < t_i \qquad \text{Eq. 2.18a)}$$

$$v_2(t) = \frac{a}{\omega b}\left|1 - e^{-\omega\left(t - t_i\right)}\right| \quad , \; for\, t_i \leq t < t_i + b \qquad \text{Eq. 2.18b)}$$

$$v_2(t) = \frac{a}{\omega b}\left|2e^{\omega\left(t - t_i - b\right)} - e^{-\omega\left(t - t_i\right)} - 1\right| \quad ; \; for\, t_i + b \leq t < t_i + 2b \qquad \text{Eq. 2.18c)}$$

$$v_2(t) = \frac{a}{\omega b}\left|2e^{-\omega\left(t - t_i - b\right)} - e^{-\omega\left(t - t_i\right)} - e^{-\omega\left(t - t_i - 2b\right)}\right| \quad for\, t \geq t_i + 2b \qquad \text{Eq. 2.18d)}$$

This output function as well as the corresponding input function are plotted in Figure 2.10 for the typical case where

RC = 1.0 ms

b = 0.2 ms

Here, both the amplitude loss and the under-shoot depth distortion features are clearly observed. Their magnitude in relation with the input maximum amplitude are respectively 9% and 16%. The amplitude loss and the Under-Shoot Depth (USD) are functions of the RC time constant and the parameter *b*. They are given below, both in direct and percentage form. The *%LOSS* is given by dividing the function *LOSS* by the amplitude *a* and multiplying the result by 100. The *%USD* function is obtained in a similar manner.

Amplitude loss function:

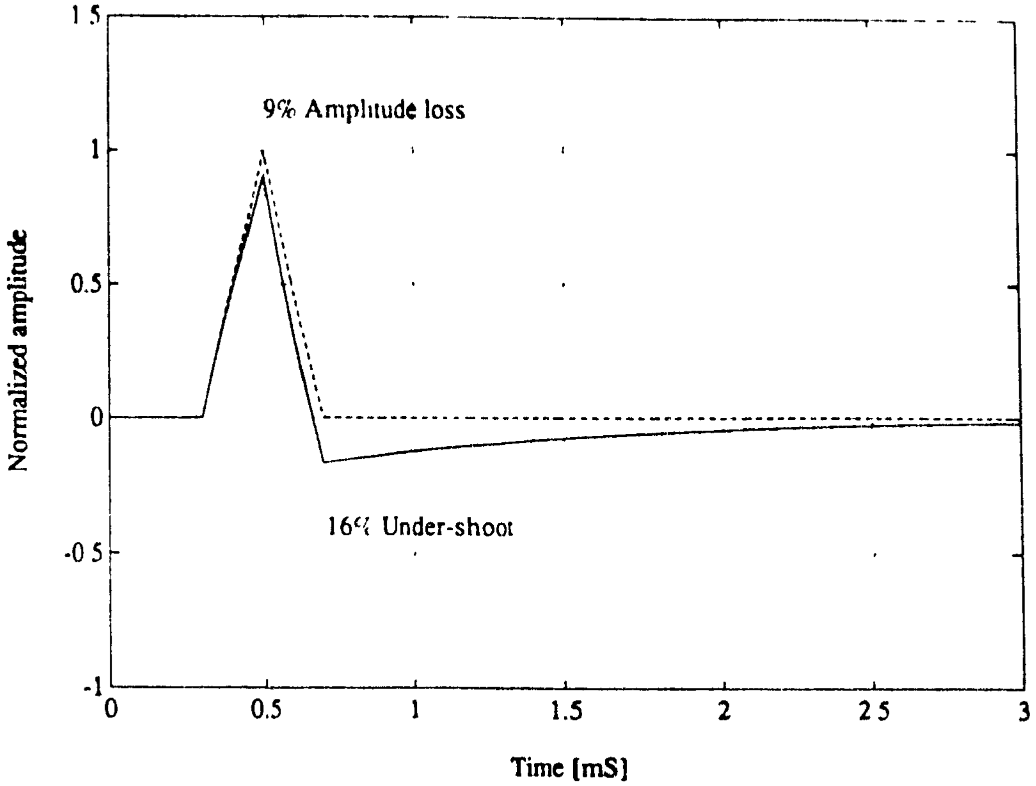

Figure 2.10 Calculated response for the triangular pulse model

$$LOSS = a - v_2\left(t_i + b\right) \qquad \text{Eq. 2.19}$$

$$\%LOSS = \frac{100}{\omega b}\left|\omega b + e^{-\omega b} - 1\right| \ , \ for \ a = 1 \qquad \text{Eq 2.20}$$

Under-Shoot Depth function :

$$USD = -v_2\left(t_i + 2b\right) \qquad \text{Eq. 2.21}$$

$$\%USD = \frac{-100}{\omega b}\left|2e^{-\omega b} - e^{-2\omega b} - 1\right| \ , \ for \ a = 1 \qquad \text{Eq. 2.22}$$

2.3.2.3 Baseline step triangular pulse model

Applying the triangular model used for pulses to baseline jump signals is realistic. In fact, the original baseline jump signal before filtering, is a fast rising edge followed by a DC level equal to the maximum value of rising edge. The baseline jump transient may be modeled by Eq. 2.23 as shown in Figure 2.11.

$$v_1(t) = 0 \quad , \; for \; t < t_i \qquad \text{Eq. 2.23a)}$$

$$v_1(t) = \frac{a}{b}\left| t - t_i \right| \quad , \; for \; t_i \leq t < t_i + b \qquad \text{Eq. 2.23b)}$$

$$v_1(t) = a \quad , \; t \geq t_i + b \qquad \text{Eq. 2.23c)}$$

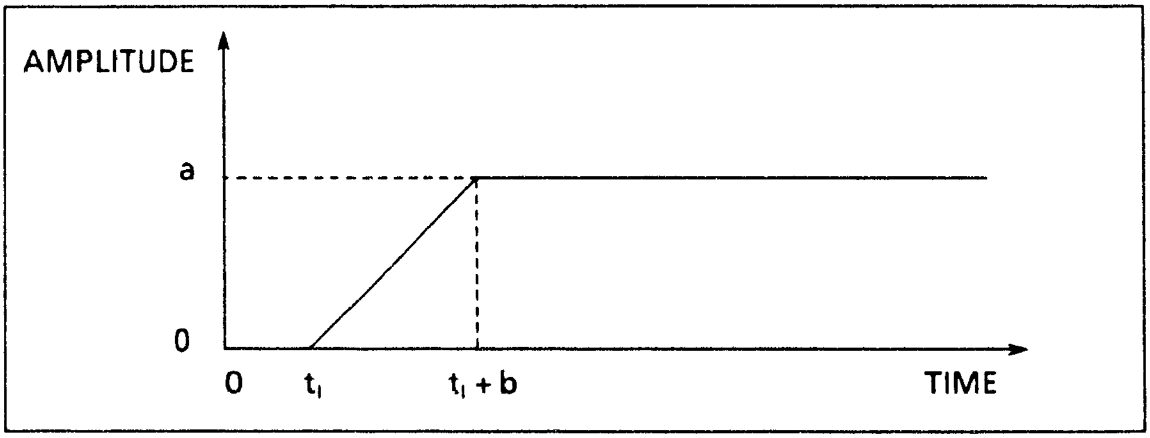

Figure 2 11 Triangular baseline step model

Again , the particular solution is calculated individually for each continuous function segment.

The solution is :

$$v_2(t) = 0 \quad ; \; for \; t < t_i \qquad \text{Eq. 2.24a)}$$

$$v_2(t) = \frac{a}{\omega b}\left| 1 - e^{-\omega\left(t - t_i\right)} \right| \quad , \; for \; t_i \leq t < t_i + b \qquad \text{Eq. 2.24b)}$$

$$v_2(t) = \frac{a}{\omega b}\left| e^{-\omega\left(t-t_1-b\right)} - e^{-\omega\left(t-t_1\right)} \right| \quad , \text{ for } t \geq t_1 + b \qquad \text{Eq 2 24c)}$$

Figure 2.12 shows input and output functions for the typical case where :

$$RC = 1.0 \text{ ms}$$
$$b = 0.2 \text{ ms}$$

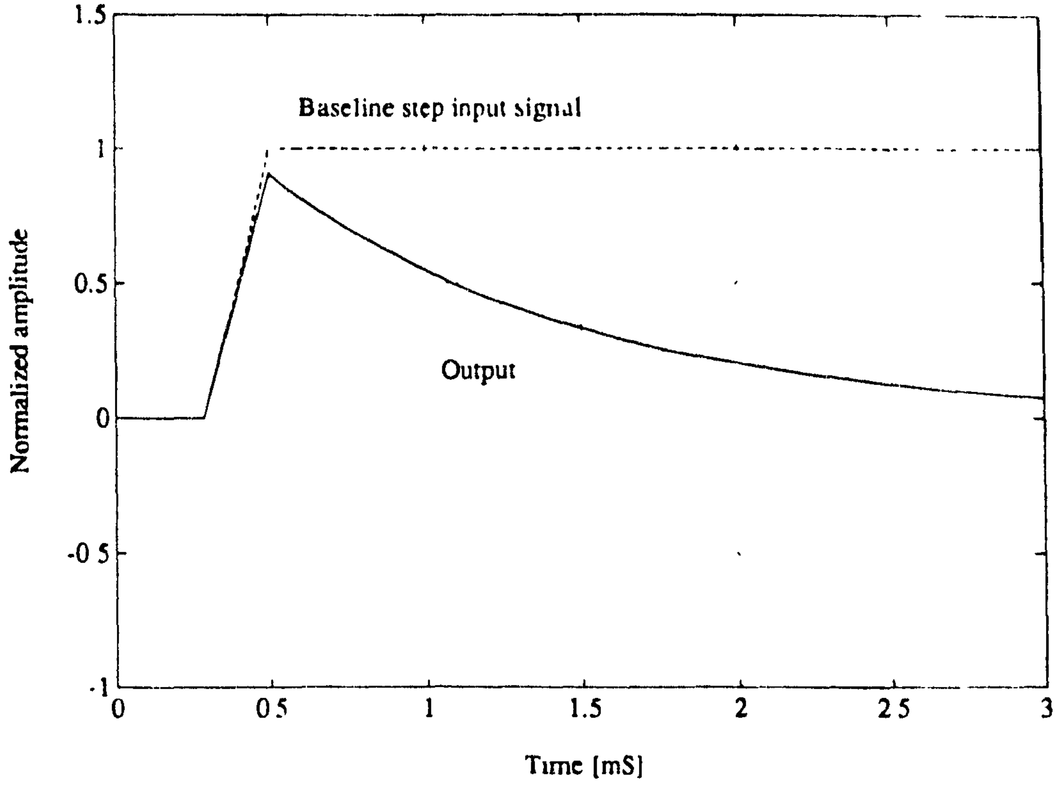

Figure 2.12 Calculated response for the baseline step triangular model

As for pulse modeling, the baseline step transient suffers the same amplitude loss at its peak level. The non-zero baseline level is filtered out following the 1ms time constant exponential decay. The real baseline step signal behaves in a very similar manner, as was previously shown in Figure 2.4.

2.3.2.4 Sine pulse model

A sine pulse model is closer to the real LiMCA signal than is the triangle pulse model. The input model function is given by Eq. 11 and is shown in Figure 2.13.

$$v_1(t) = 0 \quad , \; for\, t < t_i \qquad \text{Eq. 2.25a)}$$

$$v_1(t) = \frac{a}{2}\left[1 + \cos\left\{\frac{\pi}{b}\left(t - t_i\right) + \pi\right\}\right] \quad ; \; for\, t_i \le t < t_i + 2b \qquad \text{Eq. 2.25b)}$$

$$v_1(t) = 0 \quad , \; for\, t \ge t_i + 2b \qquad \text{Eq. 2.25c)}$$

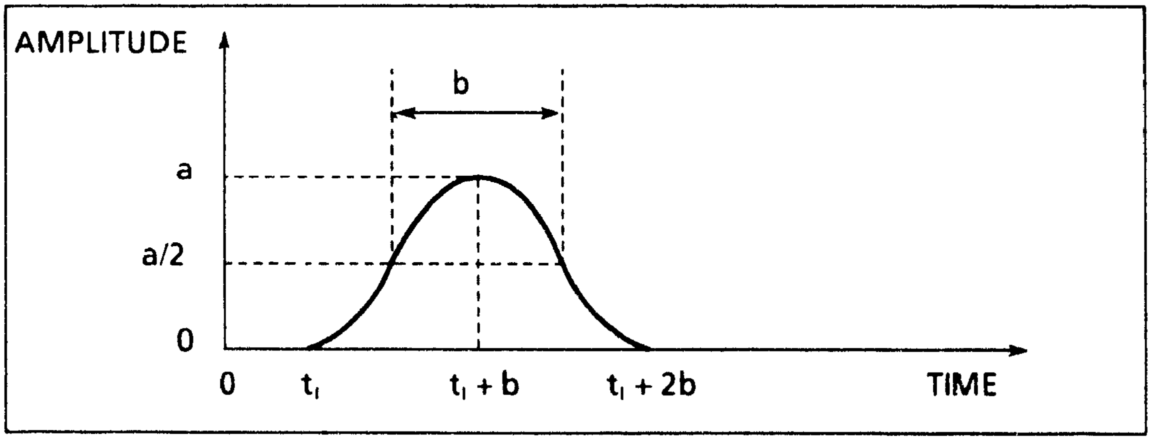

Figure 2 13 Sine pulse model

As for other models, the particular solution is calculated by segment. The solution is :

$$v_2(t) = 0 \quad , \; for\, t < t_i \qquad \text{Eq. 2.26a)}$$

$$v_2(t) = \frac{a}{2}\frac{\pi^2}{\left(\omega b\right)^2 + \pi^2}\left[e^{-\omega\left(t - t_i\right)} - \cos\frac{\pi}{b}\left(t - t_i\right) + \frac{\omega b}{\pi}\sin\left(t - t_i\right)\right] ; for\, t_i \le t < t_i + 2b$$

$$\text{Eq. 2.26b)}$$

$$v_2(t) = \frac{a}{2}\frac{\pi^2}{\left(\omega b\right)^2+\pi^2}\left|e^{-\omega\left(t-t_i\right)}-e^{-\omega\left(t-t_i-2b\right)}\right| \quad , \; for\, t \geq t_i + 2b \qquad \text{Eq 2.26c)}$$

Again, the input and the output filter signals are plotted in Figure 2.14 for the typical case where :

RC = 1.0 ms
b = 0.2 ms

As seen, the characteristics of the output signal are the same as those for the triangular pulse model. Moreover, the maximum amplitude loss and under-shoot depth percentage values are the same as for the triangular pulse model, being 9% and 16% respectively. One can conclude that, for this case (RC = 1ms ,b = 0.2 ms), the triangle and sine models produce the same results for estimates of amplitude loss and the under-shoot depth distortions.

Amplitude loss function:

$$\%LOSS = a\left|1-\frac{1}{2}\frac{\pi^2}{\left(\omega b\right)^2+\pi^2}\left(e^{-\omega b}+1\right)\right| \times 100 \qquad \text{Eq 2 27}$$

Under-shoot depth function:

$$\%USD = \frac{-a}{2}\frac{\pi^2}{\left(\omega b\right)^2+\pi^2}\left|e^{-2\omega b}-1\right| \times 100 \qquad \text{Eq. 2 28}$$

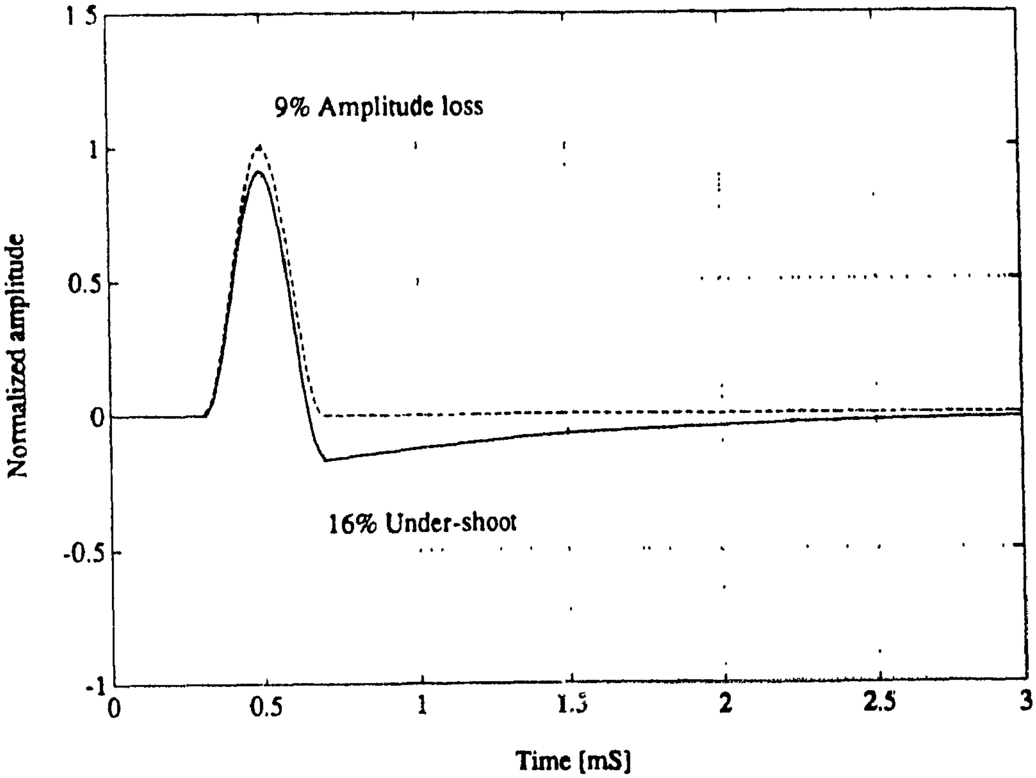

Figure 2.14 Calculated response for the sine pulse model

2.3.3 Amplitude loss and under-shoot depth versus the time constant

Figure 2.15 shows a plot of the amplitude loss and the under-shoot depth for both the triangle and sine models as a function of the filter's RC time constant. Obviously, both models behave similarly. In selecting a value for the AC-coupling time constant, one wants to minimize the distortions introduced on a pulse (with *b* equal to 0.2ms). For both models, the amplitude loss and the under-shoot depth curves approach zero % for AC-coupling time constant greater than 0.15ms. Consequently, for values of RC greater than 0.15ms, the higher the time constant, the weaker the effects on the incoming pulse. On the other hand, what this graph fail to show is that a higher time constant value increases the time required to restore the baseline to the zero level. This is not desirable since the purpose of the high pass filter is to restore the baseline to the zero level as fast as possible. Consequently, the value of RC = 1ms represents a good tradeoff between moderate distortion and moderate baseline recovery time interval.

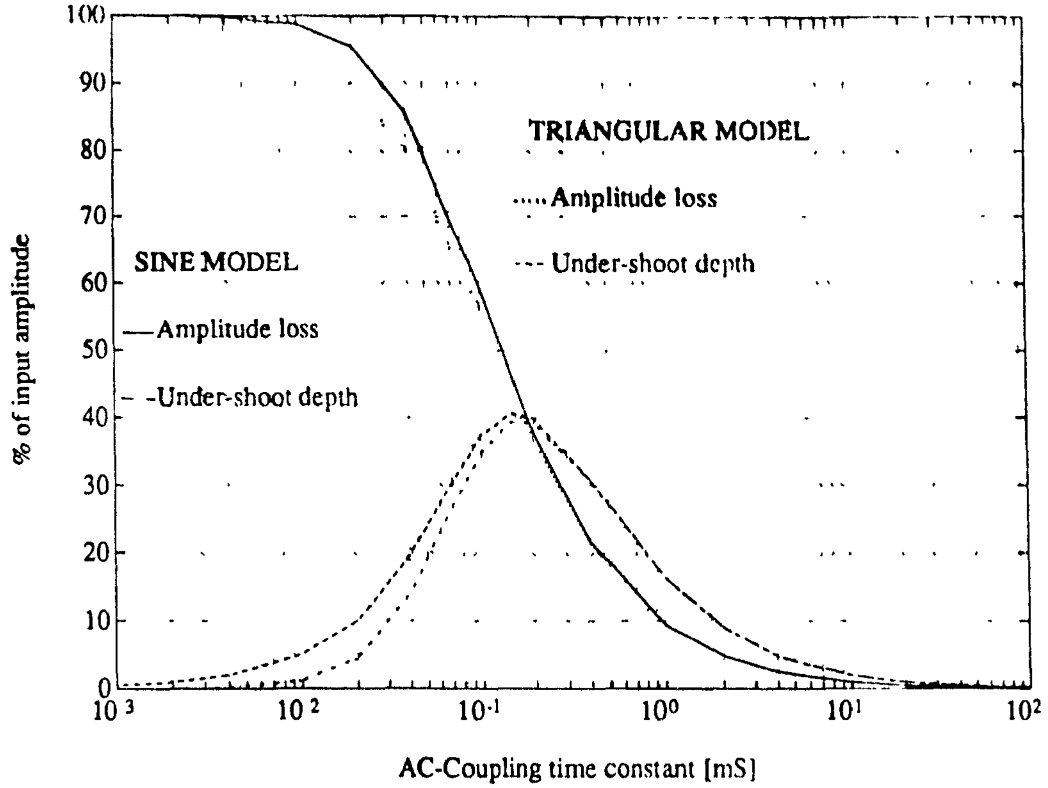

Figure 2.15 Amplitude loss and under shoot depth, as a function of RC, the time constant, for $b = 0.2$ms

2.3.4 Distortion effects versus pulse half height width

So far, pulse distortion effects have been studied only varying the value of RC, keeping *b* constant and equal to 0.2ms. While RC is a fixed parameter for the signal studied, the value of *b* (the half height width of the pulse) is not. In exceptional circumstances, where the melt flow rate through the orifice would be increased, *b* may be slightly smaller (down to 0.1ms). On the other hand, *b* will frequently be larger; for example when the flow rate through the orifice is slowed down, the particle spends more time in the ESZ, and thus *b* is increased. In practice, values of *b* up to 3ms have been observed.

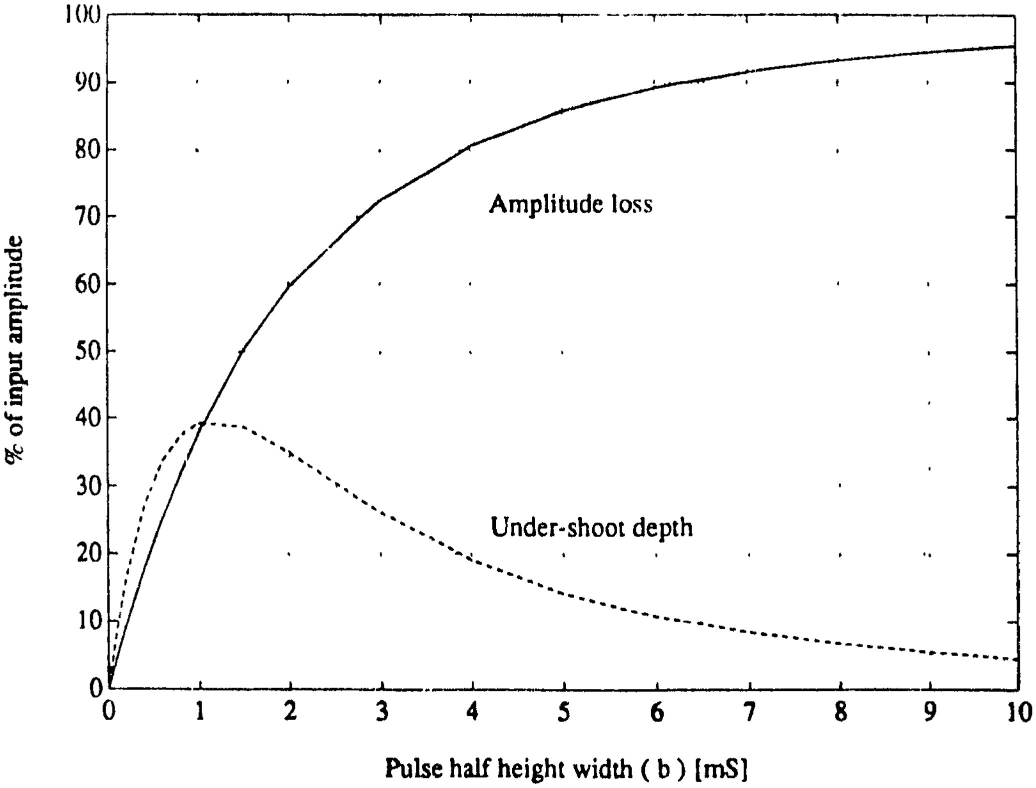

Figure 2.16 Amplitude loss and under-shoot depth,
as a function of *b*,
for the sine model with RC = 1ms

We should now consider the distortion effects of the high pass filter on the produced transients as a function of *b*, the pulse half height width. Figure 2.16 shows plots of the amplitude loss function and the back shoot depth function of the sine model versus the parameter b. This graph illustrates that the amplitude loss asymptotically increases towards 100% with increasing values of b, while the under-shoot depth reaches its maximum value at $b = 1.0$ms. As a consequence, a transient with a value of b equal to 1.5ms, like in the case of Figure 2.17, yields an amplitude approximately 50% smaller than the original input transient.

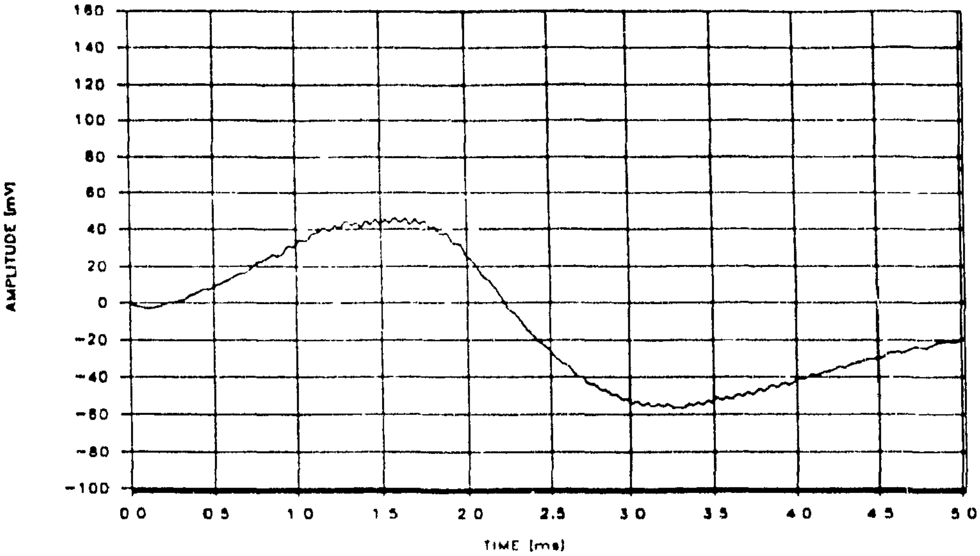

Figure 2 17 Example of real, large half height width pulse

2.4 Discussions

2.4.1 Usage of the high pass filter models

The mathematical models of the high pass filter bring important quantitative descriptions of the filter's transfer function. While the rectangular model is only of academic value, the triangular and sine models can be useful in practice, the sine model being the most realistic model in describing observed pulses. Its relatively higher mathematical complexity compared to the triangular model is not an important inconvenience since in practice, one only wants to estimate the amplitude loss percentage of a pulse through Eq. 2.27, given the half height width of the pulse, b, and the cutoff frequency of the filter, ω.

The sine model can be used at different levels of complexity to correct the measured amplitude of incoming pulses. At a first and lower level, one would assume all pulses have a value of *b* equal to 0.2ms. This was discussed in Section 2.3.3 and showed in Figure 2.14. With the standard 1ms filter time constant, the output transient amplitude is 9% smaller than the input amplitude. A global amplitude correction is performed by multiplying all measured pulse amplitudes by a factor equal to 1.099. This process restores the original transient size distribution from which the particle size distribution is calculated.

At a second level of complexity, for each incoming pulse, one would measure the value of *b*, calculate the correction factor using Eq. 2.27 and apply it to the measured pulse amplitude. Such a process is the first step towards an automatic validation of the particle size distribution. The benefit of this procedure is that it can handle situations where a reduced melt flow rate through the ESZ causes transients to be stretched in time (i.e. higher values of *b*). On the other hand, extra measurement has to be performed since both the amplitude and the parameter *b* must be measured for each detected transient.

2.4.2 Behaviour of signal analysis system

The signal processing performed by the signal analysis system has been briefly described in the last paragraph of Section 2.1. At this point, some of its features are described to illustrate its limitation to eventual improvements.

The peak detection circuit, the "peak detector" of Figure 2.1, is implemented by a Tracor-Northern TN-1246 Pulse sampler. It is an analog electronic device with a positive threshold level crossing trigger system. When the positive slope of an incoming transient activates the trigger, the circuit generates a strobe pulse when a maximum is detected. The trigger circuit can be reactivated only when the negative slope of the signal crosses the threshold level again. If many local maxima are present in the transient, only the first one will be detected.

Both the transient and the strobe signals are fed to the Multi-Channel Analyzer (MCA of Figure 2.1). The amplitude of the detected maximum is measured by the MCA and a count is recorded in the corresponding channel. Accumulation of these counts over a period of time (typically 30-45 seconds), produces a pulse amplitude distribution. The conversion of this data into a particle size distribution is performed by a IBM-PC compatible computer. This conversion is based on Eq. 1.8 and on the assumption that all detected pulses were related to the passage of a particle through the ESZ. This assumption is valid if the signal baseline is stable, which is usually the case with signal generated by an ESZ probe in aluminium melts. However, unstable signal baseline are common in specific circumstances and this is discussed in Section 5.4.

The main limitation of this signal analysis system is the lack of information collected about each individual transient. Indeed, only the amplitude of a transient is extracted. Since *b* is not, and cannot be measured with this system, it is not possible to implement corrections to individual pulse amplitude value as suggested in Section 2.4.1. This is also the reason why each pulse has to be interpreted as being produced by the passage of a particle through the ESZ. With industrially obtained signals, this assumption can be highly detrimental to the particle size distribution reliability when pulses of unknown source are present in the LiMCA signal. Thus, improvement of the signal analysis system can only be achieve if the previously described analog electronic system is replaced by a more sophisticated one. With today's digital electronic hardware, a signal analysis system based on digital signal processing techniques would offer the computing power and software flexibility to fulfill the realtime task of detecting and extracting parameters from each individual pulses.

CHAPTER 3 -- EXPERIMENTAL PROCEDURES AND INSTRUMENTATION SETUP

The LiMCA transient classification described in this thesis is based on a bank of signal recorded for this purpose. Instrumentation setups and analysis procedures have been designed to retrieve the information from the tapes and allow for observation, display, capture, processing and plotting of the transients.

In this chapter, the instrumentation setups and the experimental procedures used to obtain the results discussed in Chapters 4 and 5 are described in detail.

3.1 Introduction to experimental procedures

The recording on tape of pertinent signals (i.e. signals generated under known conditions by Alcan's LiMCA system) were carried out on two independent occasions. The first took place in a laboratory environment, in November 1986. The LiMCA system was operated in melts contained in a small lab furnace. During this session, six tape reels were used to record LiMCA signals under ideal ESZ operating conditions. The second took place in June of 1987. At that time, in-plant performances of the LiMCA equipment were recorded on eight tape reels, with ESZ operating conditions producing different degrees of LiMCA signal baseline instability.

The transients were retrieved from the tape using a digital oscilloscope. Digitized signal transients were transferred and stored on disks through an host IBM-PC compatible computer. Plotting of digitized transients was possible either directly from the oscilloscope to a strip chart recorder or from the PC to a hard copy device such as a printer or a plotter. Off-line observation of signals allowed easy identification of the different types of transients present in the signal

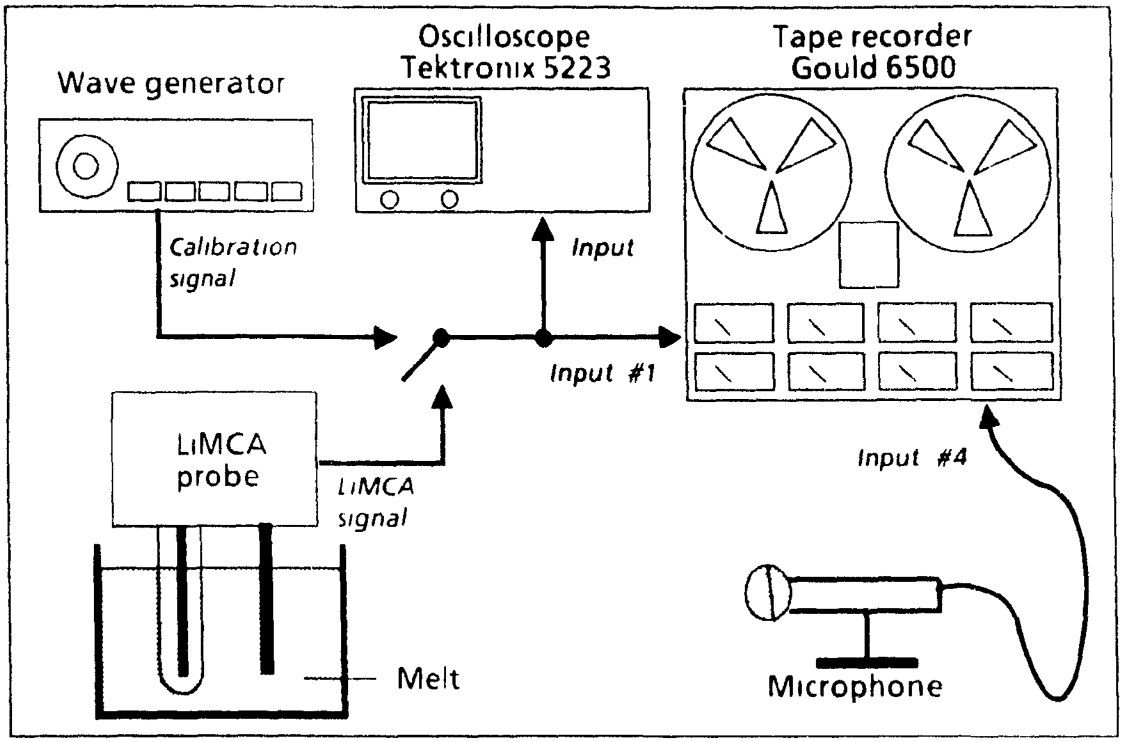

Figure 3 1 Recording setup

Two types of semi-quantitative analysis were also carried out following observation of specific sections of the tapes. First, a "Transient Type Frequency Occurrence" analysis was carried out. This procedure estimates the proportional occurrence of each type of transient as a function of time. For the case of highly unstable signals, a "Stability Time Interval Evaluation" was also performed in order to measure the time interval required for the signal to become "completely unstable" after the occurrence of a conditioning current. These analysis were designed to render qualitative evaluation of the ESZ's performance, as well as to test, for different operating situations, the reliability of the generated particle size distribution. These two analysis techniques are described in more detail in Section 3.5 and Section 3.6 respectively.

3.1.1 Review of recording/play back procedures

Two different experimental setups were used. These are identified as the "Recording Setup" and the "Play back Setup" and are illustrated in Figures 3.1 and 3 2 respectively

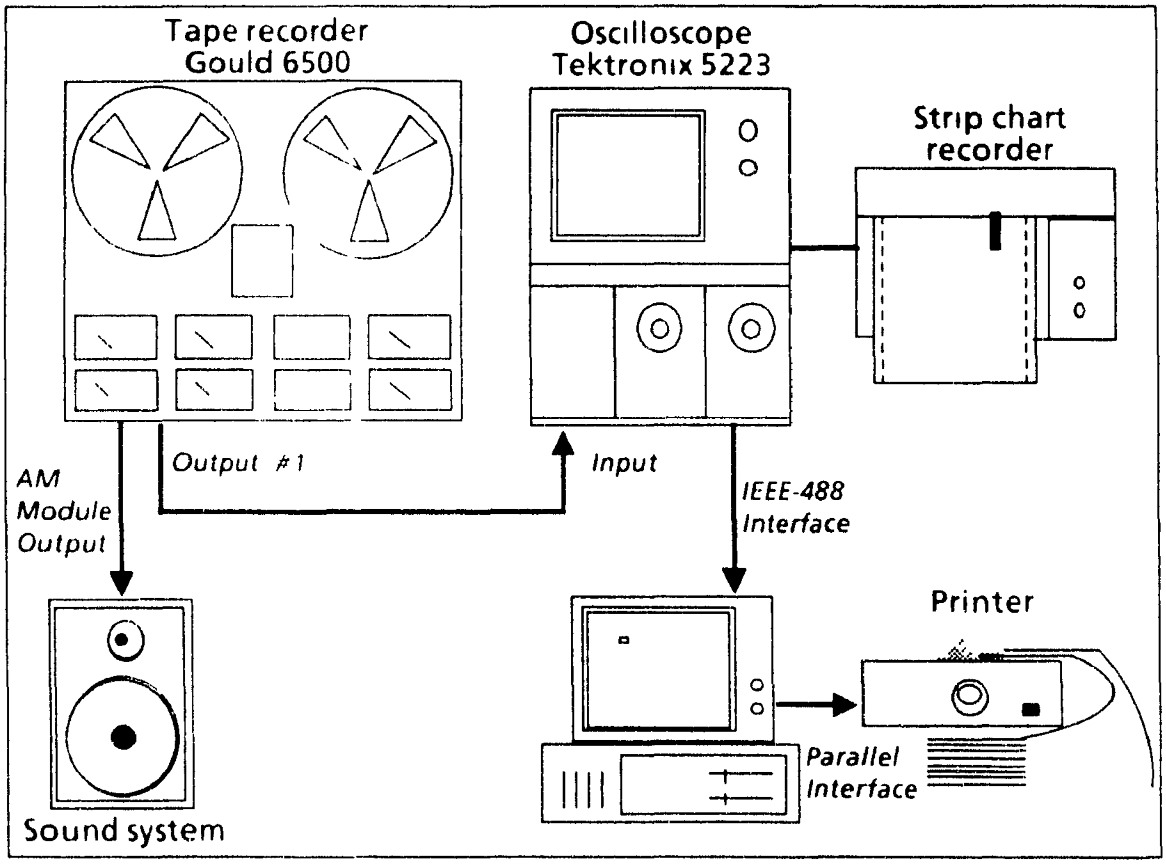

Figure 3 2 Play back setup

In the Recording Setup (Figure 3.1), the LiMCA's output signal was transmitted to the oscilloscope input as well as to the tape recorder's FM (Frequency Modulation) input module #1. For tape calibration purposes, the input of this FM module could also be connected to the output of a waveform generator. A microphone was connected to the input of the AM (Amplitude Modulation) module of the tape machine so that the operator could "speak" to identify different situations.

In the play back setup (Figure 3.2), the output of the FM module #1 was connected to the oscilloscope's preamplifier module input. The output of the AM module was connected to a sound system so that recorded spoken information could be heard. This way, elements of the recording context were reminded to the operator. The oscilloscope Display Output Terminal, when connected to a Strip Chart Recorder, allowed direct plotting of signals displayed on the oscilloscope screen. The oscilloscope was also connected to an IBM-PC compatible computer through an IEEE-488 interface bus, enabling transfer of digitized signals to the computer. The PC itself was also connected to a dot matrix printer and/or a plotter so that better quality hardcopy of the signal could be obtained

3.2 Description of instruments

In this section, important features of the instruments used, together with their application to the experiments carried out are considered.

3.2.1 Frequency Modulation (FM) Tape Recorder

The tape machine used for the experiments described was a GOULD 6500 model, kindly lent by Alcan's Arvida laboratories It was a 1/4 inch tape, seven inch reel FM multi track tape recorder machine. Although it can be configured with up to eight tracks, the unit used was equipped with only four input/output modules, three of which were FM modules while the fourth was an Amplitude Modulation (AM) module. The machine also had variable speed capabilities, offering five selections, i e. 30, 15, 7.5, 3.75 and 1.875 ips (inches per second).

The use of such a high quality tape machine (often referred to as an instrumentation recorder) was a key element to the success of this work. In essence, the frequency response of standard (AM) tape recorders are inadequate. The band width of the LiMCA signal is from 0Hz to 10kHz. At the time of the experiments, only FM tape recorders could reproduce such signal with high fidelity, particularly in the low frequency range. Now, today's instrumentation DAT (Digital Audio Tape) recorders would be even better.

The other useful feature of the Gould 6500 tape recorder was its variable speed facility. The majority of tapes were recorded at the highest speed (30 ips) so that the signal reproduction fidelity is maximized. Tape play back at slower speeds (15 or 7.5 ips), together with the stop-and-rewind procedure allowed visualization of phenomena not otherwise perceivable.

However, care had to be taken while playing back tapes at slower speed, as some distortion can be introduced. The frequency band width can be reduced at the high frequency end. A frequency response test showed that the response was flat up to at least 10kHz for the three speeds used i.e. 30, 15 and 7.5 ips so that the LiMCA signal was not affected. On the other hand, the global gain of the frequency response was slightly reduced at lower speeds. Consequently, amplitude calibration of the tapes had to be carried out for each speed used so as to compensate for the gain loss.

3.2.2 Oscilloscope

The instrument used for the experiments was a dual trace 12MHz bandwidth Tektronix 5223 Digitizing Oscilloscope with a 5B25N Digitizing Time Base/Amplifier module, a 5A22N Differential Amplifier module and an IEEE-488 bus interface

The sophisticated and sensitive triggering system of the differential amplifier input module was a key element in the success of many transient capture based experiments Also very useful was the "Output Saved Display" control and the IEEE-488 interface respectively for direct plotting of the display and for numeric data transfer to a host computer.

3.3 Description of instrument's interface

3.3.1 Oscilloscope/IBM-PC interface

A standard IEEE 488 interface was used to connect the Tektronix oscilloscope with the IBM-PC equipped with a "Tecmar PC-MATE IEEE-488 Interface" board. Along with the board, Tecmar's IEEE-488 Software Package was also used to control the data transfer. This software package, written in Basic language, provided a complete set of subroutines required to control the IEEE 488 interface bus. However, an application program had to be written on top of the package to implement custom functions.

The scope digitizer used had a resolution of 10 bits both for the time and amplitude coordinates On a screen display data dump request, the oscilloscope sends only the 1016 amplitude values (y axis), while the equally spaced time values (x axis) must be deduced. Since the scope sends no further information such as the signal amplitude or time scales, this information must be independently gathered in order to restore the conditions under which the original transients were first captured The data format used was ASCII The numbers (integers) sent by the Tektronix 5223 oscilloscope were separated by commas (no blanks) and the data transfer was terminated by CR and LF characters

3.3.2 Plotting of data files

A commercial graphic package (ENERGRAPHICS) was first used to create graphics from the ASCII data files The ASCII data files format was transferred to the ENERGRAPHICS format using a Fortran program, written for that purpose Later, the use of Lotus 123 spreadsheet/graph facilities became much more attractive Files were routed to that environment through the use of Lotus IMPORT function, no more format conversion program being required. Eventually, all graphs first created with ENERGRAPHICS were replaced by ones generated with the MATLAB's graphics facilities.

3.4 Experimental procedures

3.4.1 Signal recording sessions

The experimental setup related to this procedure has already been described and illustrated in Figure 3.1. The first step before starting a recording session was to clean the tape recorder heads and tape path of the recorder. This was particularly important in our case, because recording often took place in dusty industrial environments

The next step was to select an acceptable input gain level for the recorder's input module in order to take advantage of its dynamic range. The 0.5V peak-to-peak input level was used in most cases. Even if with this selection, the signal was saturating the recorder's input once in a while, when very large transients occurred, it was the most acceptable selection for giving good reproduction quality of low amplitude signals.

3.4.2 Tape calibration

At the beginning of each tape reel, a calibration signal of known characteristics was recorded. This signal provided an amplitude reference on the tape so that the amplitudes of real recorded transients could be recovered. Since this signal was also affected by any gain losses related to tape readings at slower speeds as well as noises or instability introduced by the presence of dust on the heads and/or tape path of the recorder at recording or at reading time, such problems could be detected.

A 10kHz 0.4V peak-to-peak sine wave was used as the calibration signal. The 0 4V peak-to-peak amplitude took advantage of most of the 0.5V dynamic range. Note that a frequency of 1kHz would have been more appropriate, falling in the 100-10kHz signal's bandwidth. The use of a complex wave form such as a square wave would also have been better at helping in the detection of the effects of the high pass and low pass filters of the signal conditioning system.

After the calibration signal had been recorded during the first few minutes of tape recording, the ESZ signal was fed to an FM input module while spoken information could be recorded through a microphone connected to the AM input module. The spoken information played a very important role since it was the only source of information describing the environment in which the signal has been recorded. Information on probe state, melt conditions, surrounding possible noise sources etc, were tackled in the speech so that these factors could be correlated with the signal at a later date.

The signal could either be recorded continuously or in an interrupted manner In cases where either up or down-mode probe sampling was used, the current is deactivated during half of the cycle so that no ESZ signal was generated It was convenient to stop the recording during these "dead signal " time intervals so as to save tape and avoid pauses of LiMCA signal. When the up/down-mode was used i.e when the current was always active, continuous recording was more appropriate

3.4.3 Tape play back session

Figure 3.2 illustrates the play back instrument setup. A tape play back session starts with the reading of the calibration signal amplitude. Computation of the gain introduced by the recording/reading process was then performed Note that these measurements and calculation had to be done for each reading speed used, since different reading speeds result in different degrees of attenuation in the output signal Typically, the signal is amplified by a factor of approximately five as a result of the recording/reading process

The second step in a session was to reset the tape counter at the end of the calibration signal This was the convention used. All tape footage references were made in relation to this convention

Note that the calibration signal could help in trouble shooting a spoiled or dirty recorder tape path In fact, sometimes, the calibration signal showed instability even if, at time of recording, the input signal was stable. Instability could be introduced either at recording or at reading time. Cleaning the tape path of the recorder was a good trouble shooting tool and was used any time reading problems were suspected.

3.4.4 Distortion introduced by the instruments

In the process of recording and reproducing the signal, some distortions were introduced. Consequently some transients or modified transients were not part of the original signal and were therefore undesirable. The tape recorder was responsible for most of the noise transients. The principal reason was saturation of the tape recorder's input. This was caused not only by the electronics but also by the magnetic media. Figure 3.3 illustrates the saturation of the tape recorder for a huge normal pulse while using a high quality tape. The peak of the pulse is truncated and "folded" downwards. The use of tapes of lower quality produced even more random wave forms when such tape recorder input saturation occurred.

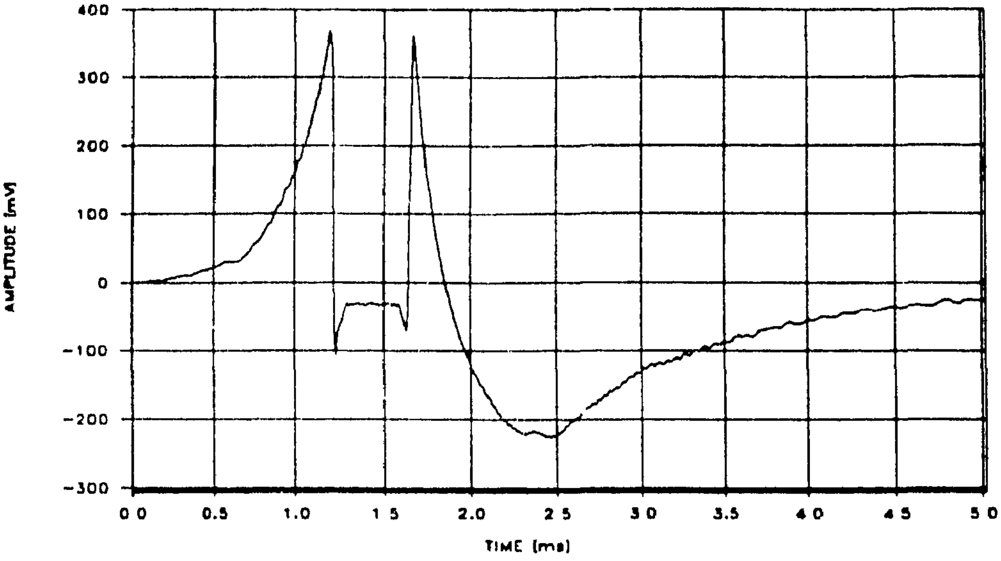

Figure 3.3
Tape recorder input saturation of a large *normal pulse*

The same phenomena have been recreated by recording a sine wave with an amplitude slightly exceeding the tape recorder's input saturation level. The result is shown on Figure 3.4. Both the maximum and minimum portions of the sine wave are distorted by the saturation process.

The presence of dust on the recorder's tape path is also a source of undesired transients. The distortion can either be introduced at recording or at reading time.

The digital oscilloscope would also introduce distortion once its saturation level was reached. Its behaviour was not random however, as in the case of the

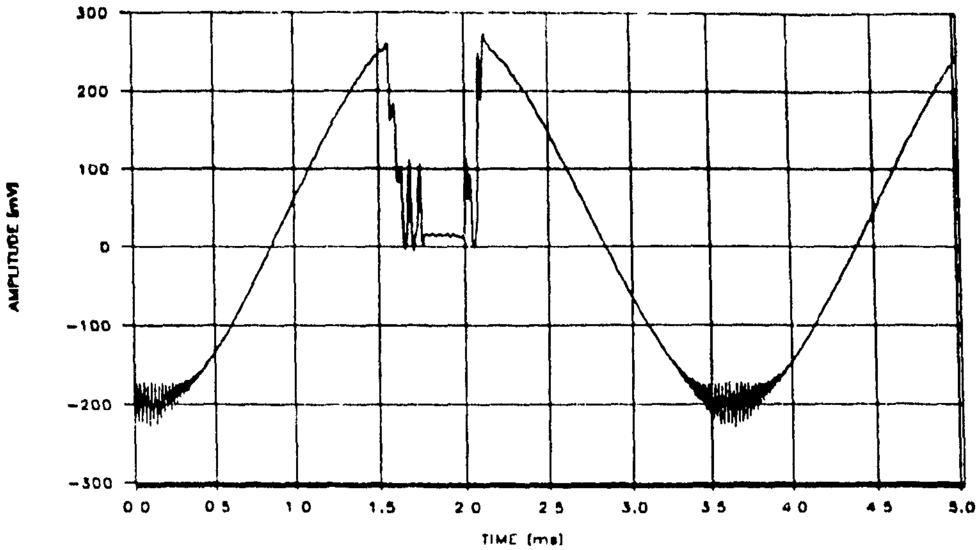

Figure 3.4
Tape recorder input saturation of a test sine wave

tape recorder. The oscilloscope output is kept at its maximum (positive or negative) value for all input levels exceeding the dynamic range of the oscilloscope. Figure 3.5 illustrates a case where three types of saturation occur for a huge normal pulse. In the figure, the first two steps to the left are produced by the tape recorder. The left most is due to positive saturation while the second one is related to negative saturation. The third step, to the right, represents a negative saturation produced by the digital oscilloscope.

3.5 ESZ signal stability period evaluation

For some metallurgical operating conditions, such as melt treatment with a hydrogen degasser located in the launder upstream of the probe, the stability of the ESZ signal was often compromised. The baseline was then no longer a "flat signal", but exhibited oscillating characteristics, whose amplitude masked transients related to the passage of particles through the ESZ. The signal would become relatively stable after each application of the

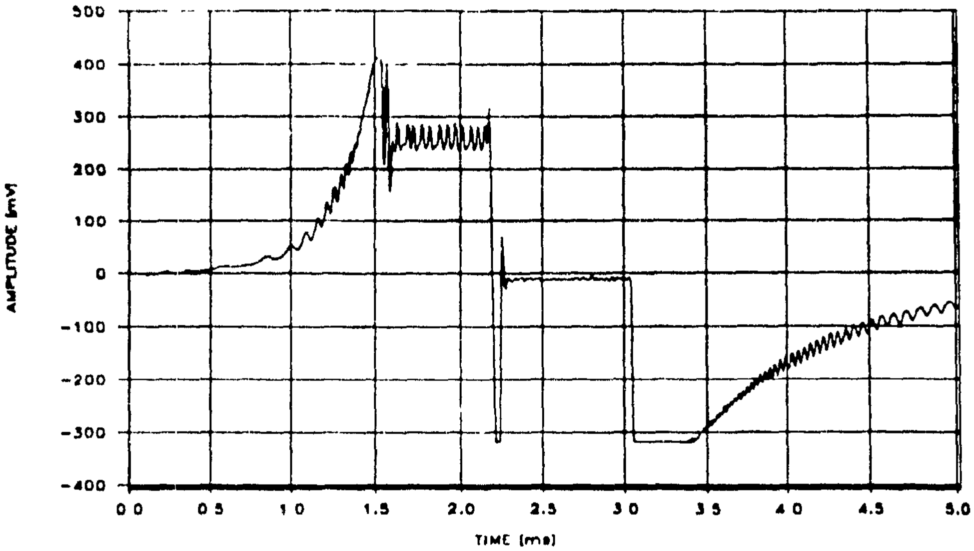

Figure 3.5
Tape and oscilloscope saturation of a huge *normal pulse*

conditioning current, but the baseline oscillation amplitude usually grow to reach a high level before the end of the cycle.

A method has been designed to estimate the stability level of the signal. The first parameter measured was the time interval after a conditioning current, for which the baseline oscillation level stayed below a reference amplitude. A second time interval, the period between the end of the conditioning signal and the moment that the baseline oscillation level reached the tape recorder input amplifier saturation level was also measured. These two time interval parameters are referred to as "Start of instability" and "Start of total instability" respectively.

Signal baseline instability or oscillations are particularly detrimental to the reliability of transient counts. For this reason, the reference amplitude level related to the "Start of instability" was set as low as possible so that it would indicate when the signal begins to be useless in terms of the measurement of particle populations. The amplitude of low level voltage instability was equivalent to those amplitudes related to 20 to 35μm diameter particles. It should be noted that the baseline oscillation level was measured from zero baseline level to the positive peak, not from peak to peak. The purpose of the second parameter, the "Start of total instability", is to determine the time required by the ESZ signal to become completely unstable.

It is considered that these two parameters were sufficient to qualify the voltage amplitude build up of baseline instabilities. The analysis is however, "semi-quantitative" because the measurement of these parameters involved the operator judgment as to when he perceived that the baseline oscillation level had reached the reference levels.

3.5.1 Procedure

The procedures used to collect the data needed for calculating the two time interval parameters are described below :

1/ The ESZ signal's amplitude was calibrated using the on-tape calibration signal.

2/ The oscilloscope's parameters were set so as to aid visualization of the baseline oscillation level. More specifically, the time base needed to be set so that the time window displayed more than five cycles of the baseline's oscillation wave.

3/ For each fill up and or flush part of the cycle being studied :
  A) The tape footage at the end of the first conditioning signal was noted
  B) The baseline level was watched such that,
    i) when it exceeded the reference level for the first time, the tape footage was noted as the "Start of instability",
    ii) when it reached amplifier saturation (if it did before the end of the cycle) the tape footage was noted as the "Start of total instability",
  C) The end of the conditioning footage value was subtracted from the "Start of instability" and the "Start of total instability" footage values to obtain the corresponding footage intervals.

The footage intervals were then converted to time intervals by dividing the footage interval value by the tape speed (30 or 15 ips) as calculated by Equation 3.1.

$$Time\ interval = \frac{Footage\ interval\,[ft]\ X\ 12\,[in/ft]}{Tape\ speed\,[in/s]} \qquad \text{Eq. 3.1}$$

This type of analysis has only been used for melts treated with a hydrogen degasser i.e. for those tape signals which show clear levels of instability. It was evidently inappropriate to apply this type of analysis to signals with a quiet baseline, since the instability trigger levels would never have been reached.

3.6 ESZ signal transient rate of occurrence evaluation

For normal ESZ operating conditions, the method previously described is inapplicable and another technique was developed to estimate the content of the signal. The number of transients occurring per unit of time, i.e. the density of events in the signal was the important parameter to be evaluated. Even more specifically, in this method, the relative rate of occurrence of each class of transient was estimated The classes of transients will be introduced and discussed in Chapter 4.

Because no system is yet available to discriminate between classes of transient, the job has been done through human visual recognition. The rates of occurrence were obtained by counting occurrences of each type of transient over the up-mode, down-mode or both parts of each melt sampling cycle. The number of counts were then divided by the time interval over which counting has been performed, giving an average rate value. A cycle's duration was typically 30 to 60 seconds. Averaged values were thus computed over that time interval. For practical reasons, the melt sampling cycle was selected as the frame of analysis even if important fluctuations in the transient rate of occurrence could occur within a cycle time lap.

Some of the equipment's features were particularly useful in the transient counting process. First, the use of a slower tape reading speed reduced the frequency density of transients on the signal. Secondly, the oscilloscope's triggering system was capable of detecting a transient with an amplitude exceeding the detection level and then freezing it until another transient activated the trigger system. By selecting an appropriate tape speed and triggering level, the operator could first see the transient, judge to what class it belongs, and finally, count it.

The tape recorder's speed could not be reduced by more than a factor of four. The amplitude detection limit was the only other way to control the density of transient occurrences on the scope screen. Setting it high allowed only large transients to be detected, thereby considerably reducing the rate of occurrence of detectable transients On the other hand, this level was kept as low as possible in order to maximize the range of transient amplitudes analyzed. Typically, the detection level was set to transient amplitudes relating to particles of 30μm in diameter.

3.6.1 Procedure

The main steps in the evaluation procedure for the rate of transient occurrences are described below :

1/ Select tape recorder speed according to the average rate of occurrence of transients of the analyzed signal so that reliable count could be performed.

2/ Perform amplitude calibration.
The calibration factor was calculated by dividing the measured amplitude value of the calibration signal by its original amplitude value. The amplitude was measured at the tape recorder speed in use for this specific experiment.

3/ Determine and set trigger level.
This was an important step where the detection limit was selected. The criteria was based on the relation to a specific particle dimension. The previously calculated calibration factor was taken into account. The voltage value corresponding to the chosen detection limit was calculated

and the oscilloscope's trigger system set to be activated whenever that amplitude was reached by the signal.

4 For each cycle .

A) the cycle was assigned an I.D. number.

B) the direction of the melt (up,down or up/down mode) over the time interval considered was determined.

C) the cycle's start and end footage values were measured so the time interval could be calculated.

D) the termination condition for the analysis of the cycle was determined and was assigned an appropriate name tag according to the following list:

"A" --> Melt flow inversion
"B" --> End of recording
"C" --> Occurrence of another conditioning current
"D" --> Impossibility to count transients due to high rate of occurrence
"E" --> Occurrence of a long non attenuated oscillation

E) For each type of transient

a) the cycle was scanned and occurrences of related transients were counted.

b) the rate of occurrence was calculated by dividing the count value by the time interval

The raw data obtained from this type of experiment were transferred to LOTUS 123 worksheets for easy processing and plotting of the data.

CHAPTER 4 -- CLASSES OF REAL SIGNALS

4.1 Introduction

The LiMCA signals that were generated and recorded from the real ESZ tubes submerged within real melts did not behave precisely like theoretical signals Differences were observed to varying degrees, depending on the context. While one aim is to minimize such differences, one should be aware that observed signals carry information about the sensor and its environment. A number of hypotheses of physical phenomena generating these unexpected signal features are discussed in this chapter.

A detailed investigation of the LiMCA's signal behaviour had not been carried out prior to this investigation. The first step towards a better understanding was to acquire knowledge of its content. The approach adopted was based on the identification and definition of classes of transients. This approach was chosen in anticipation of further work that would involve statistical Pattern Recognition (PR) techniques which in turn will provide the basic concepts for transient discrimination processes

From the LiMCA transients, the extraction and analysis of information other then just their amplitude have important benefits In the first place, the ability to identify and understand the features of the signal is a major step towards automatic validation of particle size distribution data This ability may also develop applications related to the control of the sensor. These two improvements, if they can be performed in real time by a machine, would significantly reduce the operating cost of the LiMCA apparatus. Indeed, training and supplying the specialized personnel required to operate the LiMCA represents an important fraction of the operating cost.

These developments will also benefit to the application of the LiMCA techniques to metals other than aluminium. Indeed, while the LiMCA technique has been successful in different melts (steel, magnesium and copper) [8,9,10,11], the aluminium signals are definitely the ones closer to the theoretical signal. Based on data to date, it would appear that signals originating from other melts require more complex validation processes since operating problems in relation with the probe materials tend to produce less stable signal baseline.

In the frame of this research, an important parameter measuring the density of transients was introduced Let's define $\bar{n}_m$, the number of transients with amplitudes linked to particles greater than *m* (given in µm) occurring on the signal per unit time, and averaged over specific time intervals. The subscript *m*, in µm, indicates the particle diameter linked to the lower limit of detected amplitude. $\bar{n}_m$ is usually expressed as the number of events per minute [#/min]. Values of $\bar{n}_m$ were acquired independently for each class of transient.

A more significant parameter metallurgically, is N_m, the number of inclusions whose diameter is greater than *m* per unit mass of liquid metal. Measured in K/Kg, N_m ideally represents the number of thousands of particles per Kg of liquid melt N_m is derived from $\bar{n}_m$ and is the main output parameter of the industrial LiMCA instrument and is obtained by assuming that all the transients detected are related to particles (i.e. one class of transient) and that there is a constant rate of fluid flow through the orifice. N_m is therefor calculated according to

$$N_m = \frac{\bar{n}_m}{V_t \times \rho} \times 60s/min \qquad \text{Eq. 4.1}$$

where

V_t is the volumetric flow rate (e.g. 0.5ml/s)

ρ is the density of liquid aluminium (i.e. 2357 Kg/m^3 at 700 °C)

Using these values in Equation 4.1, the numerical relationship between N_m and $\bar{n}_m$ becomes .

$$N_m = 14.14[min/Kg]\,\bar{n}_m \qquad \text{Eq. 4.2}$$

Note that in the aluminium industry, a widely used lower limit for the particle detection diameter range is 20µm. Consequently the value of N_{20} (i.e. N_m with m = 20µm) is typically the reference parameter for aluminium cleanliness.

4.2 Classes of transients

4.2.1 "Normal pulse"

This first class of transients corresponds to phenomena related to normal or desired ESZ behaviour. These transients are easily interpreted as the passage of an nonconductive particle through the ESZ orifice.

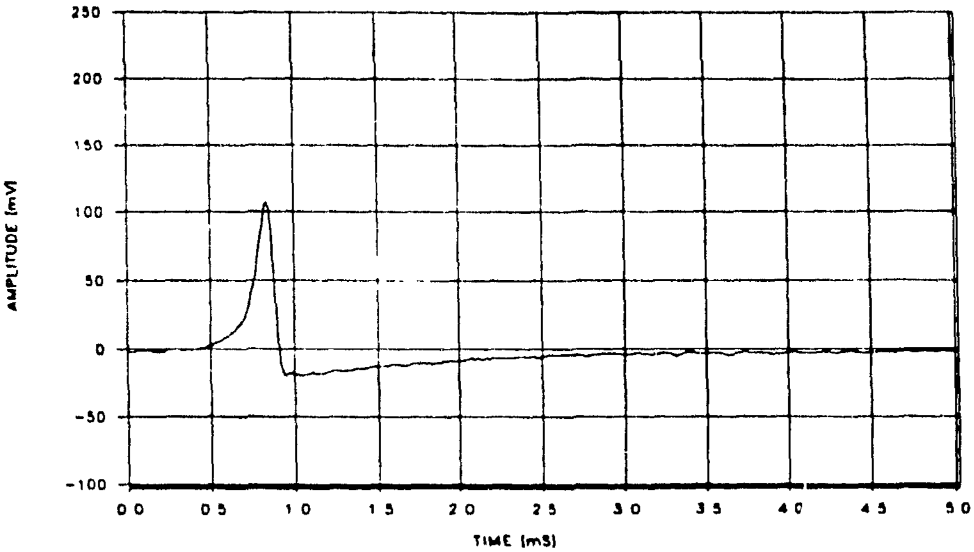

Figure 4.1 Typical *normal pulse*

DESCRIPTION

In the time domain, these pulses have an asymmetrical bell shape The asymmetry is introduced by the High Pass Filter as seen in Section 2.3.2 of Chapter 2. Figures 4.1 and 4.2 show two typical members of the *normal pulse* family. Although their amplitudes may differ, all *normal pulses* are characterized by the following features.:

1/ an under-shoot effect at the foot of the falling edge

2/ an exponential baseline recovery governed by the high pass filter time constant (RC = 1.0ms)

3/ a slightly increased falling edge slope compared to the rising slope

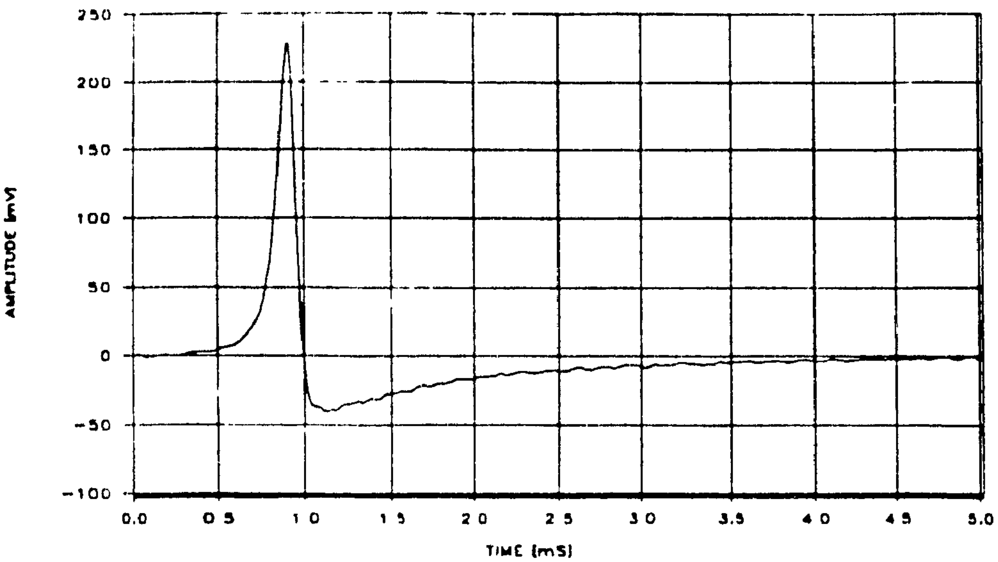

Figure 4.2 Typical *normal pulse*

The pulse voltage amplitude, as provided in Table 2.2 for particle diameters of 10 to 100 µm, ranged from 2.4mV to 2.4V following preamplification of the raw transient by a gain of 1000.

The half height pulse width is typically in the order of 0.2ms. However, it may range between 0.1 to 0.5 ms under standard operating conditions (differential vacuum/pressure of 2.5psi, 300µm diameter orifice).

A summary of the relative rates of occurrence of *normal pulses* is given in Table 4.1. The relative rate of occurrence data is provided for eight data sets. In a given data set, the rate of occurrence of each class of transient was measured for each melt sampling cycle, for a number of consecutive cycles. Data sets #1 to #4 and data set #8 were collected from in-plant experiments, while data sets #5 to #7 were obtained in a laboratory environment. For each melt sampling cycle studied, an $\tilde{n}_{30}$ (#/min) value was acquired independently for each class of transient.

In Table 4.1, four new parameters are introduced. First, *X of* $\tilde{n}_{30}$, corresponds to $\tilde{n}_{30}$ values averaged over the number, *N*, of melt sampling cycles studied in the particular data set, for the *normal pulse* transient class. *X of* $\tilde{n}_{30}$ is calculated using Eq. 4.3, where the i indices of $\tilde{n}_{30,i}$ refers to the melt sampling number. Secondly, *S of* $\tilde{n}_{30}$, is the sample standard deviation value of the averaging process and is calculated using Eq 4.4. where N and i are defined as above. Thirdly, *% X of Normal pulse ratio* is the relative proportion of each class of transient over all classes. It is defined by Eq 4.5 where the ratio of the $\tilde{n}_{30}$ value of *normal pulses* over the $\tilde{n}_{30}$ value of all classes of transients is evaluated for the i^{th} melt sampling cycle and, by Eq 4.6, where the ratio is averaged over the N melt sampling cycles of the data set. Finally, in the same manner, *S of Normal pulse ratio*, the corresponding sample standard deviation is defined by Equations 4.5 and 4.7.

$$X\ of\ n_{30} = \frac{1}{N}\sum_{i=1}^{N} n_{30,i} \qquad \text{Eq. 4.3}$$

$$S\ of\ n_{30} = \left\{\frac{1}{N-1}\left[\sum_{i=1}^{N}\left(n_{30,i}\right)^2 - \left(\sum_{i=1}^{N} n_{30,i}\right)^2\right]\right\}^{1/2} \qquad \text{Eq. 4.4}$$

$$Y_i = \frac{\left(n_{30,i}\right)_{normal\ pulse}}{\left(n_{30,i}\right)_{all\ types}} \qquad \text{Eq. 4.5}$$

$$\%X\ normal\ pulse\ ratio = \frac{100}{N}\sum_{i=1}^{N} Y_i \qquad \text{Eq. 4.6}$$

$$S\ normal\ pulse\ ratio = \left\{\frac{1}{N-1}\left[\sum_{i=1}^{N}\left(Y_i\right)^2 - \left(\sum_{i=1}^{N} Y_i\right)^2\right]\right\}^{1/2} \qquad \text{Eq. 4.7}$$

The *X of* $\tilde{n}_{30}$ values vary significantly from one data set to another. The values tended to be lower in the laboratory environment than for the in plant experiments. It ranged from 58 to 109.3 [#/min] in the laboratory and from 79.7 to 156.2 [#/min] for the plant. Thus, there was a generally higher particle concentration in the plant melts studied versus the laboratory melts. Also, from one melt sampling cycle to another within the same data set, there are important variations of $\tilde{n}_{30}$. This is shown by the high *S of* n_{30} values in the third column. These variations are large compared to the ones of usual N_{20} values of LiMCA particle counts. These fluctuations may be explained by the fact that 20-30μm particles are not counted in the $\bar{n}_{30}$ parameter. This population may represent up to 87% of the N_{20} counts, since the rate of occurrence of small particles is also more stable than the one of larger particles

Table 4.1

Rate of occurrence of *normal pulses*

data set #	*X of $\bar{n}_{30}$* [#/MIN]	*S of $\bar{n}_{30}$* [#/MIN]	*X normal pulse ratio* %	*S normal pulse ratio* %	context
1,	79.7	33.6	42.0	8.0	Plant
2	192.6	41.0	52.5	1.7	Plant
3	128.3	18.2	87.6	7.5	Plant
4	156.2	102.0	49.4	16.7	Plant
5	109.3	68.6	94.8	6.3	Lab
6	85.5	26.8	85.5	9.7	Lab
7	58.0	13.6	96.7	1.9	Lab
8	65.1	81.4	93.5	8.6	Plant

From the fourth column of Table 4.1, we see that the *normal pulse* class is predominant in the laboratory experiments (85% to 95%) while its presence goes down to 42% of the transient population for the worst in-plant experiment case. However, the sample standard deviation of the *%X normal pulse ratio* is very low compared to the *X of $\bar{n}_{30}$* ones. This means that even if the number of pulses vary considerably from one melt sampling cycle to another, the proportion of this class of transient compared to all others is relatively steady, along the consecutive ESZ probe cycles.

PHYSICAL PHENOMENA

Normal pulses are related to the passage of nonconductive particles through the ESZ orifice. As seen in Section 1.3, the amplitude of the pulse is related to the fractional volume occupied by the particle within the ESZ. The diameter of a sphere of equivalent volume is derived as the output of the detection process. The bell shape of the transient reflects the smooth entry and exit contours of the orifice

The pulse width is related to the time interval over which the particle remains within the ESZ The mean velocity of the fluid flow through the orifice is the main parameter involved. It is usually stable and constant around its optimal value.

The particle trajectory through the orifice may exert a small influence on the resulting pulse shape. First, because of the fluid flow velocity distribution, particles travelling near the orifice wall move slower than those travelling around the center area. Consequently, in such cases, either the rising, falling or both of the transient's slopes are reduced and the total pulse width is increased. Further, if the orifice shape contains sharp entrance and/or exit corners, the potential field within the ESZ is not homogeneous. Evidently, potential gradients will be much steeper around these corners [12,13]. This has the effect that any particle passing near a sharp corner will produce a resistive pulse larger than if it were to pass further away from this corner However, the Kimax probe orifices that were used within the frame of this work were smooth and very well-contoured, so that such effects are not expected.

INFORMATION POTENTIAL

The above class of signal transients obviously carries important metallurgical information, and the possibility of providing inclusion size distribution of the melt. One should recall, however, that these signals provide no information concerning the nature or chemical compositions of these particles.

The ratio of *normal pulse* transients to signal generated by other phenomena is clearly useful information. A high *normal pulse ratio* ($>$ 90%) is strongly indicative of stable ESZ behaviour. Lower ratios should not be expected in aluminium processing operations studied to date, except for SNIF treated melts. Sudden variations in the *normal pulse ratio*, between consecutive melt sampling cycles or within a cycle, can be strongly indicative of disturbance within the ESZ.

4.2.2 "Positive BaseLine Jump" (PBLJ)

This second class of transients derives its name from the behaviour of the signal when, the potential of the baseline at the electrodes registers a sudden positive step and stays at this new level.

DESCRIPTION

As seen in Chapter 2, a step change in potential at the electrodes will be characterized, after the high pass filtering stage, by a rapidly rising slope followed by an exponential decay back towards the zero volt baseline level. Such an exponential decay will follow the filter's time constant of 1 ms. This is a side effect of the high pass filter which serves as a signature for any *baseline jump* transients. Figures 4.3 and 4.4 show typical *Positive BaseLine Jump* (*PBLJ*) signals.

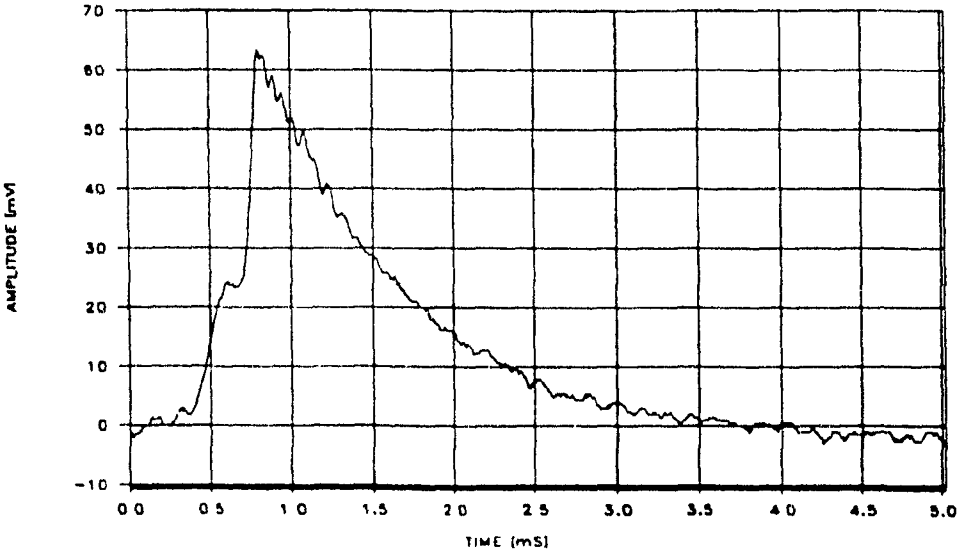

Figure 4.3 Typical *positive baseline jump*

The step or rising edge of the transient is found to be similar to that of the *normal pulses* class and is in the order of 0.1 ms. The rising edge is however much shorter than the falling decay which takes a few milliseconds to return to the baseline level.

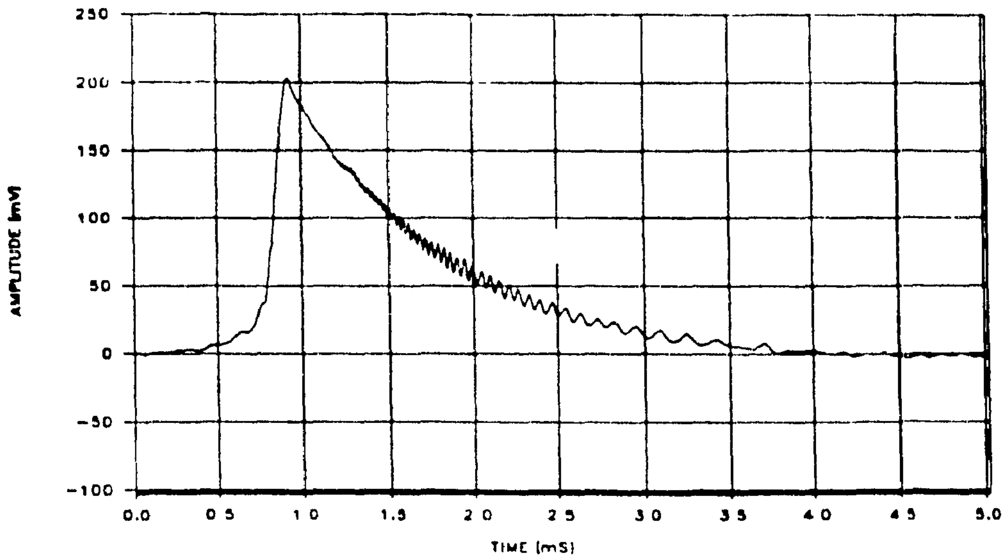

Figure 4.4 Typical *positive baseline jump*

This class of transients is much less frequently observed than the *normal pulse* class. As seen from the fourth column in Table 4.2, this is particularly true of laboratory experiments, where it forms less than 7% of the transient population. However, in more complex experimental contexts such as those using a SNIF degasser (data sets #1,2 and 4), the *positive baseline jump* class may form up to 50 % of all the transient population. The *baseline jumps* are definitely the second most important class of transients to be observed in the LiMCA signal.

PHYSICAL PHENOMENA

A sudden step in the baseline can be attributed to an increase in overall resistivity of the orifice. This increased resistivity is caused by an effective decrease in the ESZ volume, and may be due to the attachment of a nonconductive particle to the ESZ's surface. Thus, a particle may stick to the orifice wall, if it is nonwetted to the melt, and adherence to the surface can lead to a net lowering in the surface energy. One can speculate that a certain degree of roughness or porosity of the ESZ might also cause particles "capture" which would again produce a *positive baseline Jump*.

Table 4.2

Rate of occurrence of *positive baseline jumps*

data set #	*X* of $\bar{n}_{30}$ [#/MIN]	*X* of $\dot{n}_{30}$ [#/MIN]	*X* *PBLJ ratio* %	*S* *PBLJ ratio* %	context
1	95.1	30.2	51.7	51.7	Plant
2	132.7	23.8	36.4	36.4	Plant
3	12.5	9.4	8.6	6.4	Plant
4	156.2	102.0	45.8	17.9	Plant
5	2.3	3.0	3.1	4.6	Lab
6	7.0	5.4	8.3	6.8	Lab
7	0.2	0.4	0.3	0.5	Lab
8	4.1	5.0	5.2	8.1	Plant

The phenomenon may also be related to wetting of the orifice walls by the melt. Thus, a sudden local, or partial decohesion of the melt from the wall of the orifice's sensing zone could also cause periodic *positive baseline jump* transients. The passage of "long particles" or "stretched bubbles" would also be expected to generate *PBLJ* transients. However, no evidence for such phenomena have been observed in aluminium melts, not in the micrographs of solidified melts, where inclusion types , composition and shape can be measured.

INFORMATION POTENTIAL

It is not obvious whether such transients should be interpreted as inclusions (and therefor counted) or disregarded. Like *normal pulses*, the amplitude of a *BLJ* can be related to a particle diameter using the same mathematical relation, i.e. Equation 1.8. Consequently it would be logical to interpret a *BLJ* signal as indicative of a particle entering, but becoming attached to the walls of the ESZ during its passage from the melt bath into the sampling probe.

However, any *BLJ* is undesirable and indicates a certain degree of bad behaviour of the ESZ It is supposed that the relative rate of occurrence of *BLJ* transients indicates how "sticky" an ESZ surface is to particles. *Baseline jump* transients may herald imperfect wetting or indicate surface porosity. Often, a huge *baseline jump* may be associated with important perturbation within the ESZ such as blocking or unblocking of the orifice, and when the pressure is reversed within the probe as to change the direction of melt flow through the ESZ .

4.2.3 "Negative BaseLine Jumps" (NBLJ)

This third class of signal, as its name indicates, is similar to the one of a *positive baseline jump* excepting, the baseline step is negative. This characteristic is sufficient to make it a distinct class. In practice, no attention was paid to negative transients since the most interesting transients were positive and the triggering system was set to be activated only when a rising edge crosses a positive threshold level above the signal's baseline The negative transients were therefor ignored by the LiMCA electronics even though they probably exist.

DESCRIPTION

The time domain characteristics of a *Negative BaseLine Jump* are identical to that of its positive brother except that the pulse is reversed relative to the voltage axis. Figure 4.5 shows a typical waveform of this class. The transient is initiated by a fast falling edge of typically 0.1 ms while the rising edge recovers exponentially within a few milliseconds up to the zero baseline level, in accordance with the time constant of the high pass filter.

It is interesting to compare the values of X *of* $\bar{n}_{30}$ and S *of* $\bar{n}_{30}$ for both the *positive* and the *negative baseline jumps* transients Table 3 3 gives these numbers for each data set. The X *of* $\bar{n}_{30}$ values of *positive* and *negative baseline jumps* do not balance but do exhibit a certain degree of correlation and are approximately of the same order of magnitude. As their positive brothers, the transients of this class are much less frequently observed than *normal pulses*

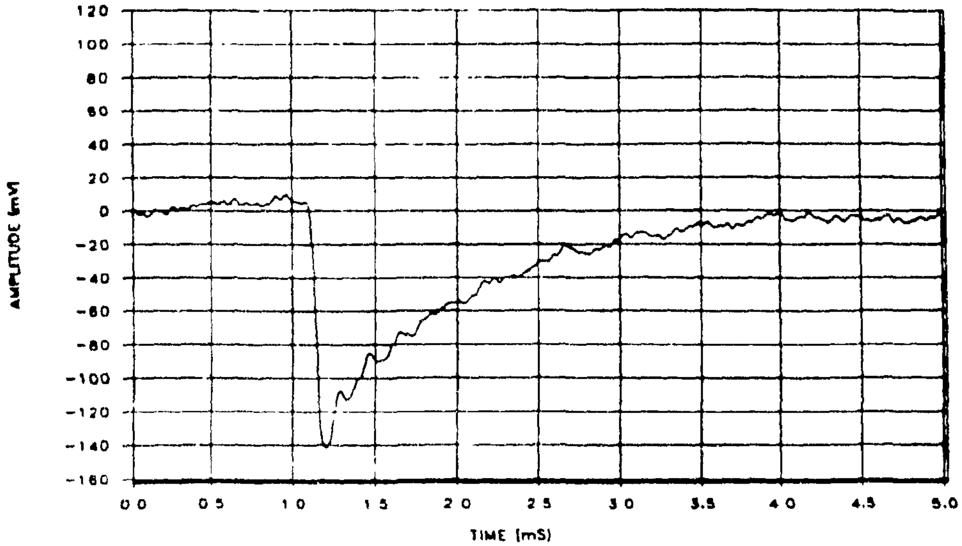

Figure 4.5 Typical *negative baseline jump*

and even less than the *positive baseline jumps*. They were found mostly in te context of an unstable ESZ.

Table 4.3
Occurrence of *positive* versus *negative baseline jumps*

data set #	POSITIVE BLJ		NEGATIVE BLJ		context
	X of $\bar{n}_{30}$ [#/min]	S of $\bar{n}_{30}$ [#/min]	X of $\bar{n}_{30}$ [#/min]	S of $\bar{n}_{30}$ [#/min]	
1	95 1	30 2	25.2	23 8	Plant
2	132 7	23.8	59.0	224 0	Plant
3	12 5	9 4	2.4	2.0	Plant
4	156 2	102 0	27.3	6.7	Plant
5	2 3	3 0	11.7	16.0	Lab
6	7 0	5 4	2 1	1.4	Lab
7	0 2	0 4	0.8	0.8	Lab
8	4 1	5.0	9.6	9.3	Plant

PHYSICAL PHENOMENA

A *negative baseline jump* is the consequence of a reduction of the overall resistivity of the orifice and can be due to a sudden increase in the ESZ volume If so, the amplitude of the transient can be related to the increase in the ESZ volume through Eq 1.8 The ESZ volume increment is presumably caused either by the release of particle(s) previously "captured" by the walls or by erosion of the orifice wall itself. The second hypothesis is not relevant to signals in the present work, since it has been shown experimentally that very little wall erosion occurs during LiMCA operations in aluminium with Kimax probes As for the *PBLJ* the *NBLJ* may also be associated with unstable wetting conditions of the ESZ walls by the melt, i.e. cohesion/decohesion of the metal stream.

INFORMATION POTENTIAL

A high rate rate of occurrence of many large *negative baseline jumps* may indicate. 1) erosion of the ESZ or 2) the release of captured inclusions (i.e orifice cleanup) or 3) imperfect wetting of the ESZ walls by the melt flow. A high rate of occurrence of *NBLJ* should be interpreted as an alarm relative to the condition of the ESZ

4.2.4 "Long pulses"

This class of transients takes its name from the fact that the transients spread themselves over a longer time interval than the *normal pulses*. More specifically, the class regroups those pulses having a long rise time, into a separate set.

DESCRIPTION

A rising edge that is much longer (>2 times) than that of a *normal pulse* of comparable height is the key common feature that distinguishes members of the *long pulse* class. The falling edge does not have distinct characteristics in this class, it can be fast, slow, exponentially decaying, etc.

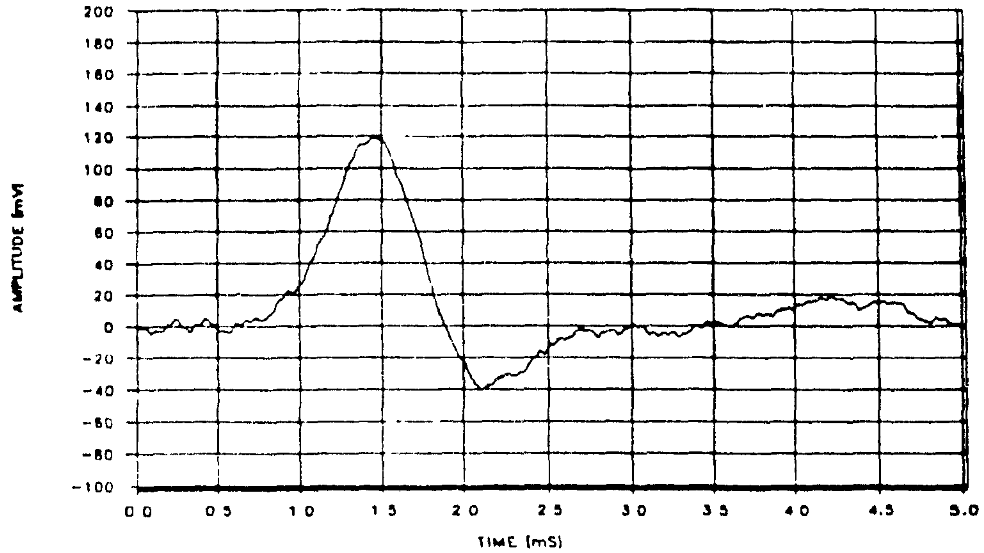

Figure 4.6 Typical *long pulse*

Figure 4.6 illustrates the case of a *normal pulse* stretched along the time axis. In this case, as predicted in Section 2.3, the back shoot effect is amplified because the transient's frequency content is shifted towards low frequency. It can also be noted that the exponential baseline recovery following the back shoot is not pure, since some very low frequency variations are superimposed. Another case is illustrated by Figure 4.7, where a long rising edge is abruptly interrupted by a sharp fast falling edge similar to those of the *normal pulses*. The third case of Figure 4.8, exhibit both very long rising and falling edges, suggesting an abnormally low melt flow rate through the ESZ.

The *X long pulse ratios* for the data sets shown in Table 4.4 are low, i.e. below 6%. The rate of occurrence also fluctuates from one melt sampling cycle to another and even within a cycle. Note that *long pulses* are often of low amplitude because they are partially filtered out by the high pass filter stage. As a result, within the context of this study, the 30μm lower limit for the particle detection range detracts from observations of these transients.

PHYSICAL PHENOMENA

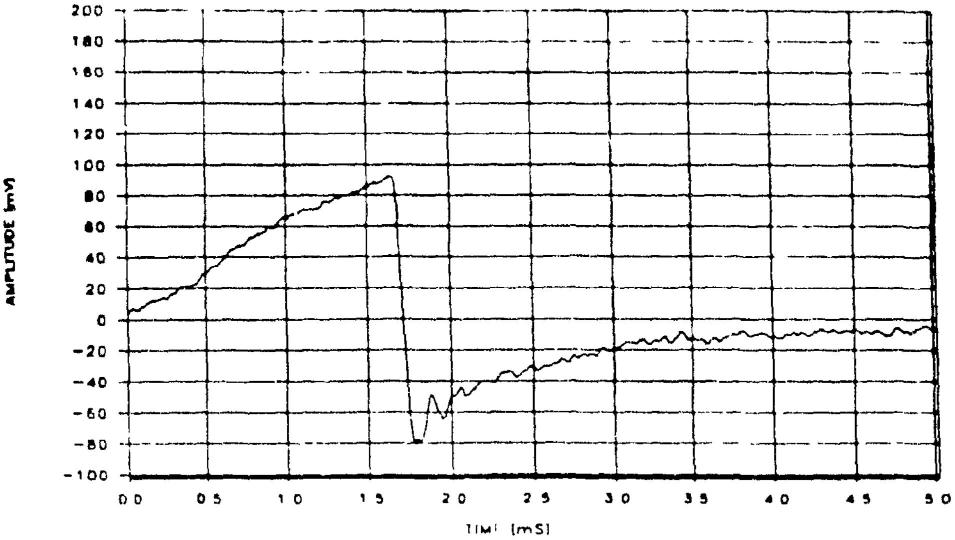

Figure 4.7 Typical *long pulse* with a fast falling edge

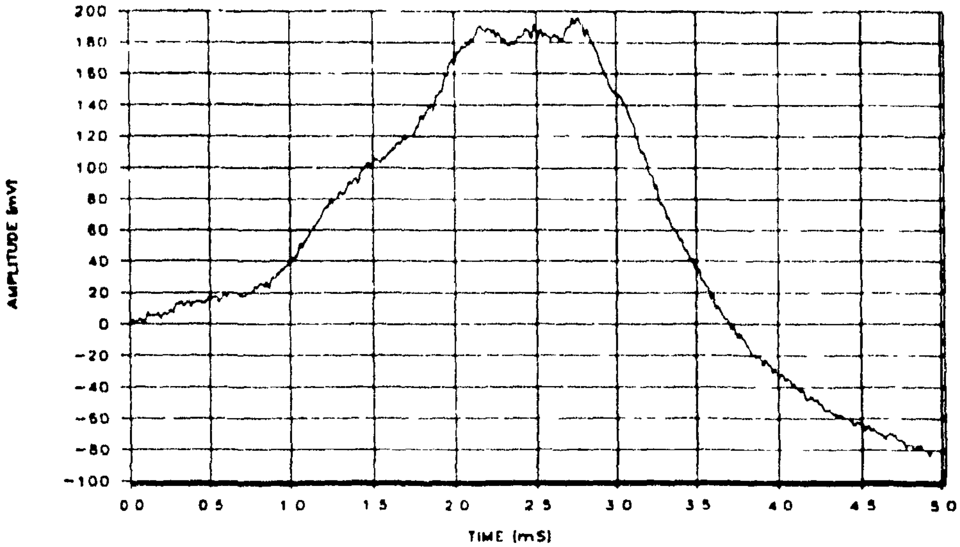

Figure 4.8 Typical *long pulse*

A long rising edge is the consequence of a longer residence time of the particle in the orifice, at least for the first portion of the ESZ. The particle entrainment velocity may be decreased either by friction of the particle with the orifice wall or because the whole melt flow through the orifice has slowed down. A drop in

Table 4.4

Rate of occurrence of *long pulses*

data set #	X of $\bar{n}_{30}$ [#/MIN]	S of $\bar{n}_{30}$ [#/MIN]	X long pulse ratio %	S long pulse ratio %	context
1	4.4	4.4	2.2	2.2	Plant
2	26.6	1.6	7.6	1.7	Plant
3	5.5	2.6	3.8	1.9	Plant
4	9.6	7.5	4.4	4.2	Plant
5	1.7	1.9	2.0	2.0	Lab
6	5.6	3.2	6.2	3.5	Lab
7	1.9	1.1	3.1	1.6	Lab
8	2.8	6.2	1.3	2.9	Plant

melt flow rate through the orifice may be the result of an obstruction or a deficiency in the vacuum system.

In the case of Figure 4.7, a particle trajectory close to the orifice wall while entering and in the main stream for the exit may explain the shape of the transient. Within the entry section of the orifice, the particle is slowed by wall proximity but becomes entrained within the normal melt flow main stream when it is half way through the passage and is therefore ejected at a normal rate.

In the case of Figures 4.6 and 4.8, abnormally reduced ESZ flow rates are the probable explanation. In this connection, one should recall from Section 2.3.4 that the amplitude loss effect of the high pass filter is much more severe on longer pulses. As explained in Section 2.3.4 and illustrated in Figure 2.16, the amplitude of the transient in Figure 4.8 would be only 50% that of the original signal amplitude.

INFORMATION POTENTIAL

While an isolated *long pulse* event does not allow one to conclude anything about the state of the ESZ, many such *long pulses* spaced within a few seconds of each other, together with a reduced density or complete absence of *normal pulses*, is a strong indication of orifice obstruction. This hypothesis can be tested on-line by applying a conditioning current and then checking if the rates of occurrence of transient classes are affected and brought back to normal. *Long pulses* with fast falling edges or isolated *long pulses* are indicative of normal flows through the orifice.

4.2.5 Oscillatory transients

This class of transients derives its name from the oscillatory nature of these signals.

DESCRIPTION

This class of transient does not form an independent group. Its members primarily belong to one of those previously defined. The characteristic feature is the presence of a superimposed oscillation over the typical transient waveform. Most classes of transients have been observed to have superimposed oscillations on occasion. Those oscillations are in the form of a periodic damped or undamped simple waveform.

Figures 4.9 and 4.10 illustrate large *normal pulses*, followed immediately, in their under shoot, by an oscillation. In both cases, the wavelength of the oscillation is of the order of magnitude of the pulse width. While the oscillation in the first one is damped the second one is not. Figure 4.11 displays the case of a *positive baseline jump* on which a damped oscillation is superimposed. In all these three cases the underlying typical transients are evident. In some cases, when the oscillation is not damped, the result is a "pure" oscillation like that shown in Figure 4.12.

The oscillation phenomena was only significantly detected in two contexts as seen from Table 4.5. For data sets #2 and #4, 40% and 50 % of the detected positive transients where found to exhibit oscillatory features. In both cases, a

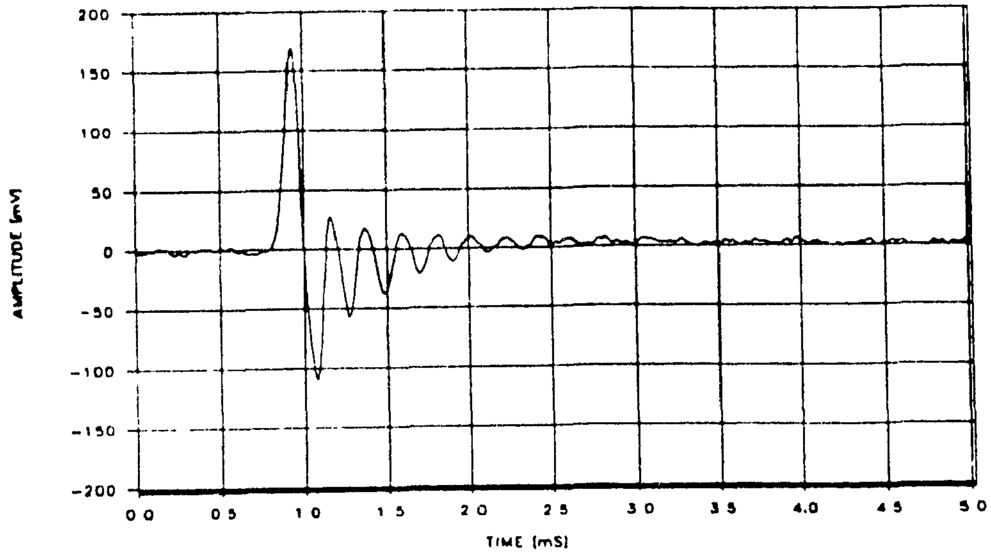

Figure 4.9 *Normal pulse* with damped oscillation

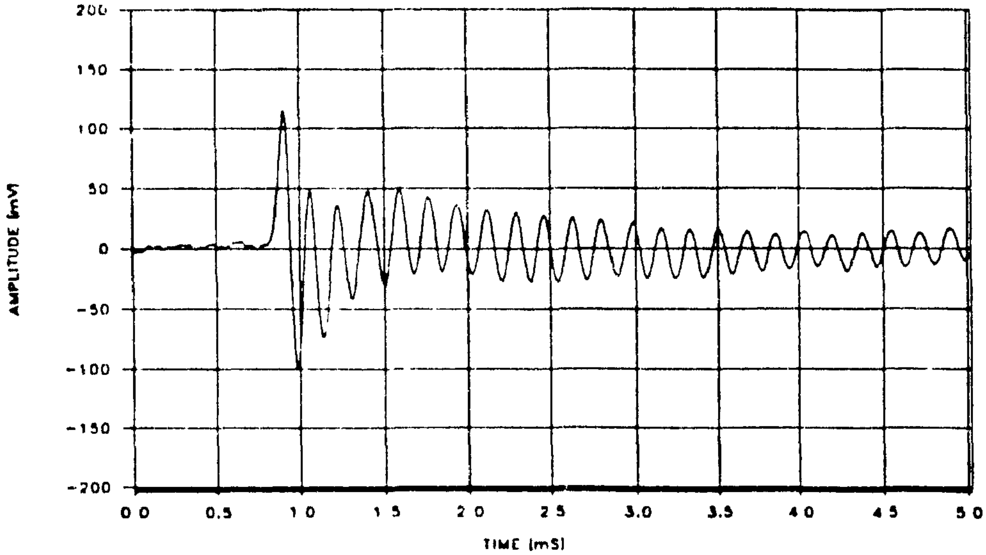

Figure 4.10 *Normal pulse* with undamped oscillation

SNIF degasser was in operation in the melt path upstream from the probe. For other plant circumstances, this phenomenon was almost nonexistent.

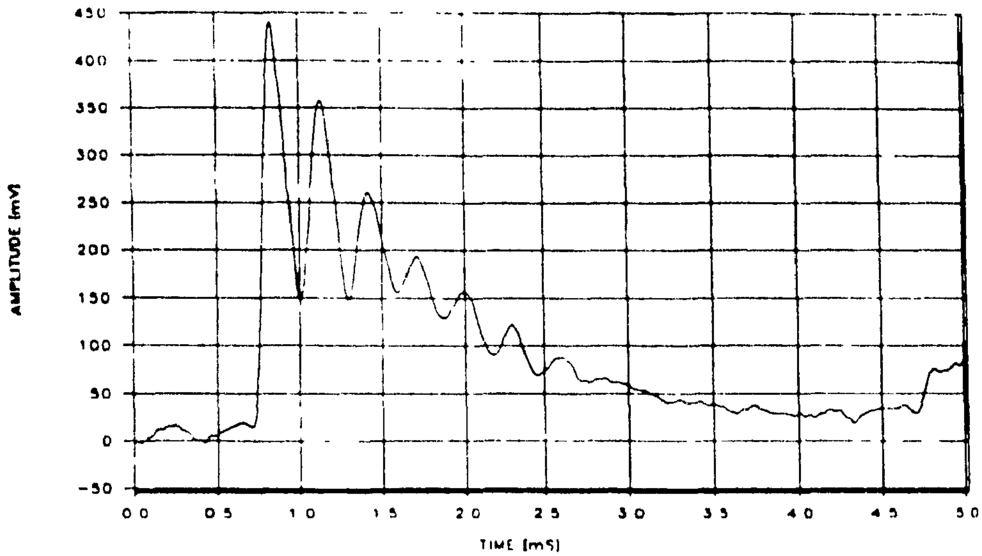

Figure 4.11 *Baseline jump* with damped oscillation

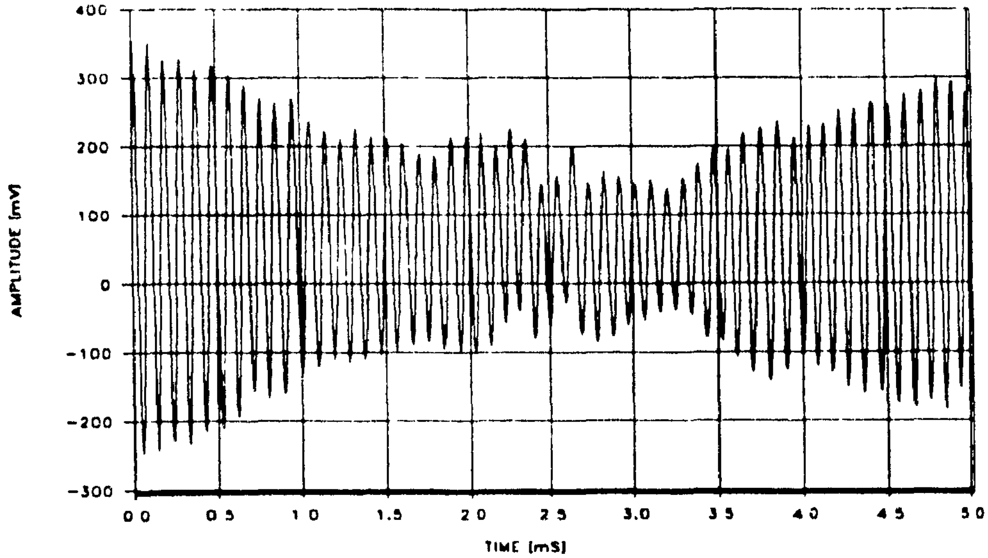

Figure 4.12 Undamped high amplitude free oscillation

The case of data set #6 is special. While 9% of the transients showed oscillatory features, the amplitudes of oscillation that were encountered were much lower than those for data sets #2 and #4. From observations of the

Table 4.5

Rate of occurrence of oscillatory transients

data set #	X of $\bar{n}_{30}$ [#/MIN]	context
1	0 1	Plant
2	40 4	Plant
3	0 0	Plant
4	50 5	Plant
5	NA	Lab
6	9 1	Lab
7	0 0	Lab
8	NA	plant

signal, the phenomena associated with data set #6 were definitely not of the same nature and cannot be compared to the cases of data sets #2 and #4.

Note that in the case of data sets # 1 and #3, where the SNIF unit was also in operation, a "spoon" was used to protect the probe from the direct bulk flow of the melt. Using this means, the oscillation problem was almost completely eliminated. This aspect will be discussed more extensively in Chapter 5.

PHYSICAL PHENOMENA

It is presumed that the oscillatory features superimposed on the ESZ signals were caused by non-wetting of the the melt flow on the ESZ walls. The assumption is that when the wetting characteristics of the ESZ become sufficiently altered as to cause decohesion of the melt from the surface of the ESZ and sets up oscillating waves that contract and expand, inducing variations of its overall resistivity. The consequence is induced oscillations on a typical LiMCA signal

The precise reasons for an alteration of the wetting characteristic within the ESZ are not known The presence of micro bubbles, thin oxide films or a high degree of turbulence within the bulk melt flow around the probe could be possible causes. One thing is clear, the phenomenon occurs as a result of the SNIF process, upstream from the probe, in the launder. In fact, taking the probe further downstream from a SNIF unit considerably reduces these oscillation problems. However in practice, the location of the probe in the launder is often restricted by plant layout to a small area close to a SNIF unit.

INFORMATION POTENTIAL

The presence of oscillating transients is a direct indication of bad wetting of the orifice. Being related to a highly unstable signal baseline, they should be taken as a serious warning. The reliability of a particle size distribution generated with a signal analysis system similar to the one described in Section 2.4.2 would be compromised by the presence of oscillating transients since each oscillation cycle would be counted as a particle related pulse. Frequent oscillations on the signal makes such a system unusable for particle size distribution measurement purposes.

4.3 Discussions

4.3.1 Complexity of the LiMCA signal

Three basic distinct classes of transients of aluminium LiMCA signals have been presented in this chapter. They are the *normal pulses*, the *long pulses* and the *positive and negative baseline jumps*. The hypotheses or explanations presented as for the physical phenomena giving rise to there classes and the information that could be retrieved from these transients partially illustrate the complexity of a given LiMCA signal in liquid aluminium. While the transient classes mentioned above can be characterized, and explained, others cannot. Indeed, from the signal, one could observe an infinite set of randomly occurring transients of unknown source. These can be generated by coincidence of more than one particle in the ESZ, from noise pickup from the environment of the sensor, from switching devices, bad behaviour of an element of the LiMCA equipment, etc ... One can rationalize such events by defining a class of *unknown signals* so as to include all transients that cannot be associated with one of the three classes identified.

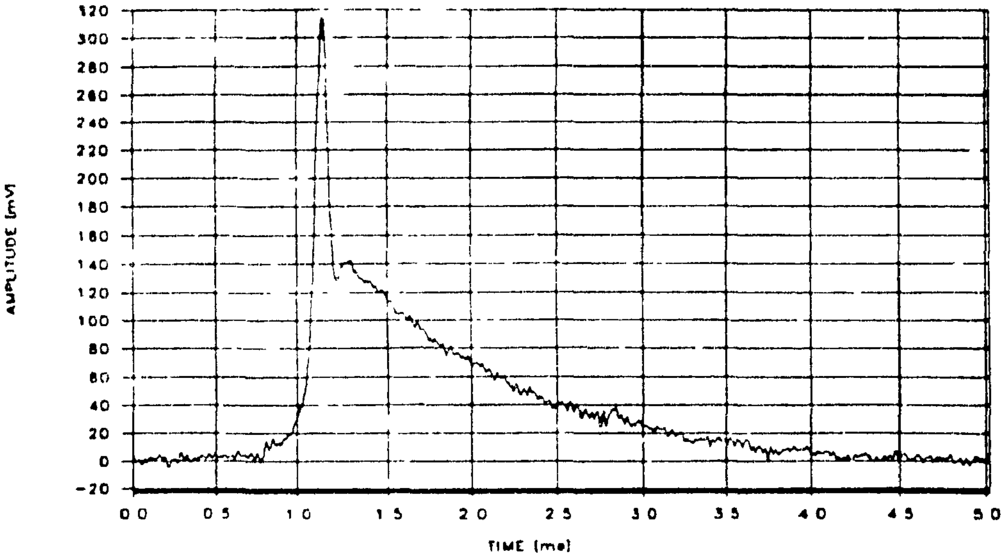

Figure 4.13
Superposition of a *normal pulse* with a *positive baseline jump*

Because of the low concentration of inclusions in the studied melts and the very small volume of the ESZ under the circumstances investigated, the coincidence of event in the ESZ is rather rare. However, the cases of coincidence in the ESZ are interesting. A transient corresponding to a coincidence of events might have unique time domain characteristics. The characteristics of the transients of the individual events may still be distinct but will be superimposed on each other. In the case of Figure 4.13, a *normal pulse* and a *positive baseline jump* occurred almost simultaneously. The passage of a particle was almost complete, producing a *normal pulse*, when probably another particle caused a *positive baseline jump*. Many other examples of multiple *normal pulse* transients or multiple *baseline jumps* transients have also been observed. All these examples illustrate how complex a complete LiMCA signal recognition procedure could become.

4.3.2 Machine recognition of transient types

In any case, an important potential of information is latent in the LiMCA signal without being taken advantage of. From the above discussion, it is clear that the task of properly monitoring and controlling the LiMCA signal is beyond the ability of a human operator. A complex machine could however fulfill this task The schematic of such a machine is shown in Figure 4 14 Some basic signal conditioning stages (High pass filtering, preamplification with gain of 1000, and logarithmic amplification) could be performed by standard high precision analog electronics. The rest of the monitoring and control of the LiMCA signal could be performed by a machine with three level of complexity

At a first level, a detected transient would be digitized and its characteristic features (amplitude, duration, frequency content,) extracted using Digital Signal Processing (DSP) techniques This could be implemented using a dedicated DSP microprocessor board or custom hardware installed in a IBM PC so that real time processing may be achieved. At the second level, the extracted features of the transient would be used to categorize it in one of the LiMCA signal class Statistical Pattern Recognition (PR) techniques could be used to perform such a task Another dedicated microprocessor board would be required here since this task is computationally hungry. Finally, at a third level, both the features and class data of each detected transient, together with other information provided by external sensors and by the operator, are used to generate a validated particle size distribution as well as for control of the LiMCA probe. This stage of processing could be implemented by the processor of the host IBM-PC running software built on ruled based Artificial Intelligence (AI) techniques.

While the system described above is a design proposition, some work has been done to evaluate the suggested statistical pattern recognition approach [14] In the frame of that investigation, the classification task was limited to a two class problem, i e. discrimination between the *normal pulses* and *baseline jumps*. For each class, a sample set of typical transients was used The time domain transients were converted to the frequency domain and/or autocorrelation domain and were approximated by polynomial curve fitting as a mean of dimensionality reduction of the resulting vectors Using the

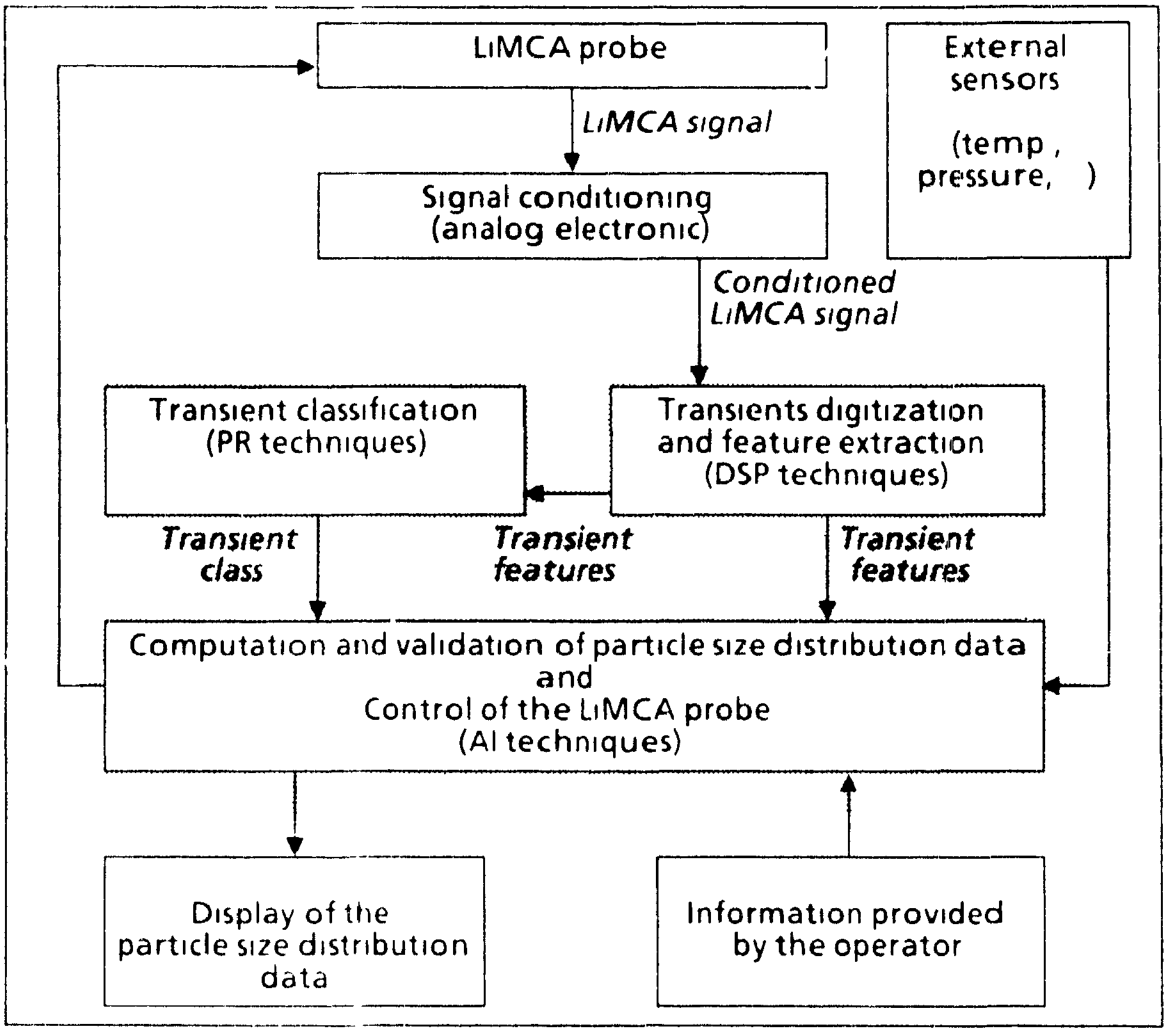

Figure 4 14
Schematic for the control and monitoring of signal generated by a LiMCA probe

coefficients of the polynomial fitting, a simple linear categorizer method was used to assign a class to each transient of the data sets. Very encouraging recognition rates were obtained (up to 90%) for the test data sets. Although these results were obtained with limited data sets (40 transients per class), off-line computations and only for a two-class problem, they proved that the pattern recognition approach can be used for LiMCA transient classification.

CHAPTER 5 -- SIGNAL BEHAVIOUR IN SPECIFIC SITUATIONS

In this chapter, the eight data sets collected from the signal recorded on tapes are analyzed in more detail. The relative rate of occurrence of the different transient classes will be used to characterize the signal behaviour within the context of each of the data sets.

5.1 Normal conditions of operation

The operation of the LiMCA system in a laboratory furnace is usually not as problematic as compared to in-plant operation, since noise level (acoustic, electromagnetic) and the presence of dust, which are the main causes of troubles in the plant environment, can be eliminated. The melt flow around the probe is also far more quiescent in a small, closed, laboratory furnace than in a plant launder For all these reasons, the signal obtained in the laboratory experiment represents the optimal signal

From the previous chapter, we can conclude that in an optimal signal, the proportion of *normal pulses* dominates over the sum of all other classes. Such a case is illustrated in Figure 5.1 from data set #7. The $\bar{n}_{30}$ values of the *normal*, the *base line jump* and the *long pulse* classes are plotted for 10 consecutive cycles. The plotted $\bar{n}_{30}$ values correspond to the number of observed events per unit time. For a given class of transient, they are obtained by counting pulses (related to particles with diameter $>30\mu m$) during a melt sampling cycle and dividing that number by the time interval over which the counting procedure took place.

It is clear from Figure 5.1, that the rate of occurrence of the *normal pulse* class is much larger than that for other classes. While there are a few occurrences of *long pulses*, *baseline jumps* are almost nonexistent. The count rates are also relatively steady from one melt sampling cycle to another. Together, these considerations characterize a stable signal. With such a signal, reliable particle size distributions can be easily extracted without the need for a transient type discrimination procedure.

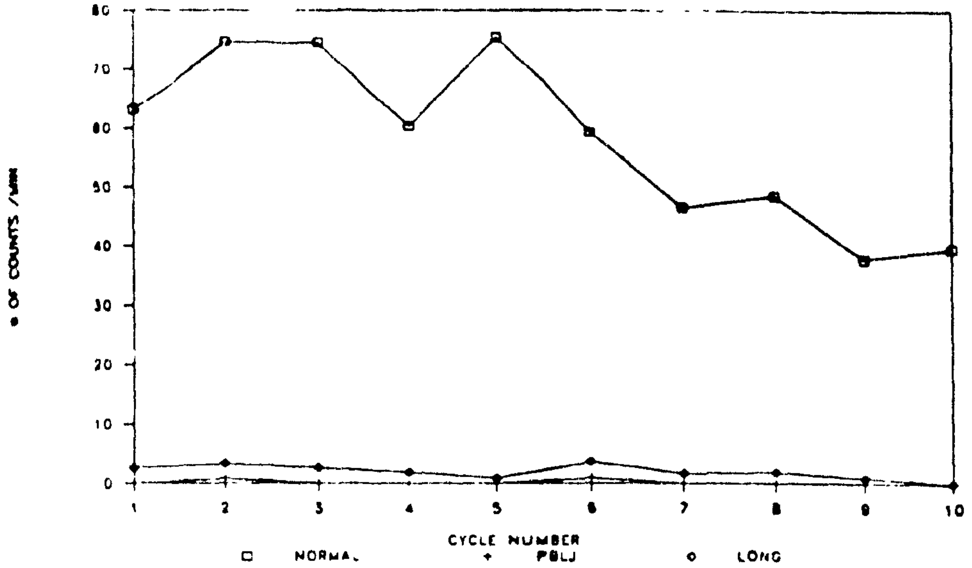

Figure 5.1 $\hat{n}_{30}$ occurrence rate
Up-mode analysis from laboratory experiment

The count rate of the *normal pulse* class tends to decrease with increasing cycle number. Metallurgically, this can be interpreted to be caused by the settling out of large (>30µm) particles from the sampled melt.

Note that the occurrence curves are obtained from counts of transients with amplitudes related to particles of 30µm and greater. No data are available for the transient occurrence rate related to the 20-30µm particle range. However, qualitative observation of the signals suggest that there is a significant correlation between the relative count rates observed over, and below, 30µm.

5.2 Orifice obstruction

The obstruction of the orifice is a relatively frequent problem while operating the ESZ probe in liquid aluminium. Physically, the melt flow is reduced or even interrupted while the electric current still passes through. The resulting signal shows little sign of activity where only *long pulses* and a slowly moving baseline are observed. Because of its quietness, such situations often do not draw the attention of the operator.

If a constant melt flow rate through the ESZ is assumed, an orifice obstruction is deleterious to the reliability of measured particle concentration, as they cause under estimation of the true density of particles in the melt since the orifice melt flow is reduced.

The conditioning current is a powerful on-line method to test the hypothesis of orifice obstruction. When abnormally low count rates or suspiciously quiet signals are observed, a conditioning current is applied by the operator. The high density of energy created in the orifice from the application of the conditioning current clears the orifice of any dirt blocking the passage of melt through it. In a case of orifice obstruction, if the normal rates of occurrence of the transients are recovered immediately after the application of one or two conditioning currents, the diagnostics will have been confirmed. Measuring the orifice voltage drop is also an effective mean of detecting blockage.

The $\bar{n}_{30}$ occurrence curves for data set #5 are shown in Figure 5.2 and nicely illustrate cases of orifice obstruction. The figure shows the rate of occurrence of the *normal*, the *long* and the *baseline jump* type of transients over 14 consecutive cycles. The count rates have been obtained from up/down mode analysis for each melt sampling cycle. Cycle #1 corresponds to the very first cycle of the experiment, immediately following the establishment of the first contact of the melt with both electrodes. The experiment was run in a small laboratory furnace.

The occurrence curves show some of the characteristics of normal conditions. The count rate of *normal pulses* is generally much larger than that for the other types of transients. The count rates of both the *long* and the *baseline jump* transient classes are very low, if not null. However, the *normal pulse* occurrence curve shows unusually low level fluctuations both at cycle #2 and cycle #10.

With regard to qualitative observations that can be made with respect to the data in Figure 5.2, it was found that:

1/ After the automatic conditioning of cycle #1, the signal behaved as for normal conditions of operation. This shows that the probe can produce reliable

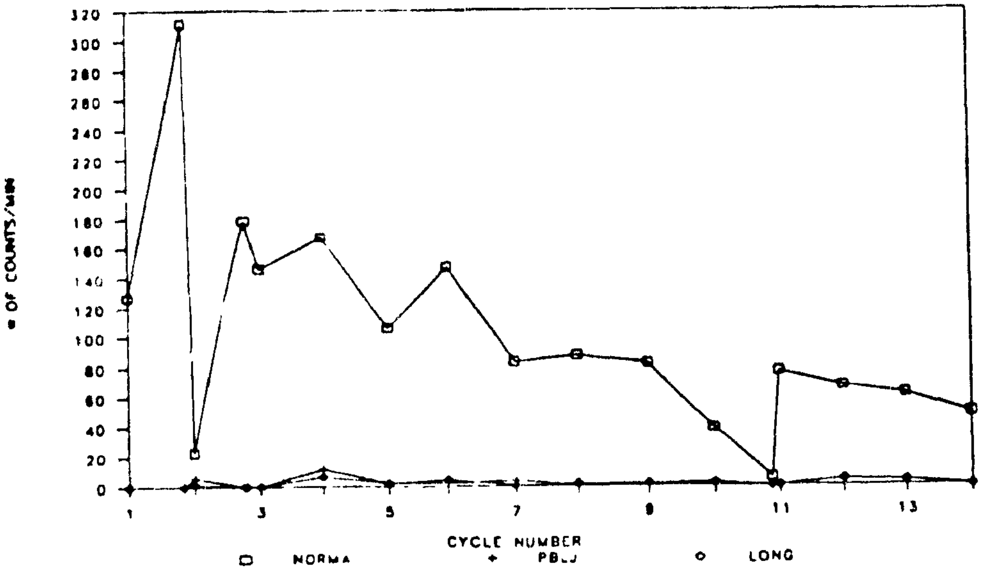

Figure 5.2 $\hat{n}_{30}$ occurrence rate
Up/down-mode analysis from laboratory experiment

signals even at the first melt sampling cycle, immediately following the first melt/electrodes contact.

2/ A manual conditioning current was activated by the operator before the end of the first cycle. The signal remained good. The *normal pulse* occurrence rate however is particularly high.

3/ The automatic orifice conditioning of the beginning of cycle #2 was than activated. Thereafter, the signal behaved as for normal conditions of operation for a few seconds, followed by a huge saturated *baseline jump*, shown in Figure 5.3. Very few *normal pulses* are thereafter observed, while some *long pulses* or baseline instability, are present.

4/ The operator detected this abnormal behaviour and activated the manual conditioning procedure (before the end of the cycle). Instantaneously, the signal's normal characteristics were recovered.

5/ The rest of the experiment behaved as for normal conditions of operation up to cycle #10. At this point, the operator observed a reduced number of *normal pulses* and suspected that something was going wrong. He therefore

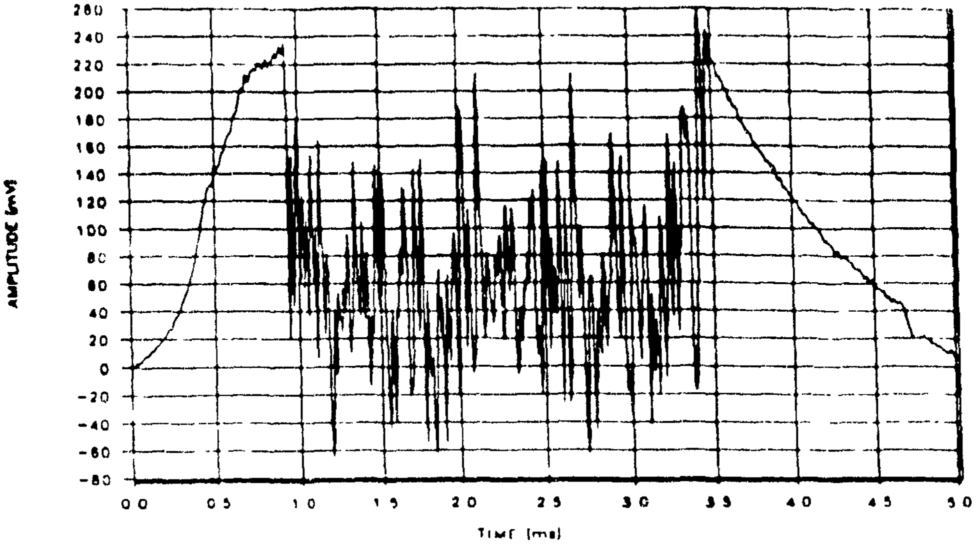

Figure 5.3 Huge saturated baseline jump mark the beginning of an orifice obstruction

activated a manual conditioning current just before the end of the cycle but the situation became even worse such that almost no transients were observed for the last seconds of the cycle.

6/ The occurrence of the automatic conditioning of cycle #11 reestablished adequate signal behaviour.

The sudden decline in the *normal pulse* rate of occurrence was strong indication of an eventual obstruction of the orifice. Other symptoms such as the observation of *long pulses* and slow baseline fluctuations reinforce this hypothesis. The use of the conditioning current as an on-line test should be taken advantage of, as often as these features are detected, and data collected from melt sampling cycles with confirmed orifice obstruction should be disregarded.

By analyzing Figure 5.2, it is not obvious at all that the *long pulses* are indicators of orifice obstruction. However, as is demonstrated in section 2.3.4, a significant amplitude loss is introduced by the low pass filter for the long pulses. Consequently, the $\bar{n}_{30}$ occurrence curve of *long pulses* is always under estimated and most *long pulse*'s amplitude fail under the threshold detection level. This explains why the number of such transient does not appear to be significant in Figure 5.2. Curves of $\tilde{n}_{20}$ would probably show stronger correlations between the *long pulse* occurrences and orifice obstruction with a lower threshold detection level.

5.3 Effects of stirring the melt around the probe

The LiMCA instrument allow for the on-line detection of fast surges of particles thus providing the ability to observe a problem in real time. This is of great help in searching for its origin. The occurrence curves of data set # 8 shown in Figure 5.4 illustrate a detection of fast particle population increase.

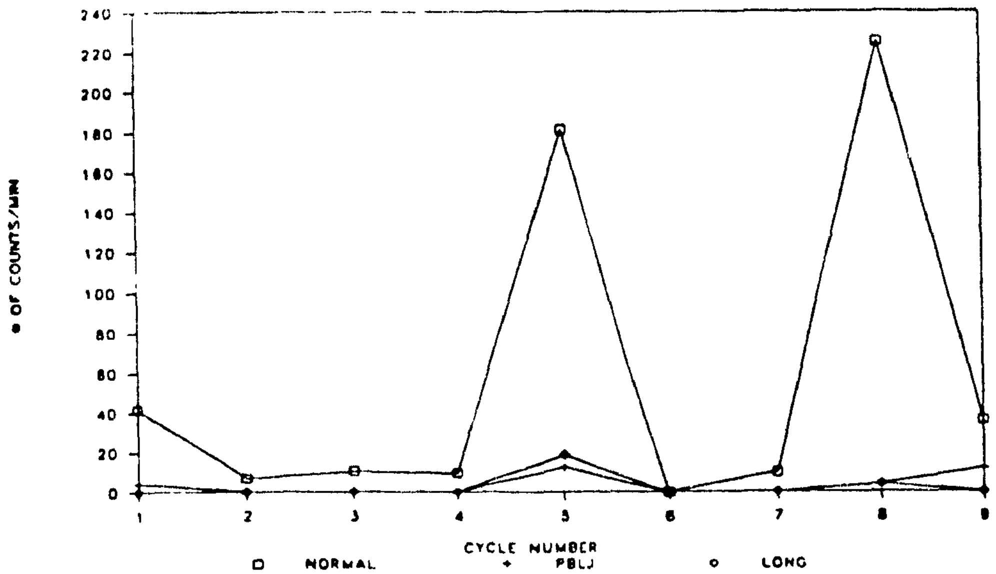

Figure 5.4 $\tilde{n}_{30}$ occurrence rate curves
Up-mode analysis from in-plant experiment

The experiments were performed in-plant and the data presented were derived from the up-mode analysis of the melt by LiMCA over nine consecutive melt sampling cycles. The probe was submerged in the launder, downstream from a SNIF unit, and was protected by a "spoon" with an opened down flow side (see Section 5.4.2 for the description of the "spoon").

As seen, the count rate for the *normal pulse* class started at a low value. It increased abruptly at cycle #6 and decreased back to its original level at cycle #7, before going up again at cycle #8 and finally coming down at cycle #9. These two drastic surges of particles are directly linked to external phenomena. Indeed, both at the time of cycle #6 and cycle #8, an operator had stirred the melt in the spoon around the probe. This action remixes settled particles increasing the local particle population around the probe. However, the density of particles decreases rapidly, within one or two cycles from the disturbance, indicating the particles were probably carried along, away from the probe.

In the case of cycle #6, the number of *long pulses* and *baseline jumps* transients also increased slightly. This indicated a certain degree of induced ESZ flow disturbance.

5.4 In-plant use of a SNIF degasser and its effect on the ESZ signal

The in-plant use of a SNIF degasser in the melt path, upstream of the probe, created the most problematic condition for the operation of the LiMCA instrument in liquid aluminium.

In attempts to operate the LiMCA apparatus in a launder downstream from an operating SNIF unit, the operators were confronted with a major problem of signal instability. Moving the LiMCA probe away from the SNIF unit, the gravity of the problem tended to be reduced. However this solution was often impractical because of space restriction in many of the plants. A large proportion of *long* and *baseline jump* transients, as well as oscillatory features were observed on the transient signals. Typically, the instability is at its minimum level immediately following a conditioning current and this increases constantly, reaching a saturated level of oscillation prior to the end of a melt sampling cycle.

Essentially, in these conditions, the standard ESZ up-mode analysis was virtually incapable of producing a stable signal from which reliable particle size distribution data could be extracted. Special procedures were designed for the operation of the LiMCA under these circumstances and tested in-plant, in order to minimize signal instability. These procedures, and the results from investigations of them are discussed in the following sections.

5.4.1 Down-mode versus up-mode analysis

The down-mode analysis was investigated in order to determine if its usage would improve the signal's stability when operating the probe downstream from a SNIF unit Theoretically, one would expect to obtain comparable particle size distributions for a particular melt sample analyzed both in the up-mode and the down-mode. In practice this was not the case. Typically, the down-mode analysis (not unexpectedly) gave lower count values. This could be explained using the assumption that a certain percentage of the incoming particles are trapped in the probe either when they float out, settle down or stick to the wall inside the probe.

In-probe melt rest periods were also investigated. After the up-mode analysis is completed, i.e. when the probe is full with melt, rather than flushing the tube right away, the melt was allowed to rest for a certain time inside the probe. Again, the objective was to test whether this procedure would improve the signal's stability. Assuming that the presence of oxide films in the melt causes instability of the signal, the idea was that, prior to the down-mode analysis, the rest period could favor the separation of the phase and therefore stabilize the signal. Rest periods of 30, 60, 90 and 120 seconds were tested.

An experimental procedure, as described in Section 3.5, was designed in order to evaluate the baseline stability period. The goal was to evaluate how long the baseline oscillation level takes to reach a specific amplitude. Two such amplitude levels were used in conjunction with the following results. The first one is the transient amplitude linked to 25μm particles. On the first observed occurrence of such an oscillation level, the tape footage is noted as the "Start of Instability". Note that when the baseline oscillation level has reached this amplitude, the transients of all particles of 25μm and smaller cannot be discriminated from the "noise". In a typical particle size distribution, the 20-

25µm range forms 70% of the particle population [3]. This illustrates how deleterious such a level of oscillation is on a signal's utility. The second amplitude level is the one at which the baseline oscillation level saturates the tape recorder input level. On the first observed occurrence of such an oscillation level, the tape footage is noted as the "Start of Total Instability".

For each of the rest periods mentioned above, the down-mode analysis was tested with a number of melt sampling cycles. For each of these cycles, the "start of instability" and the "start of total instability" parameters were measured, for both the up-mode and down-mode analysis. The results are shown in Figure 5.5. The graph shows the values for the "start of instability" (25µm related level) and the "start of total instability" (completely unstable baseline), averaged over a number of cycles, for rest periods of 0, 30, 45, 60, 90 and 120 seconds.

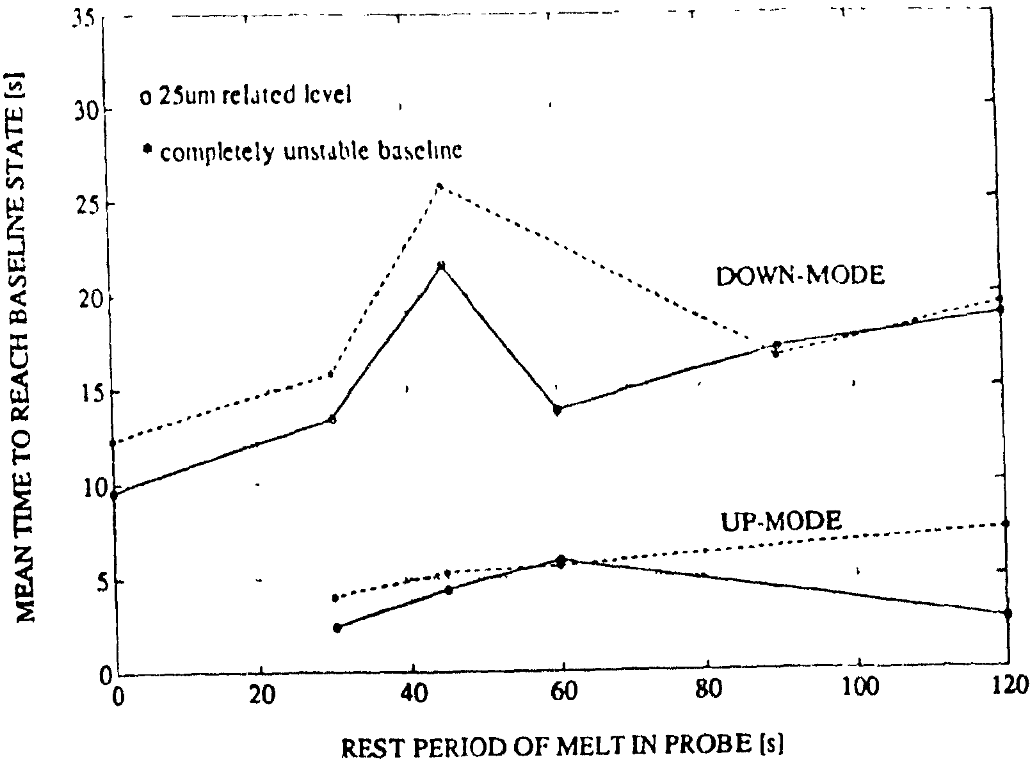

Figure 5.5 ESZ stability intervals
For up/down-mode analysis with rest periods

The curves in Figure 5.5 show that in the up-mode analysis, the baseline oscillation level reaches the 25µm related level within 2 to 5 seconds and that the saturation level is reached in roughly 5 seconds. For down-mode analysis, the baseline's oscillation growth tends to take more time the longer the rest periods. The 25µm related level is reached within 10 to 22 seconds, while the baseline saturated level occurs between 12 and 25 seconds. The saturated baseline state is reached within a few seconds of the 25µm baseline oscillation level, suggesting that the oscillation builds up in a geometrical or exponential manner.

These facts clearly indicate that direct up-mode analyses downstream of a SNIF unit produce useless signals Even in the down-mode analysis, 120 second rest periods do not yield useful signal stability. The 15 to 20 seconds interval of baseline oscillation level under 25um obtained is not sufficient to allow the gathering of useful particle size distribution. Moreover, even if the down-mode analysis reduces the baseline instability somewhat, it does not eliminate the oscillation features found on the transients This is particularly deleterious to the reliability of the particle size distribution since each cycle of an oscillation that crosses the threshold level is registered as a particle.

A better picture of the phenomena resulting from the down-mode analysis of melts processed by a SNIF degasser is obtained by looking at the occurrence curves. The rate of occurrence of the *normal*, the *baseline jump* and the *long* types of transients for data set #4, are plotted for 8 consecutive melt sampling cycles, and given in Figure 5.6.

For this data set, the measurement of the rates of occurrence could not be performed over the whole down-mode section of each melt sampling cycle. Indeed, the counting procedure was interrupted at the point where the instability level became too high for transient types to be detected and identified. Consequently, the occurrence rate values of data set #4 describe only the best ESZ behaviour intervals of the cycles studied.

The large proportion of *baseline jump* transients is the most important feature of Figure 5.6. In fact, the rate of occurrence of the *baseline jump* transients was even higher than the *normal pulses* for the first three cycles and was still high

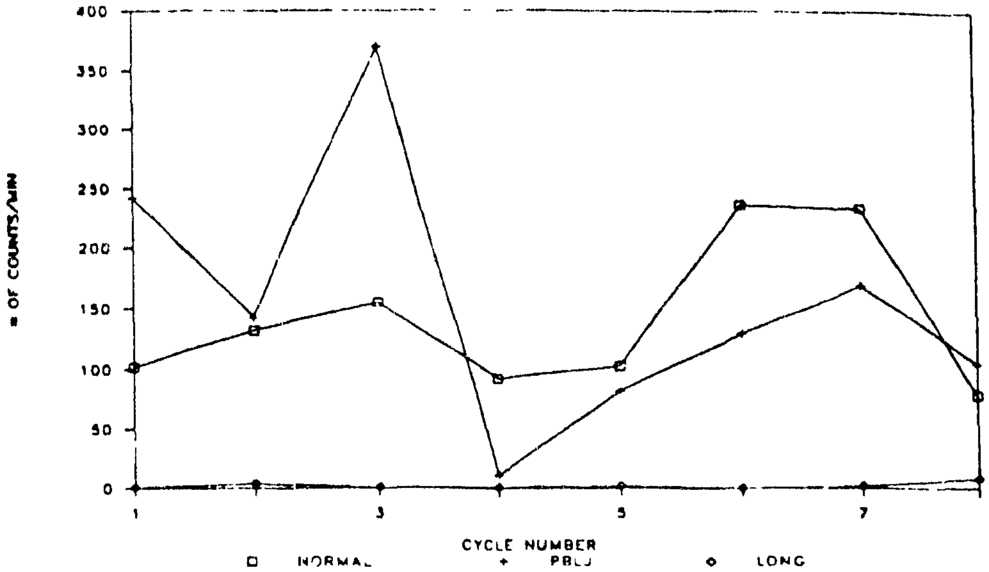

Figure 5.6 $\hat{n}_{30}$ occurrence rate
Down-mode analysis from in-plant experiment

for the others. Cycle #4 was the only one offering worthwhile conditions for the extraction of a particle size distribution. The fluctuations in the rate of occurrence of both the *baseline jump* and the *normal pulse* are also particularly high.

The presence of *long pulses* in this data set is not important and is relatively constant. No sign of orifice obstruction was observed, the only exception being the last cycle (#8), where both an increase in *long pulses* and a significant decrease in *normal pulses* were observed. In this case, partial orifice obstruction is a legitimate diagnosis.

Figure 5.7 shows another view of the same data set where only two occurrence curves are plotted. The first one corresponds to the summed rates of occurrence of all positive transients, i.e. *normal pulses*, *baseline jumps* and *long pulses*. The comparison can be interpreted as the signal's activity on the baseline. The second one corresponds to the number of transients of the first curve that have been observed with oscillatory features. It is consequently a measure of the degree of oscillation of the signal. From Figure 5.7, it can be seen that for most cycles at least 50% of the transients exhibited oscillatory features. This indicates the high degree of oscillation from which the signal suffers.

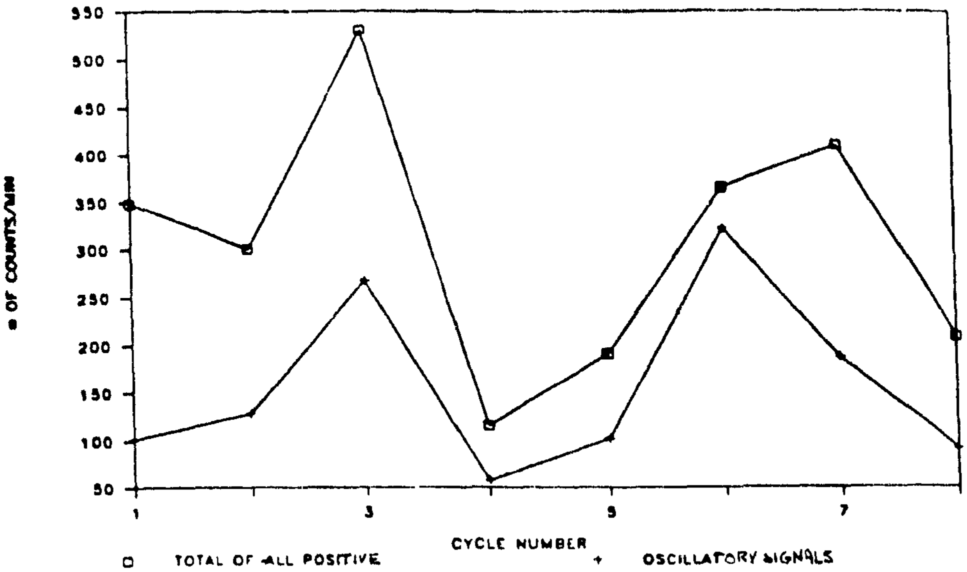

Figure 5.7 $\tilde{n}_{30}$ rate of occurrence.
Sum of positive versus oscillatory transients. Down-mode analysis from in-plant experiment

Naturally, reliable particle size distribution cannot be extracted from this signal, using a straight peak picking mode of interpretation.

5.4.2 Probe protection by a "spoon"

It is believed that the operation of a SNIF degasser introduces gas micro bubbles, oxide films as well as turbulence in the downstream flow of melt in the launder. This turbulent flow can be expected to hinder the disengagement of bubbles and oxide films from the melt. The passage of such micro bubbles or oxide films through the ESZ could cause ESZ instability by altering wetting of the orifice's wall. In the process of seeking a way to protect the probe from these effects by allowing bubbles and films to separate before they reach the ESZ, a "spoon" was used to test the principal.

A schematic of the so called "spoon" is given in Figure 5.8. It comprises a coated metallic open-top box fixed to a handle. The downstream face is equipped with two holes, allowing the melt to penetrate when the "spoon" is partially submerged in the melt. The probe is then plunged in the melt. The

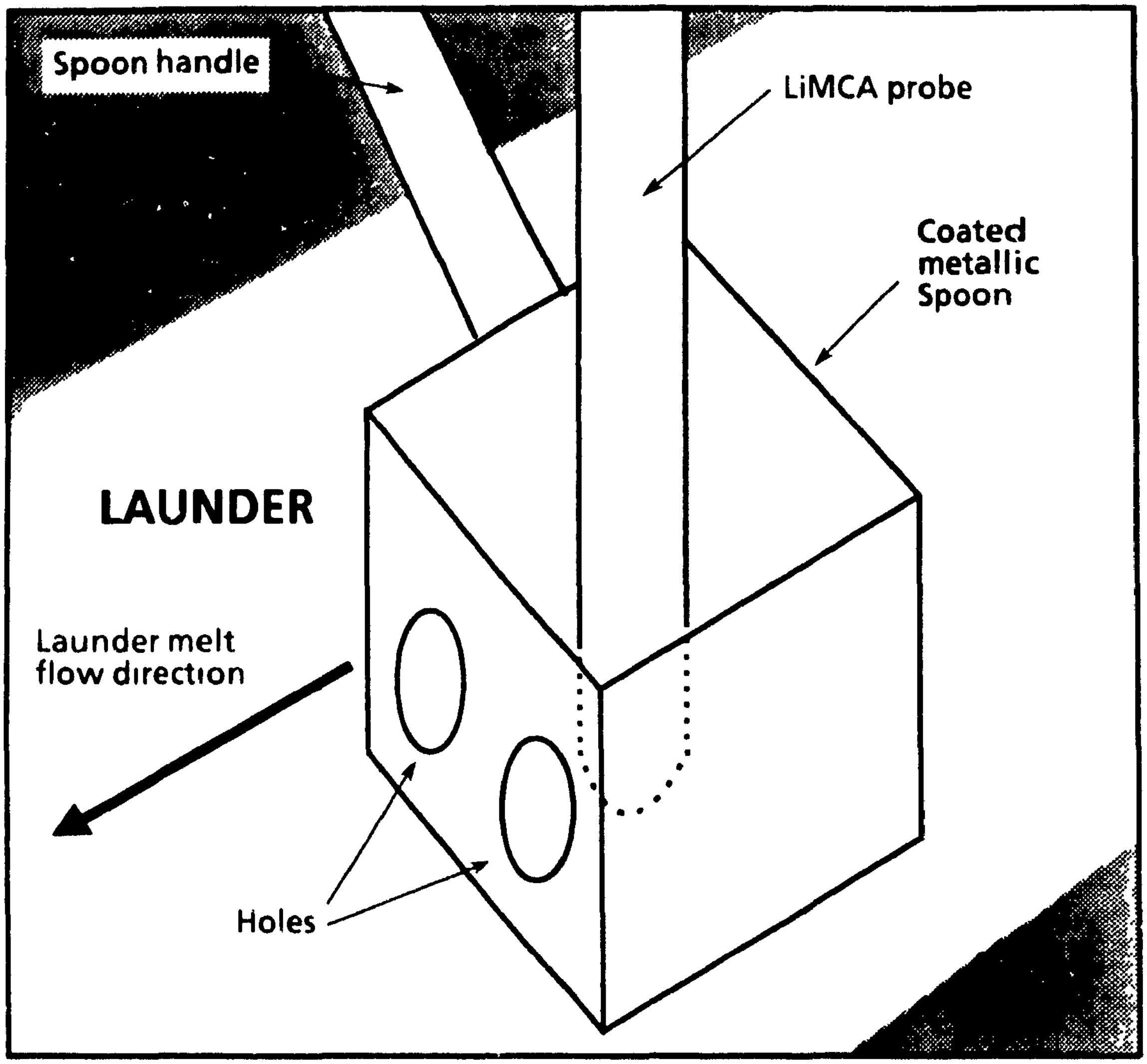

Figure 5.8 "Spoon" configuration

melt in contact with the probe can then only recirculate through the holes on the downstream face of the "spoon".

The use of this device considerably reduced the level of signal instability. Figure 5.9, similar to Figure 5.7, gives the rate of occurrence curves for the sum of all positive transients versus those for oscillatory transients. This data set #1 covers 25 melt sampling cycles over a range of 43 consecutive cycles. The oscillation problem was practically eliminated through use of the "spoon" protection. Indeed, only a few occurrences of oscillatory signals were observed in the first four melt sampling cycles of the experiment. This number is very small and practically negligible in comparison with the rate of occurrence of the grouped positive transients.

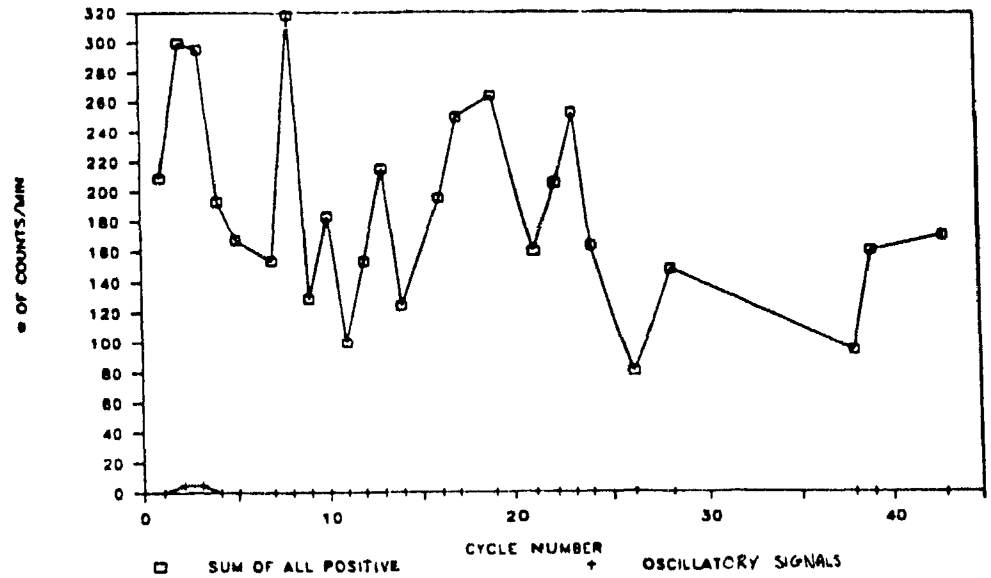

Figure 5.9 $\bar{n}_{30}$ rate of occurrence
Sum of all positive transients versus oscillatory transients.
"Spoon" protection experiment from in-plant experiment

The summed rate of occurrence of all positive transient classes in Figure 5.9 show a relatively high degree of variability. This is often linked to the instability of ESZ. The standard occurrence curves of *normal*, *baseline jump* and *long pulses* are shown in Figure 5.10. The most obvious observation from this graph is the high rate of occurrence of *baseline jumps* which exhibit similar, or higher rates of occurrence than those of *normal pulses*. The high variability between these two occurrence curves also indicates dissimilar behaviour of the ESZ from one melt sampling cycle to the other.

The rate of occurrence of *long pulses* in Figure 5.10 is relatively stable and low compared to the rates for the other classes of transients. No obvious complete or partial orifice obstruction can be identified from these curves.

From these experiments, it is clear that the use of a "spoon" protection does reduce the signal instability level by creating a zone of low turbulence around

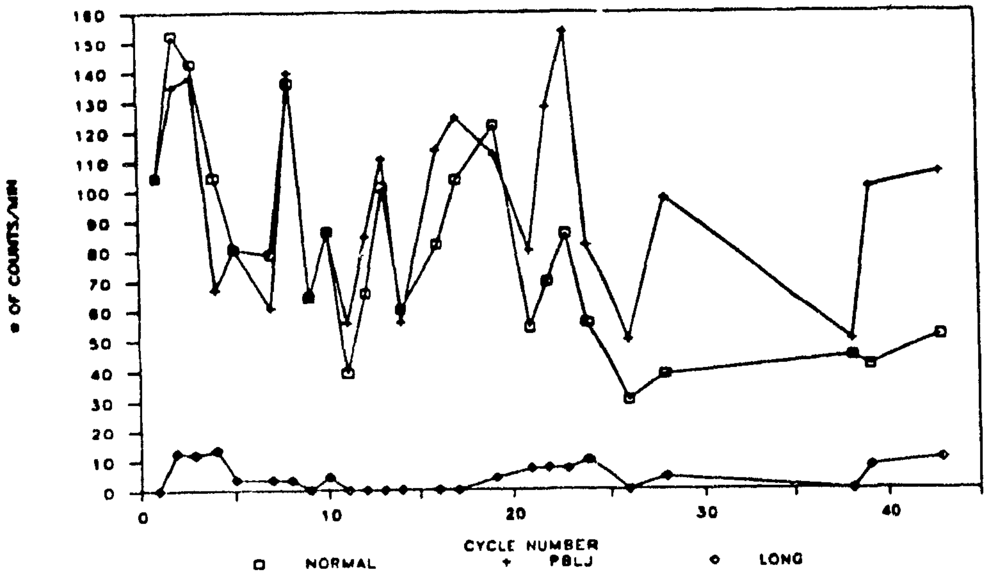

Figure 5.10 $\bar{n}_{30}$ rate of occurrence
"Spoon" protection experiment from in-plant experiment

the probe, allowing micro bubbles and/or oxide films to separate. This, in practice, eliminates the oscillation problem. On the other hand, the rate of occurrence of *baseline jump* is still as important as the one for the *normal pulses*. The use of this device is consequently not a complete solution.

The interpretation of the *positive baseline jump* transients is not straightforward. Presumably, their occurrence is related to penetration of a particle or a bubble into the orifice as well as a local non-wetting of the orifice wall. Figure 5.11 shows the occurrence curves for data set #3. This data set was extracted from the signal of an experiment analyzing the melt upstream of a SNIF degasser unit. The experiment was performed within the same cast as data set # 1. The *normal, baseline jump* and *long pulse* occurrence curves are drawn for five melt sampling cycles over a range of eight consecutive cycles.

This graph shows a clear separation between the rate of occurrence curve for *normal pulses* and the others. It shows near ideal conditions of operation. The rates of *baseline jumps* and *long* transients are stable and relatively low.

Upstream of the SNIF, the rate of occurrence of *normal pulses* ranges from 110 to 150 per minute, while downstream, using a "spoon" (from Figure 5.10), it

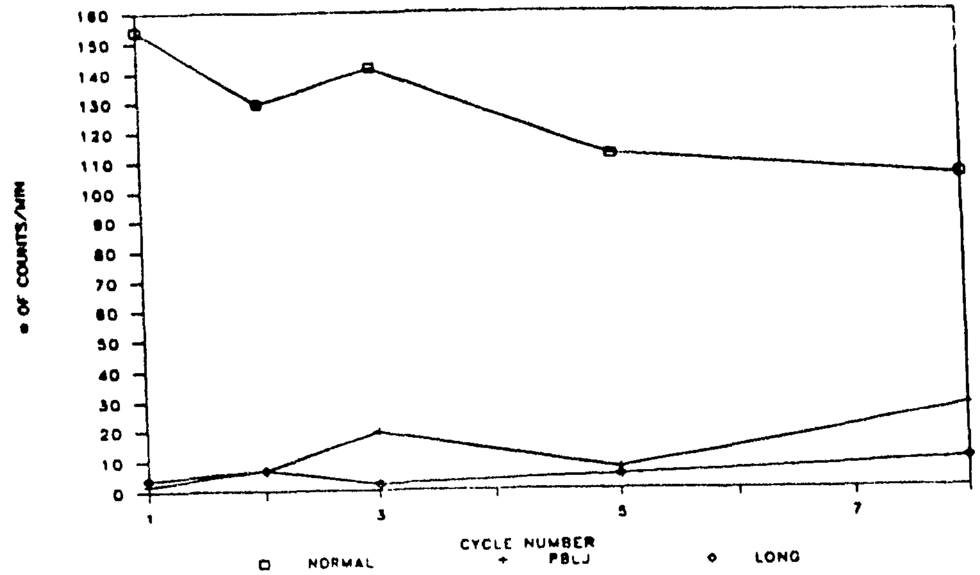

Figure 5.11 $\tilde{n}_{30}$ rate of occurrence
Analysis from in-plant experiment, upstream from a SNIF unit

ranges from 30 to 150 per minute. A comparison of these numbers suggests that the use of a SNIF unit helped to reduce the concentration of inclusions (of diameter >30μm) within melt. This conclusion is correct only provided the *baseline jump* counts are not interpreted as deriving from the passage of particles through the ESZ.

Including the *baseline jump* rates, it is obvious that there is much more activity on the signal downstream from the SNIF than upstream from it. This confirms the fact that the SNIF degasser introduces either flow turbulence, a second micro bubble phase and/or oxide films into the melt and therefore affects the behaviour of the ESZ. The ESZ signal activity is related to the ESZ instability as well as the inclusion content of the melt.

5.5 "Positive" versus "negative baseline jumps"

In Chapter 4, the *negative baseline jump* class of transient was defined and described. Occurrence curves for this class of transient have yet to be discussed. Thus, negative triggering is required to detect them. Positive triggering is always used in LiMCA signal analysis because the principal classes of transients require positive triggering. The significant occurrence of *negative baseline jumps* was only observed when *positive* ones had an important rate of occurrence. Figure 5.12 illustrates three occurrence curves for data set # 1 ("spoon" protection experiment). The first corresponds to the grouped positive transient classes, representing positive activity on the signal. The second and third are respectively the *positive* and *negative baseline jump* rates.

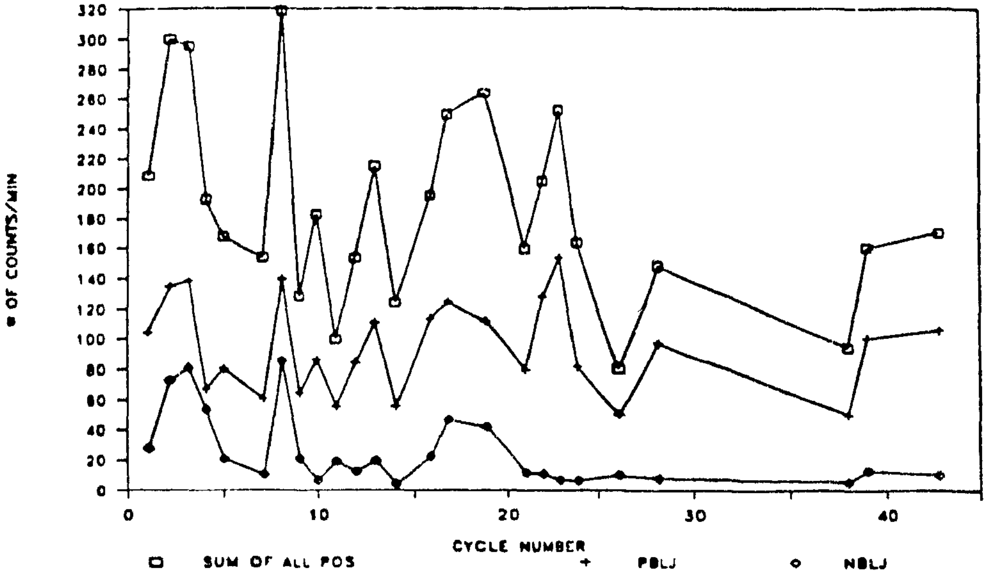

Figure 5.12 $\breve{n}_{30}$ occurrence
Positive versus *negative baseline jumps*
SNIF protection experiment from in-plant experiment

The *negative baseline jump* count rate tends to follow the *positive baseline jump* rates, particularly for the first nine melt sampling cycles of the data set. The rate of occurrence of *negative baseline jumps* were always lower than that for *BLJ*. From cycle # 21 to the end of the data set, the rate of occurrence of *negative baseline jumps* was much lower than those for *positive BLJ's* and the two curves did not correlate.

A much larger rate of *positive baseline jumps* compared to its *negative* relatives, may be an indication of the accumulation of particles on the orifice walls. Strong correlation of these two curves would, on the other hand, indicate a balanced situation in terms of accumulation and release of particles in the orifice. Monitoring *negative baseline jump* rates of occurrence would be particularly useful while operating the LiMCA apparatus in a melt, different than aluminium, in which the probe material is subject to alteration. This way, orifice erosion could be detected.

5.6 Discussions

The sampled data sets studied in this chapter have been derived from only a few minutes of LiMCA signals. One cannot claim that they constitute a complete and sufficient set for representing the LiMCA signal generated in aluminium melts. Drawing a complete picture of the LiMCA signal was beyond the scope of this work. However, the slices of signals and their corresponding data sets were chosen because they reflected a number of identified ESZ states.

The goal of the work presented in this chapter was to show how the ESZ states can be characterized through the relative rates of occurrence of the different types of transients. While examples of such characterizations have been presented, analysis of a much larger set of signals sample should be carried on so that a set of ESZ states and decision rules can be established, based on the relative rates of occurrence of the different transient classes. These rules could be integrated in the third level of the LiMCA signal monitoring and control machine presented in Section 4.3.2 and illustrated in Figure 4.14.

The relative rates of occurrence could be computed over each melt sampling cycle. Making a decision on the ESZ state for each particular cycle allow to validate, correct or disregard, the particle size distribution data generated during that cycle. Monitoring of fluctuations of the relative rates of occurrence over shorter time intervals (every 5 seconds for example) could allow the machine to activate the conditioning current whenever the ESZ state is judged unstable. This way, some melt sampling cycles could be recuperated for the production of reliable particle size distribution data.

The decision rules could be based on fixed relative rates of occurrence threshold values for which an ESZ state is defined (ex.: if more than 50% of the detected transients are *baseline jumps*, the signal is judged useless for the extraction of particle size distribution data). The rules could also be based on comparisons with previously acquired relative rates of occurrence. For example, for normal conditions of operation, the values of relative rates of occurrence should be relatively constant over consecutive melt sampling cycles. Therefore, comparison of such value of previous melt sampling cycle could be indicative of an abnormal ESZ behaviour.

CONCLUSIONS

Metal cleanliness can be measured on-line by the LiMCA apparatus, based on the Electric Sensing Zone (ESZ) technique. The sensor, submerged in a liquid metal bath, produces a characteristic electrical signal transient during the passage of a particle through its sensing zone. Detection of these signals allow to derive the size distribution of the particles suspended in the liquid metal. Signals generated by the LiMCA apparatus, when used in liquid aluminium baths, have been studied.

The transfer function of the high pass filtering stage of the LiMCA apparatus was described using mathematical models and was best characterized by the sine model. As a side effect, the high pass filter modifies the original LiMCA signal transients by reducing their amplitude by a factor of 9%, typically. This amplitude loss is detrimental to the particle size distribution accuracy, leading to underestimation of the particles size. The sine model, through Equation 2.27, can be used to correct the transients amplitude value.

Three basic LiMCA signal transient classes were identified. They are the normal, the long and the positive or negative baseline jump pulses. The normal pulses are related to the passage of a particle through the ESZ and yield to the evaluation of the particle size distribution of the liquid aluminium bath under analysis. The long pulses are generated by the passage of a particle when the melt flow rate through the ESZ is abnormally low. Their amplitude value are reduced more drastically with increasing length. The positive and the negative baseline jumps are respectively related to a sudden reduction or increase of the ESZ volume and correspond to undesirable behaviour of the sensing zone. The detection of transients and the identification of the class to which they belong allow to validate the particle size distributions derived.

When the LiMCA apparatus was operated in a launder downstream from a SNIF liquid metal cleaning unit, oscillatory features were observed on all classes of transients. These oscillatory features were highly detrimental to the reliability of particle size distributions derived from such operations. A few sensor operating techniques such as down-mode LiMCA signal analysis and protection of the LiMCA probe by a "spoon", were tested in order to limit the oscillatory features of the signal. They failed in providing a stable LiMCA signal from which a particle size distribution can be derived.

Rates of occurrence of all class of transient were estimated for a number of ESZ sensor operation conditions. It was shown that the LiMCA signal behaviour and consequently the ESZ state can be characterized using the relative rates of occurrence of the different transient classes.

REFERENCES

[1] Pitcher D.E. and Young R.S.,"Methods of an Apparatus for Testing Molten Metal", U.S. Patent, 3, 444, 726, May 20, 1969.

[2] Mansfield T.L.,"Ultrasonic Technology for Measuring Molten Aluminium Quality", Light Metals, The Metallurgical Society of AIME, pp.969-980, 1982.

[3] Doutre D.A., "The Development and Application of a Rapid Method of Evaluating Molten Metal Cleanliness", Ph.D Thesis, Dept. of Mining and Metallurgical Eng., McGill University, Montréal, 1984.

[4] Coulter W.H., "High Speed Automatic Blood Cell Counter and Cell Size Analyzer", Proc. of the National Electronic Conf., pp.1034, 1956.

[5] DeBlois R.W., Bean C.P. and Wesley R.K.A.,"Electrokinetic Measurements with Submicron Particles and Pores by the Resistive Pulse Technique", Journal of Colloid and Interface Science, Vol. 61, No.2, pp.323-335, Sept 1977.

[6] DeBlois R.W. and Bean C.P., "Counting and Sizing of Submicron Particles by the Resistive Pulse Technique", Rev. Sci. Instr., Vol. 41, No. 7, pp.909-915, 1970.

[7] Smythe W. R., "Flow Around a Sphere in a Circular Tube", The Physics of fluids, Vol. 4, No. 6, pp.756-759, 1961.

[8] Kuyucak S. and Guthrie R.I.L.,"On-Line Inclusion Detection and Measurement in Transformer Steel", Second International Symp. on the Effects and Control of Inclusions and Residuals in Steels", August 17-20, 1986.

[9] Kuyucak S., Nakajima H. and Guthrie R.I.L.,"On-Line Measurements of Inclusions in Liquid Steel", Proc. of the Fifth International Iron & Steel Congress, pp. 193-198, April 6-9, 1986.

[10] Kuyucak S. and Guthrie R.I.L.,"On-Line Detection and Measurement of Inclusions in Molten Alloys of Magnesium", 26th Annual Conf. of Metallurgists, CIM, Winnipeg, August 23-26, 1987.

[11] Kuyucak S. and Guthrie R.I.L.," On the Measurement of Inclusion in Copper-Based Melts", Canadian Metallurgical Quarterly, Vol. 28, No. 1, pp. 41-48, 1989.

[12] Atkinson C.M.L. and Wilson R., "Artefact Peaks in Particle Size Distribution Measured by the Electrical Sensing Zone (Coulter Counter) Method", Powder Technology, Vol. 34, pp.275-284, 1983.

[13] Wilson R., "Calculation of the Electric Field within an Electrical Sensing Zone Counter", Part. Charact., Vol. 1, pp.37-43, 1984.

[14] Thibault J-F., Boisset A., Dallaire F. and Carayannis G., "Pattern Recognition Techniques for Metal Quality Control", Canadian Conf. on Electrical and Computer Engineering, Sept. 17-20, 1989.